PEOPLE'S DEMOCRATIC REPUBLIC OF ALGERIA
MINISTRY OF HIGHER EDUCATION AND SCIENTIFIC RESEARCH
UNIVERSITY OF YAHIA FARES, MEDEA
FACULTY OF TECHNOLOGY
DEPARTMENT OF MECHANICAL ENGINEERING



THESIS Entitled:

# Contribution to the numerical study of multiphase non-Newtonian flows in a porous medium channel

IS SUBMITTED FOR THE PURPOSE OF OBTAINING
PH.D. DEGREE IN MECHANICAL ENGINEERING
Option: Energy
By

**ZID Islam**

Presented on 04/25/2026

IN FRONT OF THE JURY COMPOSED OF:

| | | | |
|---|---|---|---|
| ZIRARI MOUNIR | Professor | Medea University | President |
| ALLICHE MOUNIR | Professor | Medea University | Research Supervisor |
| REBHI REDHA | MCA | Medea University | Research Cosupervisor |
| BENAROUS ABDELLAH | Professor | Blida 1 University | Examiner |
| CHIBA YOUNES | Professor | Medea University | Examiner |

RÉPUBLIQUE ALGÉRIENNE DÉMOCRATIQUE ET POPULAIRE

MINISTÈRE DE L'ENSEIGNEMENT SUPÉRIEUR ET DE LA RECHERCHE SCIENTIFIQUE

UNIVERSITÉ YAHIA FARES DU MÉDÉE

FACULTÉ DE TECHNOLOGIE

DÉPARTEMENT DE GÉNIE MÉCANIQUE

Cette thèse intitulée :

# Contribution à l'étude numérique des écoulements non newtoniens multiphasiques dans un canal à milieu poreux

EST PRÉSENTÉE EN VUE DE L'OBTENTION

DU DIPLÔME DE DOCTORAT EN GÉNIE MÉCANIQUE

Option : Énergétique

Par

**ZID Islam**

Soutenue le : 25/04/2026

DEVANT LE JURY COMPOSÉ DE :

| | | | |
|---|---|---|---|
| ZIRARI MOUNIR | Professeur | Université de Médéa | Président |
| ALLICHE MOUNIR | Professeur | Université de Médéa | Directeur de recherche |
| REBHI REDHA | MCA | Université de Médéa | Co-directeur de recherche |
| BENAROUS ABDELLAH | Professeur | Université de Blida 1 | Examinateur |
| CHIBA YOUNES | Professeur | Université de Médéa | Examinateur |


بسم الله الرحمن الرحيم
Sidi

DEDICATIONS

This work is dedicated to my beloved mother, Hayat, and my father, Djenaihi, whose unwavering support and sacrifices made this journey possible; to my brothers, Ahmed Sasi and Amir Abdelkader; and to my sisters, Ines and Aya, for their constant encouragement and love.

**ACKNOWLEDGMENT**

In the name of ALLAH, the Most Gracious, the Most Merciful.

Alhamdulillah. All praise and gratitude belong to ALLAH (SWT), the Almighty, for His boundless blessings, divine guidance, and the fortitude bestowed upon me throughout the completion of this doctoral thesis. I am profoundly aware that this scholarly endeavor would not have come to fruition without His infinite mercy, grace, and will.

First and foremost, I express my profound appreciation to my supervisor, **Professor Alliche Mounir**, for his exceptional expertise, insightful counsel, and constant encouragement. His constructive guidance and steadfast support have been instrumental in shaping the trajectory of this work. I feel truly privileged to have benefited from his mentorship, which has significantly enriched both my academic knowledge and professional growth.

My sincere thanks also go to my co-supervisor, **Dr. Rebhi Redha**, for his generosity, constant availability, and significant intellectual contributions. His original ideas, meticulous proofreadings, and thoughtful suggestions have substantially enhanced the quality and rigour of this thesis. I am deeply indebted to him for his continuous assistance and commitment.

I also wish to express my sincere gratitude to **Mr. Alilat Djamel** and **Mr. Khir Saleh** for their valuable assistance. Their dedication and willingness to share their expertise played a vital role in the successful completion of this endeavor.

My heartfelt appreciation extends to Pr. **ZIRARI Mounir**, who graciously agreed to chair the examination jury. I am also grateful to Pr. **BENAROUS ABDELLAH** and Pr. **CHIBA YOUNES** for accepting the invitation to serve as examiners and for the keen interest they have shown in my research, despite their numerous professional commitments.

Last but certainly not least, I owe my deepest love and gratitude to my family for their unconditional support, boundless patience, and sacrifices. Their unwavering belief in my potential has been my primary source of strength and motivation throughout this arduous journey.

To all those who have contributed, directly or indirectly, to the completion of this thesis, please accept my sincerest thanks. Your contributions have been truly meaningful, and I remain deeply appreciative of the role each of you has played in bringing this work to fruition.

With heartfelt gratitude, ZID Islam

## ABSTRACT

This thesis presents a numerical investigation of natural convection in a tiltable square porous enclosure subjected to an external magnetic field and saturated with a non-Newtonian nanofluid. The vertical walls of the cavity have two different and constant temperatures, while the horizontal walls are considered thermally insulated and impermeable. The fluid flow within the porous medium is modeled using the Dupuit–Darcy formulation coupled with the Boussinesq approximation, whereas the Carreau–Yasuda model is employed to capture the rheological behavior of the non-Newtonian nanofluids under consideration. The governing partial differential equations, along with the corresponding boundary conditions, are numerically solved using the finite difference method (FDM) for enhanced computational accuracy.

Two types of nanofluids are examined: two simple nanofluids—SWCNT–water and $Al_2O_3$–water—and one hybrid nanofluid, ($Al_2O_3$+Cu)–water. The study explores the flow field, heat transfer performance, and apparent viscosity variations within the cavity across a wide range of parameters, including the four Carreau–Yasuda parameters, the Darcy–Rayleigh number, the nanoparticle volume fraction, the Hartmann number, the inertial effect parameter, and the inclination angle of the cavity.

The results reveal that the Carreau–Yasuda rheological parameters significantly influence both flow dynamics and heat transfer rates. As the fluid becomes more shear-thinning, the flow circulation intensifies, resulting in enhanced convective heat transfer. Conversely, higher values of the Hartmann number and the inertial parameter suppress fluid motion and diminish heat transfer, with thermal conduction becoming dominant at elevated values.

While the shear-thinning behavior improves heat transport, a strong magnetic field counteracts this enhancement by stabilizing the flow. The 30° inclination angle is identified as the optimal configuration for maximizing natural convection. Among the tested fluids, the SWCNT–water nanofluid demonstrates superior thermal performance due to its combination of high thermal conductivity and low apparent viscosity, whereas the hybrid nanofluid ($Al_2O_3$+Cu)–water exhibits weaker thermal efficiency owing to its higher viscosity and stronger inertial interactions despite its improved conductivity

**Keywords**: porous medium, non-Newtonian fluid, square cavity, Inertial effect parameter, Magnetic field, Dupuit-Darcy model, Carreau–Yasuda model

**RÉSUMÉ**

Cette thèse présente une étude numérique de la convection naturelle dans une cavité carrée poreuse inclinée, soumise à un champ magnétique externe et saturée par un nanofluide non newtonien. Les parois verticales de la cavité sont maintenues à deux températures constantes et distinctes, tandis que les parois horizontales sont considérées adiabatiques et imperméables.

L'écoulement du fluide à travers le milieu poreux est modélisé à l'aide de la formulation de Dupuit–Darcy, couplée à l'approximation de Boussinesq, tandis que le modèle de Carreau–Yasuda est employé pour décrire le comportement rhéologique des nanofluides non newtoniens étudiés. Le système des équations différentielles partielles gouvernantes, ainsi que les conditions aux limites associées, est résolu numériquement à l'aide de la méthode des différences finies (MDF) afin d'assurer une meilleure précision de calcul.

Deux types de nanofluides sont examinés : deux nanofluides simples — SWCNT–eau et $Al_2O_3$–eau — ainsi qu'un nanofluide hybride, ($Al_2O_3$+Cu)–eau. L'étude analyse le champ d'écoulement, la performance du transfert de chaleur et les variations de la viscosité apparente dans la cavité pour un large éventail de paramètres, incluant les quatre paramètres du modèle de Carreau–Yasuda

le nombre de Darcy–Rayleigh, la fraction volumique des nanoparticules, le nombre de Hartmann , le paramètre d'inertie et l'angle d'inclinaison de la cavité.

Les résultats montrent que les paramètres rhéologiques du modèle de Carreau–Yasuda exercent une influence significative sur la dynamique de l'écoulement et le taux de transfert de chaleur. Lorsque le fluide présente un comportement plus amincissant par cisaillement, la circulation s'intensifie, ce qui entraîne une amélioration du transfert thermique par convection. À l'inverse, des valeurs élevées du nombre de Hartmann et du paramètre d'inertie réduisent la mobilité du fluide et affaiblissent la convection naturelle, la conduction thermique devenant prédominante à des valeurs importantes de ces paramètres.

Bien que le comportement d'amincissement par cisaillement favorise le transport de chaleur, un champ magnétique intense atténue cet effet en stabilisant l'écoulement. L'angle d'inclinaison de 30° a été identifié comme la configuration optimale pour maximiser la convection naturelle. Parmi les fluides testés, le nanofluide SWCNT–eau présente la meilleure performance thermique grâce à sa forte conductivité thermique et à sa faible viscosité apparente, tandis que le nanofluide hybride ($Al_2O_3$+Cu)–eau affiche une efficacité thermique moindre en raison de sa viscosité plus élevée et de ses interactions inertielles plus marquées, malgré une conductivité améliorée.

**Mots-clés** : milieu poreux, fluide non-Newtonien, cavité carrée, Paramètre d'effet inertiel, Champ magnétique, Modèle de Dupuit-Darcy, Modèle de Carreau-Yasuda

**ملخص**

تُعنى هذه الأطروحة بدراسة عددية للحمل الحراري الطبيعي داخل حاوية مسامية مربعة الشكل قابلة للإمالة بالنسبة للمستوى الأفقي، تخضع لتأثير مجال مغناطيسي خارجي، ومشبعة بسائل نانوي غير نيوتوني. ، يتميز الجدران الرأسيان للتجويف بدرجتي حرارة مختلفتين وثابتتين، في حين تعتبر الجدران الأفقية معزولة حرارياً وغير منفذة.تم اعتماد نموذج ديبوي–دارسي مقترنًا بتقريب بوسينسكي لنمذجة تدفق المائع داخل الوسط المسامي، في حين استُخدم نموذج كارو–ياسودا لوصف السلوك الريولوجي للسوائل غير النيوتونية قيد الدراسة. جرى حل النظام الحاكم من المعادلات التفاضلية وشروطها الحدّية باستخدام منهج الفروق المنتهية لتحقيق الدقة العددية المطلوبة.

تضم الدراسة نوعين من السوائل النانوية وهي البسيطة وتتمثل فيSWCNT-ماء و $Al_2O_3$-ماء والنوع الثاني هو النانوي الهجين–(Al2O3+Cu) ماء. تم تحليل سلوك التدفق وانتقال الحرارة وتغيرات اللزوجة داخل الحاوية عبر نطاق واسع من المعاملات الفيزيائية، شملت معاملات نموذج كارو–ياسودا ، ورقم رايلي–دارسي ، ونسبة الحجمية للجسيمات النانوية ، ورقم هارتمان ، ومعامل القصور الذاتي ، إضافةً إلى زاوية ميل التجويف

أظهرت النتائج أن المعاملات الريولوجية لنموذج كارو–ياسودا تؤثر تأثيرًا جوهريًا على ديناميكية التدفق ومعدل انتقال الحرارة بالحمل الطبيعي؛ إذ يؤدي ازدياد حساسية المائع للتخفيف بالقص إلى تعزيز دوران المائع ورفع كفاءة الحمل الحراري. بالمقابل، يتسبب كلٌّ من ازدياد رقم هارتمان ومعامل القصور الذاتي في تثبيط الحركة الدورانية وتقليل معدلات انتقال الحرارة، حيث تصبح آلية التوصيل الحراري هي السائدة عند القيم العليا للعاملين الأخيرين.

في حين أن سلوك التخفيف الناتج عن القص للسائل النانوي يعزز انتقال الحرارة، فإن المجال المغناطيسي القوي يمكن أن يحيد هذه الفوائد عبر تثبيط شدة التدفق. تم تحديد زاوية 30°درجة باعتبارها الميل الأمثل لتعظيم الحمل الحراري الطبيعي داخل الحاوية. من بين الموائع المدروسة، أظهر مائع SWCNT–ماء أفضل أداء حراري بفضل جمعه بين التوصيل الحراري المرتفع واللزوجة الظاهرية المنخفضة، في حين قدّم السائل النانوي الهجين (Al2O3+Cu) –ماء أداءً أضعف نسبيًا نتيجة لارتفاع لزوجته الظاهرية وتأثره الأقوى بالقصور الذاتي رغم تحسّن موصليته الحرارية..

**الكلمات المفتاحية**: ، وسط مسامي، مائع غير نيوتوني.،تجويف مربع، معامل تأثير القصور الذاتي، المجال المغناطيسي، نموذج ديبوي-دارسي، نموذج كاريو-ياسودا

# TABLE OF CONTENTS

**DEDICATIONS** ..... **i**

**ACKNOWLEDGMENT** ..... **ii**

**ABSTRACT** ..... **iii**

**RÉSUMÉ** ..... **iv**

**ملخص** ..... **v**

**TABLE OF CONTENTS** ..... **vi**

**LIST OF FIGURES** ..... **ix**

**LIST OF TABLES** ..... **xii**

**NOMENCLATURE** ..... **xiii**

**GENERAL INTRODUCTION** ..... **1**

**1. CHAPTER I : Fundamentals and Current State of Research.** ..... **3**

.1.1 Generality on porous media ..... 3

1.1.1. Definition of Porous Media ..... 3

.1.1.2 R.E.V. and properties of porous media ..... 3

.1.1.3 Classification of Porous Media ..... 6

1.1.4. Momentum Equation Models ..... 7

1.2. Generality on nanofluids ..... 8

1.2.1. Classification of nanofluids ..... 8

1.2.2. Preparation of nanofluids ..... 11

1.2.3. Modeling heat transfer in nanofluids: ..... 12

1.2.4. Thermophysical Properties of Nanofluids ..... 13

.1.3 Non-Newtonian Fluids ..... 17

.1.3.1 Basic Rheological Concepts ..... 17

.1.3.2 Non-Newtonian Fluids ..... 18

1.3.3. Constitutive Models for Non-Newtonian Fluids ..... 20

1.4. magnetohydrodynamics (MHD) .....23

1.4.1. Definition .....23

1.4.2. The MHD Equations and Essential Dimensionless Parameters .....24

.1.5 Current State of Research .....26

**2. CHAPTER II :PHYSICAL MODELING AND GOVERNING MATHEMATICAL FORMULATION.....33**

2.1. Problem description.....33

2.2. Model Simplifications and Assumptions .....33

2.3. Mathematical formulation .....34

2.3.1. Continuity equation .....34

2.3.2. Motion equation .....35

2.3.3. Energy equation.....35

2.4. Boundary conditions .....42

2.4.1. Hydrodynamic boundary conditions .....42

2.4.2. Thermal boundary conditions.....42

2.5. Quantifying Heat Transfer: Local and Average Nusselt Number Analysis .....42

2.5.1. Local Nusselt Number.....42

2.5.2. Average Nusselt Number .....42

**3. CHAPTER III :NUMERICAL METHODOLOGY .....44**

3.1. Thermal boundary conditions discretization .....45

3.1.1. For the adiabatic and impermeable walls: .....45

3.1.2. For active walls .....45

3.2. Energy equation discretization .....45

3.2.1. Implicit Scheme in the x-Direction and Explicit in the y-Direction .....46

3.2.2. Implicit Scheme in the y-Direction and Explicit in the x-Direction .....47

3.3. Momentum equation discretization .....48

3.4. Velocity fields discretization.....49

3.5. Discretization of velocity boundary conditions .....49

3.6. Calculation algorithm.....50

**4. CHAPTER IV: PRESENTATION AND DISCUSSION Of RESULTS.....52**

4.1. First Section: The Non-Newtonian SWCNT–Water Nanofluid .....52

4.2. Second part: The Non-Newtonian hybrid nanofluid (Cu-Al2O3- water) .....70

**5. CHAPTER V: CONCLUSION AND PERSPECTIVES.....90**

5.1. Conclusion.....90

5.2. PERSPECTIVES: .....91

**REFERENCES.....93**

LIST OF FIGURES

Figure 1.1:Top: Examples of natural porous materials: A) beach sand, B) sandstone, C) limestone, D) rye bread, E) wood, and F) human lung . Bottom: Granular porous materials used in the construction industry, 0.5-cm-diameter spheres (left), and 1-cm-size crushed limestone (right) (Nield & Bejan, 2006).....3

Figure 1.2: The concept of the Representative Elementary Volume (REV) illustrates its intermediate scale in relation to the dimensions of the flow domain and pore structures. .....4

Figure 1.3 : 2D Sketch for the tortuosity concept (Fu et al., 2021) .....6

Figure 1.4 Schematic representation of a unidirectional sheared flow .....17

Figure 1.5 :The shear stress—shear rate curve for incompressible Newtonian fluids.....18

Figure 1.6: types of non-Newtonian time independent fluids.....19

Figure 1.7:types of non-Newtonian time dependent fluids.....20

Figure 1.8: Viscosity behaviour as modelled by the Carreau–Yasuda model(Morrison, 2001).....23

Figure 1.9: Interaction of a magnetic field and a moving conductor.....24

Figure 2.1: Schematic representation of the problem .....33

Figure 3.1 Mesh size of the study area in (i,j) .....44

Figure 4.1 validation in terms of streamline (in the left), isotherms (in the middle and the apparent viscosity) to what reported by (Khechiba et al., 2017)(a) with this present work (b) at $RT$ = 70, $n = 0.6$, $s = 0.01$, $E = 0.6$ and $a = 2$.....53

Figure 4.2 validation in terms of streamline, isotherms and the apparent viscosity to what reported by (Djamel et al., 2023) (Top) with this present work (Bottom) at $R\,T = 200$, $n = 0.8$, $s = 0.01$, $E = 0.6$, $G = 0.5$ and $a = 2$.....54

Figure 4.3 Validation in terms of streamline for different $Ha$ to with Mahmud & Fraser, 2004.....55

Figure 4.4 Variation of Hartmann number (Ha) for streamlines (4a), isotherms (4b) and the apparent viscosity (4c) with the following parameters $RT = 200$, $G = 0.5$, $\gamma = 0, \phi = 0.05$, $E = 0.6, n = 0.8\ s = 0.01\ and\ a = 2$. .....56

Figure 4.5 Variation of the power law index(n) for streamlines (5a), isotherms (5b) and the apparent viscosity (5c) with the following parameters $RT = 200, Ha = 2$ , $G = 0.5, \phi = 0.05$, .....58

Figure 4.6 effect of varying the concentration of SWCNTs nanoparticles on the streamlines (6a), isotherms (6b) and the apparent viscosity (6c) with the following parameters $RT = 200, Ha = 2$ , $G = 0.5, n = 0, \gamma = 0°, E = 0.6, s = 0.01\ and\ a = 2$ .....59

Figure 4.7 variation of stream function at the center$\Psi max$ (7a) ,the maximum average Nusselt number $NuL$(7b), apparent viscosity $\eta nf$(7c) versus n for various values of Ha, with $RT = 200, G = 0.5\ \phi = 0.05, \gamma = 0°, E = 0.6, s = 0.01\ and\ a = 2$ .....61

Figure 4.8 relationship between the time constant parameter E and of stream function at the center$\Psi max$ (8a) ,the maximum average of Nusselt number $Nul$ (8b), and the apparent viscosity (8c) for various Hartmann numbers (Ha) at $RT = 200, G = 0.5\ \phi = 0.05, \gamma = 0°, n = 0.6, s = 0.01\ and\ a = 2.$.....62

Figure 4.9 Variation of stream function at the center$\Psi max$ (09a), the maximum average Nusselt number $NuL$(09b), apparent viscosity $\eta nf$(09c) versus the parameter (a) for various values of $Ha$ at $RT$ = 200, ϕ=0.05, $s = 0.01$, $E = 0.6$ and $n = 0.6$. .....63

Figure 4.10. variation of stream function at the center$\Psi max$ (10a) ,the maximum average Nusselt number $NuL$(10b), apparent viscosity $\eta nf$(10c) versus the parameter (s) for various values of $Ha$ at $RT = 200, G = 0.5\ \phi = 0.05, \gamma = 0°, E = 0.6, s = 0.01\ and\ a = 2$.....64

Figure 4.11. . variation of stream function at the center$\Psi max$ (11a) ,the maximum average Nusselt number $NuL$(11b), apparent viscosity $\eta nf$(11c) versus the parameter (G) for various values of Ha at $RT = 200, n = 0.6\ \phi = 0.05, \gamma = 0°, E = 0.6, s = 0.01\ and\ a = 2.$ .....66

Figure 4.12 variation of stream function at the center$\Psi max$ (12a) ,the maximum average Nusselt number $NuL$(12b), apparent viscosity $\eta nf$(12c) versus $\phi$ for various values of $Ha$ at $RT = 200, G = 0.5\ n = 0.6, \gamma = 0°, E = 0.6, s = 0.01\ and\ a = 2.$.....67

Figure 4.13 Variation of stream function at the center $\Psi max$ (13a), the maximum average Nusselt number $NuL$(13b), apparent viscosity $\eta nf$(13c) versus $\gamma$for various values of $Ha$ at $RT = 200, G = 0.5\ \phi = 0.05, n = 0.6, E = 0.6, s = 0.01\ and\ a = 2.$ .....69

Figure 4.14 comparison between SWCNT and $AL_2O_3$ nanoparticles on the maximum absolute stream function$\Psi max$(14a) the average Nusselt number $Nul$ (14b) and the apparent viscosity at $RT = 200, G = 0.5\ \phi = 0.05, \gamma = 0°, E = 0.6, s = 0.01, and\ a = 2$ .....70

Figure 4.15:Variation of the average Nusselt number and maximum stream function with grid size for the grid independence test.....71

Figure 4.16 :Comparison in terms of streamline for different $RT$ values between the current results (b) and those of (Revnic et al., 2024) (a) at $\phi hnf$=0.04 , G=0, Ha=0, n=1.....72

Figure 4.17 streamlines (a) , isotherms (b) , and (c) apparent viscosity contours at various values of power-law index (n) at $RT$=200,G=0.5,Ha=4,a=2,E=0.6 ,s=0.01 and $\phi hnf = 0.04$.....73

Figure 4.18 streamlines (a) , isotherms (b) , and (c) apparent viscosity contours at various values of Hartmann numbers (Ha)at $RT$=200,G=0.5,n=0.4,a=2,E=0.6 ,s=0.01 and $\phi hnf = 0.04$ .....74

Figure 4.19 :streamlines (a) , isotherms (b) , and (c) apparent viscosity contours at various values of nanoparticles percentage $\phi hnf$ at $RT$=200,G=0.5,n=0.4,a=2,E=0.6 ,s=0.01 and $Ha = 4$...76

Figure 4.20: Profiles of the apparent viscosity versus the X-axis with various value of: (a) Hartmann number, (b)inertial parameter G and (c) nanoparticle volumetric fraction, at Y=0.....77

Figure 4.21:Profiles of the apparent viscosity versus the X-axis under the influence of: (a) the power law index a , (b) time constant parameter E, (c) viscosity ratio parameter s and (d) dimensionless parameter of the Carreau-Yasuda model a, at Y=0.....78

Figure 4.22:The dependency of: (a) the maximum absolute stream function; (b) the average Nusselt number on the left wall; and (c) the apparent viscosity of the hybrid nanofluid on the function of the concentration percentage (ϕ) and various power law index values (n) .....79

Figure 4.23:The dependency of: (a) the maximum absolute stream function; (b) the average Nusselt number on the left wall; and (c) the apparent viscosity of the hybrid nanofluid on the function of the concentration percentage (ϕ) and various dimensionless time constant values (E) ....80

Figure 4.24:The dependency of: (a) the maximum absolute stream function; (b) the average Nusselt number on the left wall; and (c) the apparent viscosity of the hybrid nanofluid on the function of the concentration percentage (ϕ) and various viscosities ratio values (s) .....81

Figure 4.25:The dependency of: (a) the maximum absolute stream function; (b) the average Nusselt number on the left wall; and (c) the apparent viscosity of the hybrid nanofluid on the function of the concentration percentage (ϕ) and various dimensionless parameter values (a).....82

Figure 4.26: The dependency of: (a) the maximum absolute stream function; (b) the average Nusselt number on the left wall; and (c) the apparent viscosity of the hybrid nanofluid on the function of the inertial parameter and various volumetric fraction values (ϕ).....83

Figure 4.27: The dependency of: (a) the maximum absolute stream function; (b) the average Nusselt number on the left wall; and (c) the apparent viscosity of the hybrid nanofluid on the function of Hartmann number(Ha) and various volumetric fraction values (ϕ) .....84

Figure 4.28:The dependency of: (a) the maximum absolute stream function; (b) the average Nusselt number on the left wall; and (c) the apparent viscosity of the hybrid nanofluid on the function of Rayleigh number($RT$) and various volumetric fraction values (ϕ).....86

Figure 4.29:The dependency of: (a) the maximum absolute stream function; (b) the average Nusselt number on the left wall; and (c) the apparent viscosity of the hybrid nanofluid on the function of the Inclination angle ($\gamma$) and various volumetric fraction values (ϕ) .....87

Figure 4.30 comparison between the hybrid nanofluid ($Al_2O_3$+Cu/water),the nanofluids ($Al_2O_3$/water)and (SWCNT/water) in term of (a) the maximum absolute stream function; (b) the average Nusselt number on the left wall; and (c) the apparent viscosity.....89

LIST OF TABLES

Table 1-1:The most used type of nanoparticles and base fluid.....9
Table 1-2 non-exhaustive list of nanoparticle-based fluid combinations.....10
Table 1-3:Comparison of the advantages and disadvantages of one-step and two-step methods.....11
Table 1-4:List of Nondimensional Parameters.....26
Table 2-1:Thermophysical properties of base fluid (water) and nanoparticles used.....38
Table 4-1: the convergence tests conducted for $|\Psi|_{max}$ and $\overline{Nu_l}$ at $Ha=2$, $G=0.5$, $R_T=200$ and $n=1$.....52
Table 4-2 comparison between the present results and those of (Khechiba et al., 2017) regarding of $|\Psi|_{max}$ and $Nu_m$ across various n values.....53
Table 4-3 comparison between the present results and those of Djamel et al., 2023 regarding of across various n values.....54
Table 4-4an additional comparative analysis with the study conducted by Alilat, Alliche, Rebhi, & Chamkha, 2020. across various values of Ha.....54
Table 4-5: Comparison of $\overline{Nu}$ with some previous numerical results.....71

NOMENCLATURE

| | |
|---|---|
| $B$ | Applied magnetic field, $N.m^1.A^1$ |
| $C_p$ | specific heat, J·kg$^{-1}$·K$^{-1}$ |
| $d$ | particle size (diameter), m, |
| $D$ | Molecular diffusion coefficient, $m^2.s^1$ |
| $g$ | gravitational acceleration vector,m·s$^{-2}$ |
| $I$ | Electric current ,A |
| $k$ | thermal conductivity, $W.m^{-1}.K^{-1}$) |
| $K$ | permeability of porous medium, $m^2$ |
| $\widetilde{K}$ | constant solute flux per unit area, $kg.m^1.s^1$, |
| $L, H$ | dimensions of cavity, m |
| $p$ | Pressure, N·m$^{-2}$ |
| $T$ | Temperature, k |
| $u$ | velocity $x$-component, m·s$^{-1}$ |
| $v$ | velocity $y$-component, m·s$^{-1}$ |
| $V$ | velocity vector, m·s$^{-1}$ |
| $x, y$ | cartesian coordinates |

**Greek symbols**

| | |
|---|---|
| $\alpha$ | fluid thermal diffusivity, $m^2/s$ |
| $\beta$ | thermal expansion coefficient, K$^{-1}$, |
| $\xi$ | inclination angle of the of applied magnetic field (°), |
| $\gamma$ | inclination angle of the cavity to the horizontal (°), |
| $\rho$ | density of fluid, $kg/m^3$ |
| $\dot{\gamma}'$ | shear rate magnitude |
| $\varepsilon$ | porosity of the porous medium |
| $\mu_a$ | non-Newtonian nanofluid apparent viscosity, kg·m$^{-1}$·s$^{-1}$ |
| $\mu_0$ | zero-shear rate dynamic viscosity |
| $\mu_\infty$ | infinite-shear rate dynamic viscosity |
| $\eta$ | Carreau–Yasuda nondimensional apparent viscosity |
| $\upsilon$ | kinematic viscosity, m$^2$ s$^{-1}$ |
| $\tau$ | time, s |
| $\phi$ | nanoparticle volumetric fraction |
| $\sigma$ | Electrical conductivity , $\Omega^{-1}$.m$^{-1}$ |
| $\Psi$ | stream function, |
| $\theta$ | temperature |

**Dimensionless quantities**

| | |
|---|---|
| $a$ | dimensionless Carreau–Yasuda model parameter |
| $E'$ | dimensional time constan |
| $n$ | Power law index |
| $s$ | ratio of the infinite-to-zero shear-rate viscosities, s = $\mu_\infty/\mu_0$ |

| | |
|---|---|
| $t$ | time |
| $U, V$ | velocity components |
| Y | Cartesian coordinate in the y direction |
| X | Cartesian coordinate in the *x* direction |

**Dimensionless Numbers**

| | |
|---|---|
| $G$ | parameter that measures the inertial effects |
| $Nu$ | Nusselt number |
| $\overline{Nu_L}$ | average Nusselt number of the left wall |
| $\overline{Nu_R}$ | average Nusselt number of the right wall |
| $Nu_m$ | average Nusselt number |
| $R_m$ | Magnetic Reynolds number |
| $R_T$ | Darcy–Rayleigh number |
| $Ha$ | Hartmann number |

**Subscript**

| | |
|---|---|
| 0 | reference value |
| $f$ | Base fluid |
| $C$ | cold |
| $f$ | fluid |
| $h$ | hot |
| $hnf$ | Hybrid nanofluid |
| $max$ | maximum value |
| $nf$ | nanofluid |
| $p$ | Nanoparticle |

**Abbreviations**

| | |
|---|---|
| CNT | Carbon Nanotube |
| CY | Carreau–Yasuda |
| SWCNT | cold |
| $f$ | fluid |
| $h$ | hot |

# GENERAL INTRODUCTION

# GENERAL INTRODUCTION

Natural convection heat transfer is a fundamental physical phenomenon resulting from density variations in a fluid caused by temperature differences. When a fluid experiences a temperature gradient, the more heated, less dense fluid ascends while the colder, denser fluid descends, establishing a continuous circulation pattern along with a convective current (Incropera et al., 1996). This process is essential in numerous natural and artificial systems, including atmospheric and oceanic circulations as well as diverse industrial uses. Comprehending and regulating convective heat transport is crucial for researchers and engineers aiming to improve thermal performance and devise effective heat management solutions.

The search of enhanced heat transfer efficiency in recent decades has pushed the investigation of innovative working fluids beyond conventional coolants such as mineral oils, water, and ethylene glycol. The revolutionary research by (Choi & Eastman, 1995), who established the nanofluids concept—suspensions of solid particles at the nanoscale (usually < 100 nm) scattered throughout base fluids.—made a huge progress in this medium. Recently, nanofluids have become a promising alternative to traditional heat transfer fluids primarily due to their superior thermophysical features, such as increased thermal conductivity, improved convective coefficients, and consistent dispersion behavior. Various types of nanofluids have been developed, including metallic, metal oxide, and carbon-based nanofluids(Das et al., 2006). Recently, hybrid nanofluids— consisting of two or more distinct nanoparticles— have attracted significant attention due to their capacity to enhance both thermal and rheological properties synergistically(Suresh et al., 2011).

Concurrently with investigations on nanofluid, porous media have also been recognized for their significant role in heat transfer processes. Engineering applications widely use porous materials, such as catalytic reactors, filtration devices, and geothermal systems. The existence of a porous matrix enhances heat transmission primarily by increasing the effective contact surface area between the solid matrix and the liquid phase, thereby facilitating increased energy exchange(Nield & Bejan, 2006). Furthermore, the integration of porous media with nanofluids has demonstrated utility in enhancing thermal efficiency in heat exchange systems.(Bianco et al., 2015)

Another major class of fluids that has received important attention in both academia and industry is non-Newtonian fluids. In contrast to Newtonian fluids, whose viscosity remains constant, non-Newtonian fluids display diverse rheological behaviors—such as shear-thinning, shear-thickening, and viscoelasticity —depending on the imposed shear rate. (Bird et al., 1987)These fluids are ubiquitous in

numerous industrial applications and consumer products, such as polymeric melts, coatings, and lubricants, biological fluids, ketchup, and fruit juices. The sophisticated flow behavior of this type of fluid has motivated scientists to construct a variety of rheological models, such as the Power-Law, Carreau–Yasuda, and Bingham models, aimed at improving understanding and prediction of their behavior under distinct flow and thermal conditions(Chhabra & Richardson, 2011).

The main objective of this thesis is to numerically investigate natural convection heat transfer in a square porous enclosure filled with non-Newtonian nanofluids, accounting for the combined effects of magnetic field, porous medium, and complex rheological behavior. The fluids considered in this study include the single-walled carbon nanotube–water (SWCNT–water) nanofluid, the aluminum oxide–water ($Al_2O_3$–water) nanofluid, and the hybrid nanofluid ($Al_2O_3$ + Cu–water).

The enclosure is subjected to a horizontal temperature gradient, with the left vertical wall maintained at a constant hot temperature ($T_h$) and the right vertical wall at a constant cold temperature ($T_c$), while the horizontal walls are thermally insulated. The flow within the porous medium is modeled using the Dupuit–Darcy formulation under the Boussinesq approximation, while the non-Newtonian behavior of the working fluids is described using the Carreau–Yasuda model. The resulting governing equations are solved numerically using the finite difference method (FDM), implemented in a FORTRAN computational code.

This study aims to analyze the influence of the governing dimensionless parameters, including the Rayleigh number, Hartmann number, inertial parameter, Carreau–Yasuda parameters, nanoparticle volume fraction , and cavity inclination angle, on flow intensity, heat transfer rate, and apparent viscosity distribution. In addition, a comparative analysis is conducted to evaluate the thermal performance of mono and hybrid nanofluids under identical operating conditions.

This thesis is organized into five chapters. The first chapter introduces the research context and reviews the relevant literature. The second chapter presents the mathematical formulation of the problem, including the governing equations and boundary conditions. The third chapter describes the numerical methodology and computational procedure. The fourth chapter discusses the results obtained and provides a detailed analysis. Finally, the fifth chapter summarizes the main findings and suggests perspectives for future work.

# CHAPTER 1

# Fundamentals and Current State of Research

# 1. CHAPTER I : Fundamentals and Current State of Research.

## 1.1. Generality on porous media

### 1.1.1. Definition of Porous Media

Porous media are solid materials containing a network of interconnected voids or pores, which allow for the transport of one or more fluid phases (Bear, 1972). Porous structures are encountered in various natural and engineered systems, as presented in Figure 1.1

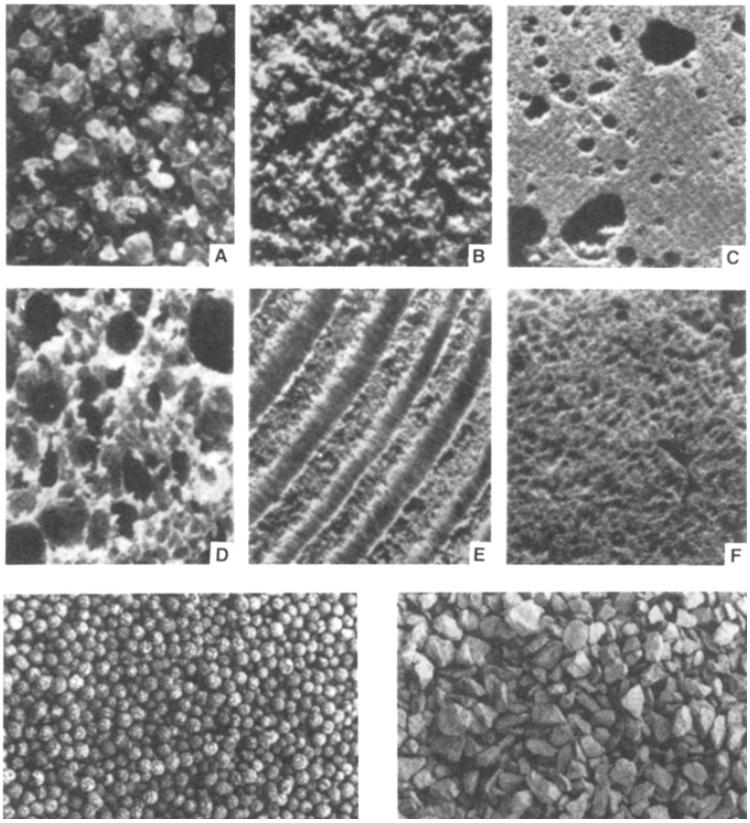



*Figure 1.1:Top: Examples of natural porous materials: A) beach sand, B) sandstone, C) limestone, D) rye bread, E) wood, and F) human lung . Bottom: Granular porous materials used in the construction industry, 0.5-cm-diameter spheres (left), and 1-cm-size crushed limestone (right) (Nield & Bejan, 2006)*

### 1.1.2. R.E.V. and properties of porous media

To describe the macroscopic behavior of transport processes in porous media, it is essential to define a Representative Elementary Volume (REV). The REV is the smallest volume over which physical properties such as porosity, permeability, and thermal conductivity can be averaged to yield values representative of the bulk medium, independent of further volume increases. Below this scale, local

heterogeneities cause significant fluctuations in measured properties. However, once the REV threshold is reached, these fluctuations tend to average out, allowing for reliable continuum-level modeling (Bear, 1972)).

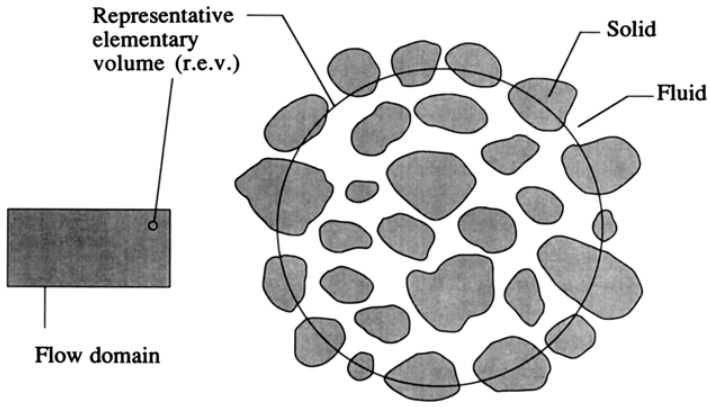



*Figure 1.2: The concept of the Representative Elementary Volume (REV) illustrates its intermediate scale in relation to the dimensions of the flow domain and pore structures.) (Nield & Bejan, 2006)*

Once the REV is established, it becomes meaningful to define and quantify the key transport properties of porous media, namely porosity, permeability, and tortuosity

#### 1.1.2.1 Porosity (ε)

Porosity, a macroscopic porous medium property, is the simplest geometrical descriptor of a porous medium. It is defined as the ratio of the void volume to the total volume of the medium:

$$\varepsilon = \frac{volume\,of\ pore\,space}{total\,sample\,volume} = 1 - \frac{V_s}{V_t} = \frac{V_p}{V_t} \qquad (1.1)$$

where ε represents the porosity of the medium, while Vs and Vt denote the volume of the solid phase and the total volume of the medium, respectively.

Two types of porosity are commonly distinguished:

- Total porosity includes all types of pores, whether they are connected or not, encompassing both effective and isolated pore spaces.
- Effective porosity, $\varepsilon_{eff}$ which considers only the interconnected pores that contribute to fluid flow and storage (Dullien, 1992; Heinemann & Mittermeir, 2013)

The porosity of a material varies significantly depending on its microstructure. For instance, dense metals may have porosities close to zero, while fibrous materials and thermal insulators may exhibit porosities approaching unity

#### 1.1.2.2 Permeability (K)

Permeability is a measure of a porous medium's ability to allow fluid flow through its pore network. It is an intrinsic property that depends solely on the geometry, size, and connectivity of the pores within the medium, and is therefore independent of the physical properties of the fluid flowing through it.

For granular porous media, the Carman–Kozeny theory, originally derived for packed beds, provides an estimate for permeability (Nield & Bejan, 2006)

$$K = \frac{\varepsilon^3 d_p^2}{180(1-\varepsilon)^2} \tag{1.2}$$

where:

$K$ : the permeability

$\varepsilon$ : the porosity,

$d_p$ is the mean particle diameter.

This equation assumes laminar flow and uniform particle packing and is widely used in chemical and petroleum engineering

#### 1.1.2.3 Tortuosity (τ)

Another key attribute of a porous material is its tortuosity (Figure 1.3), which quantifies the complexity of flow paths through a porous medium. It is defined as the ratio between the actual (effective) length of the fluid path and the straight-line length of the porous sample (Dullien, 1992):

$$\tau = \frac{effective\ length}{sample\ length} = \frac{L_e}{L} \tag{1.3}$$

where:

$\tau$ : the tortuosity,

$L_e$ : the effective path length,

$L$ : the geometric (straight-line) length.

Higher tortuosity implies more convoluted pathways, resulting in increased resistance to transport processes and convection

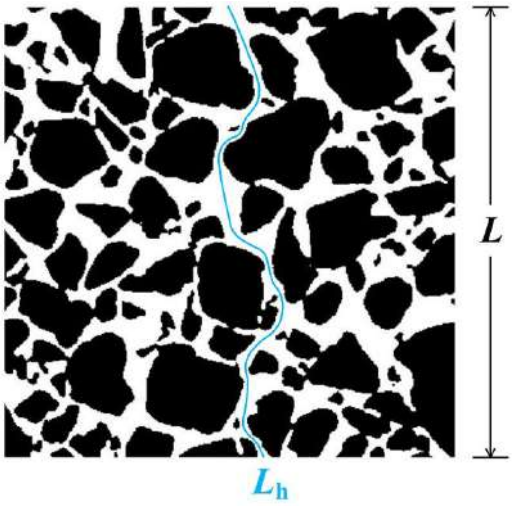



*Figure 1.3 : 2D Sketch for the tortuosity concept (Fu et al., 2021)*

### 1.1.3. **Classification of Porous Media**

Porous media can be classified according to various criteria, including their origin, physical form, structure, and material composition of the media. These classifications are important in comprehending and simulating fluid flow, heat conduction, and mechanical behavior in the porous structures. According to (Lofrano et al., 2020) the key classification schemes can be outlined in the following:

#### 1.1.3.1 Based on the Origin

- Natural porous media: They occur in nature and include soil, rocks, organs (kidneys and lungs), and other biological tissues.
- Synthetic porous media: are comprised of a diverse range of engineered materials, including polymer foams, ceramics, cementitious composites, and biomaterials. These materials are frequently designed for thermal, hydraulic, or mechanical performance specifications.

#### 1.1.3.2 Based on location

- In situ porous media: These are not disturbed in their natural or functional location, e.g., soil beds, charcoal beds, or zeolite beds.
- Ex situ porous media: These are extracted or intentionally inserted in technical systems, e.g., in filters or packed columns in separators and reactors.

#### 1.1.3.3 Based on the scale of solid matrix

- Macrostructured media: are composed of big particles or pieces of rocks, e.g., fragmented rocks, boulders, and karst.
- Micro- or nano-structured materials: are made up of very small particles, including adsorbents, biological tissues, and specially prepared porous membranes

#### 1.1.3.4 Based on the consolidation of constituents

- Consolidated porous media: The solid matrix is well bonded, e.g., cementitious materials, catalysts, or compacted clays.
- Unconsolidated porous media are uncompacted particles, for example, loose sediments or soils

#### 1.1.3.5 Depending on the Nature of the Components

- Granular media: Composed of approximately spherical or irregular particles, e.g., activated charcoal.
- Fibrous media are distinguished by the inclusion of elongated or filamentous material, like geotextiles and root systems.

### 1.1.4. Momentum Equation Models

The momentum equation governs the fluid motion within the porous medium. Several models have been developed depending on the fluid type, flow regime, and the assumptions regarding the medium's structure. The most common formulations are summarized below

#### 1.1.4.1 Darcy's Law

The earliest model for flow through porous media was developed by (Darcy, 1856) based on experiments using loosely packed, uniform granular media. His empirical relation describes the linear relationship between pressure gradient and fluid velocity under low Reynolds number conditions

$$-\frac{dp}{dx} = \frac{\mu}{K} u_D \tag{1.4}$$

where:

$p$: fluid pressure

$\mu$: dynamic viscosity

$K$: permeability of the porous medium

$u_D$: Darcy velocity

Darcy's law is valid for slow, viscous, steady, and incompressible flows, typically in the creeping flow regime

#### 1.1.4.2 Brinkman Model

To account for viscous shear effects and boundary-layer behavior near solid walls, (Brinkman, 1949)extended Darcy's law by including a Laplacian term:

$$-\frac{dp}{dx} + \rho g = \frac{\mu u}{K} + \mu_{eff} \nabla^2 u \tag{1.5}$$

This model bridges the gap between Darcy flow and the Navier–Stokes equations. The effective viscosity $\mu_{eff}$ may differ from the fluid viscosity $\mu$, Depending on the porosity and microstructure of the medium (Nield & Bejan, 2006)

#### 1.1.4.3 Forchheimer Model

(Forchheimer, 1901) introduced a nonlinear correction to Darcy's law to include inertial effects at higher Reynolds numbers:

$$-\frac{dp}{dx}+\rho g=\frac{\mu}{K}u+\frac{F\rho_f|u|u}{\sqrt{K}} \tag{1.6}$$

where:

$\rho_f$ : fluid density

$F$ : Forchheimer coefficient, an empirical parameter depending on the medium

This model is more accurate for transitional and inertial-dominated flows

#### 1.1.4.4 Darcy–Brinkman–Forchheimer Model (Generalized Model)

The most general formulation combines all previous effects—viscous diffusion, permeability resistance, and inertial drag:

$$\rho\left(\frac{\partial v}{\partial t}+u.\nabla u\right)=-\nabla p+\rho g+\mu\nabla^2 u-\frac{u}{K}u-\beta\rho|u|u \tag{1.7}$$

This equation is suitable for modeling a wide range of flow regimes in porous media, from creeping to moderately turbulent flow

## 1.2. Generality on nanofluids

Nanofluid refers to a colloidal suspension of nanoparticles, typically with diameters less than 100 nm, uniformly dispersed in a base fluid. Dr. Choi (Choi & Eastman, 1995) first introduced this term, marking the relatively recent emergence of this field. Incorporating these nano-sized particles into the base fluid significantly enhances thermal conductivity and other properties such as viscosity and heat transfer capabilities. Consequently, nanofluids present promising applications in various engineering and industrial processes, offering potential improvements in efficiency and performance

### 1.2.1. Classification of nanofluids

The classification of nanofluids can be approached from multiple perspectives, depending on specific characteristics and influencing factors. The subsequent sections delineate the principal criteria utilized for the categorization of nanofluids

#### 1.2.1.1 Classification Based on the Type of Nanomaterial

Nanofluids can be categorized by the type of nanomaterials dispersed within the base fluid, with researchers having explored many types of nanomaterials, each with distinct properties influencing the nanofluid's behavior. The choice of nanomaterials depends on several factors, including the application, toxicity, cost, and availability. The most commonly used types of nanoparticles are listed in Table 1-1

*Table 1-1:The most used type of nanoparticles and base fluid*

| Material (Symbol) | Thermal Conductivity W/(m·K) |
|---|---|
| **Pure Metal-Based** | |
| Aluminum (Al) | 247 (Chung, 2001) |
| Copper (Cu) | 398 (Chung, 2001) |
| Gold (Au) | 315 (Chung, 2001) |
| Silver (Ag) | 429 (Bobkov et al., 2008) |
| Silicon (Si) | 148 (Sarkar, 2011) |
| **Carbon-Based** | |
| Carbon Nanotubes (CNTs) | 2000 (Kwon & Kim, 2006) |
| Diamond (C) | 3300 (Sarkar, 2011) |
| Graphite | 2000 (Balandin, 2011) |
| **Metal Oxide-Based** | |
| Aluminum Oxide ($Al_2O_3$) | 40 (Shackelford & Alexander, 2000) |
| Copper Oxide (CuO) | 33 (Sarkar, 2011) |
| Silicon Dioxide ($SiO_2$) | 1.4 (Vajjha et al., 2010) |
| Titanium Dioxide ($TiO_2$) | 8.4 (Kim et al., 2007) |
| **Base Fluids** | |
| Water | 0.608 (Handbook, 2005) |
| Ethylene Glycol (EG/W) 40:60% | 0.257 (Perry, 1950)<br>0.404 (Sundar et al., 2014) |

#### 1.2.1.2 Classification Based on the Nanomaterial Composition

Nanofluids are engineered suspensions in which the dispersed phase may consist of a single type of nanoparticle, a combination of different nanoparticles, or a composite material integrating two or more distinct components. The classification of nanofluids is based on the composition of the dispersed nanomaterials, and they are generally divided into two categories: conventional (mononanofluids) and hybrid nanofluids

**a) Conventional (mononanofluids)**

mononanofluids are nanofluids that consist of a single type of nanoparticle uniformly dispersed within a base fluid. These systems can be formulated using any of the nanomaterials discussed previously, with particle size and concentration adjustable to meet specific requirements. Due to the

presence of only one nanoparticulate component, the overall behavior and performance of the nanofluid are directly dictated by the intrinsic properties of that single component, thereby simplifying both synthesis and characterization processes Table 1-2 presents a non-exhaustive list of nanoparticle-based fluid combinations synthesized by various research groups.(Ribeiro & Gruss, 2009)

*Table 1-2 non-exhaustive list of nanoparticle-based fluid combinations*

| | Acetone | Water | Ethylene Glycol | Oil | Toluene | Decene | Ethanol |
|---|---|---|---|---|---|---|---|
| Ag | | × | | × | | | |
| AlN | | | | | | | × |
| Au | | × | | | × | | |
| $Al_{70}Cu_{30}$ | | | × | | | | |
| Al2O3 | | × | × | × | | | |
| $Bi_2Te_3$ | | | | | | | |
| Diamond(C) | | × | | | | | |
| Graphite(C) | | × | | × | | | |
| CNTs | | × | | × | | × | |
| Fullerene(C) | | | | × | × | | |
| Cu | × | × | × | × | | | |
| CuO | | × | × | | | | |
| Fe | | | × | | | | |
| SiC | | × | | | | | |
| $SiO_2$ | | × | × | | | | |
| $TiO_2$ | | × | × | | | | |
| $WO_3$ | | | × | | | | |
| $ZrO_2$ | | × | | | | | |

**b) Hybrid nanofluids**

Hybrid nanofluids represent a progressive innovation in nanofluid technology, achieved by dispersing two or more distinct types of nanoparticles into a single base fluid. This combination leads to the formation of a nanocomposite structure that significantly enhances the thermophysical properties of the fluid beyond what is attainable with conventional nanofluids containing a single nanoparticle type. These improvements are largely attributed to synergistic interactions between the different nanoparticles, contributing to superior thermal conductivity characteristics. Depending on the synthesis method, hybrid nanofluids are generally classified into two categories, as detailed by (Bhanvase & Barai, 2021)

- **Nanomaterial mixture-based hybrid nanofluids :**

These nanofluids are formulated by physically mixing two or more distinct nanoparticles within a base fluid. The objective is to combine the unique properties of each nanoparticle type to achieve an improved overall thermal performance. Such mixtures, often referred to as binary or ternary systems, aim to enhance the heat transfer characteristics by exploiting the combined effects of their constituents

- **:Nanocomposite-based hybrid nanofluids :**

In contrast, nanocomposite-based hybrid nanofluids refer to materials composed of two or more constituents, with at least one dimension residing within the nanoscale. This method not only targets enhanced thermal conductivity but also aims to address common challenges such as nanoparticle agglomeration and sheet restacking, especially in carbon-based systems like graphene. By anchoring secondary particles on the surface of primary nanoparticles, the stability and dispersion uniformity of the nanofluid are significantly improved

### 1.2.2. **Preparation of nanofluids**

To date, numerous laboratory investigations have been undertaken regarding nanofluids, which have enabled the identification of their production methodologies, fundamentally categorized into two distinct approaches: the one-step method and the two-step method

#### **1.2.2.1 One-step method**

The one-step method involves the synthesis of nanoparticles directly within the base fluid, enabling immediate utilization without the necessity of drying or separating the nanomaterials from the fluid. Several techniques have been developed to prepare nanofluids in a single step, which can be broadly categorized into physical and chemical methods. However, it appears that the one-step preparation techniques are predominantly based on physical processes, likely to minimize the risk of contamination from unreacted substances that may arise when employing chemical methods

#### **1.2.2.2 Two-step method**

The two-step synthesis method for nanofluids involves the synthesis of the nanomaterial in one step, followed by its dispersion in the required base fluid in another. The synthesis of nanomaterials can be achieved through a variety of processes, encompassing both top-down and bottom-up methodologies. The two-step method is the most common for the preparation of nanofluids due to its ease of production. The advent of a plethora of production methodologies has engendered a substantial array of nanomaterials that can be dispersed in diverse fluids. A comparison of the advantages and disadvantages of the two methods is provided in Table 1-3 (Yılmaz Aydın & Gürü, 2021)

*Table 1-3:Comparison of the advantages and disadvantages of one-step and two-step methods*

| Method | Advantages | Disadvantages |
|---|---|---|
| **Two-step method** | - Well-suited for large-scale<br>- Cost-effective<br>- applicable to oxide-based nanoparticles | - Prone to particle agglomeration<br>- Offers limited precision over particle characteristics<br>- Elevated surface energy may lead to instability |
| **One-step method** | - Ensures high dispersion stability | - Inappropriate for mass production |

| | | |
|---|---|---|
| | - Minimizes particle aggregation<br>- Eliminates the need for post-synthesis storage, drying, and oxidation steps<br>- Provides enhanced control over particle formation | - Associated with higher production costs<br>- Restricted to base fluids with low vapor pressure |

### 1.2.3. **Modeling heat transfer in nanofluids:**

Modeling heat transfer in nanofluids is essential for comprehending their behavior and is a prerequisite for their application. Currently, we outline two primary approaches to heat transfer modeling:

#### **1.2.3.1 Single-phase approach**

Although nanofluids are, by nature, multiphase mixtures composed of a solid nanoparticle phase and a liquid base phase, most numerical and analytical investigations of natural convection consider nanofluids as single-phase (homogeneous) fluids. This assumption is justified by the extremely small size and low concentration of nanoparticles, which are believed to flow at the same velocity as the base fluid. By invoking the local thermal equilibrium hypothesis, the nanoparticle–fluid suspension can be represented as a standard single-phase medium with effective thermophysical properties determined from those of its constituents. Various single-phase modeling approaches have been presented, including the homogeneous model, the Buongiorno model , and the thermal dispersion model.

#### **1.2.3.2 Two-phase approach:**

In contrast to the single-phase approach, the two-phase modeling framework considers the base fluid and nanoparticles as distinct phases that interact dynamically. In practice, nanoparticles are not always uniformly dispersed within the base fluid, since various interfacial and body forces—such as Brownian motion, thermophoresis, and drag—can induce nonuniform particle distributions. Consequently, the two phases may exhibit differences in both velocity and temperature, giving rise to a slip velocity that represents the relative motion between nanoparticles and the surrounding fluid.

Accounting for these interphase effects allows two-phase models to capture more realistic transport mechanisms and provide improved predictive accuracy compared to single-phase formulations, albeit at the cost of increased mathematical and computational complexity. Two main classifications of two-phase models are commonly employed: the Eulerian–Eulerian model, ; and the Eulerian–Lagrangian model.(Bhanvase & Barai, 2021; Sheikholeslami & Ganji, 2016)

Nevertheless, in the present study, the low nanoparticle concentration and nanoscale particle size ensure that interphase slip, and temperature differences are negligible. Therefore, the single-phase

homogeneous model described previously is considered sufficiently accurate and is adopted for the numerical investigation

### 1.2.4. **Thermophysical Properties of Nanofluids**

The incorporation of nanoparticles into a base fluid alters its thermophysical properties, including thermal conductivity, viscosity, and specific heat capacity, which directly influence convective heat transfer. Key factors affecting these properties include nanoparticle concentration, purity level, shape, and size, all of which significantly impact the overall thermal performance of the nanofluid

#### **1.2.4.1 Volume Fraction**

The volume fraction of nanoparticles, denoted by ϕ, is a quantitative measure indicating the proportion of nanoparticle volume relative to the combined volume of the system, encompassing both the fluid and solid components. Mathematically, this can be expressed as follows:

$$\phi = \frac{V_p}{V_t} = \frac{V_p}{V_f + V_p} \tag{1.8}$$

where:

$\phi$ : Volume fraction

$V_p$ : Volume of the nanoparticles

$V_f$ : Volume of the base fluid

$V_t$ : the total volume (nanoparticles + base fluid).

#### **1.2.4.2 The Density:**

To determine the density of a nanofluid, it is assumed that the suspension is fully homogeneous and that the nanoparticles are uniformly dispersed within the base fluid. Under these assumptions, the density of the nanofluid can be expressed as a function of the nanoparticle volume fraction as follows (Einstein, 1906; Xuan & Roetzel, 2000) :

$$\rho_{nf} = \left(\frac{m}{V}\right)_{nf} = \frac{m_f + m_p}{V_f + V_p} = \frac{\rho_f V_f + \rho_p V_p}{V_f + V_p} \tag{1.9}$$

Where :

- $\rho_{nf}$ : The density of the nanofluid
- $\rho_f$ : The density of the base fluid
- $\rho_p$ : The density of the nanoparticles
- $m_f$ : The mass of the base fluid

- $m_p$ the mass of the nanoparticles

From Eqs (1.8) - (1.9), the density of the nanofluid at a given temperature can be derived as(Pak & Cho, 1998):

$$\rho_{nf} = (1-\phi)\rho_f + \phi\rho_p \tag{1.10}$$

#### 1.2.4.3 Specific Heat Capacity

The specific heat capacity of a nanofluid can be calculated using various empirical correlations. A widely adopted formulation was proposed by (Pak & Cho, 1998), who introduced the following equation:

$$(Cp)_{nf} = (1-\phi)(Cp)_f + \phi(Cp)_p \tag{1.11}$$

where $\phi$ is the nanoparticle volume fraction, $(Cp)_{nf}$ is the specific heat capacity of the nanofluid, $(Cp)_f$ is that of the base fluid, and $(Cp)_p$ is that of the nanoparticles. However, as demonstrated by (Zhou et al., 2010) this model provides satisfactory results only at low nanoparticle concentrations, limiting its applicability for broader practical scenarios

To overcome this limitation, (Xuan & Roetzel, 2000) proposed a different approach that explicitly incorporates the nanofluid density into the formulation. This leads to what is often referred to as "Mixture Mode". This model has been extensively employed in nanofluid research due to its effectiveness across a wide range of volume concentrations. It is given by:

$$(\rho Cp)_{nf} = (1-\phi)(\rho Cp)_f + \phi(\rho Cp)_p \tag{1.12}$$

This model assumes thermal equilibrium between the two phases and ensures a more physically consistent representation by considering the density value. A further simplification of this model leads to an alternative formulation based on weight fraction ω, as suggested by (Teng & Hung, 2014)

$$(Cp)_{nf} = (1-\omega)(Cp)_f + \omega(Cp)_p \tag{1.13}$$

#### 1.2.4.4 thermal expansion coefficient

The thermal expansion coefficient $\beta$ represents the rate at which a fluid's density changes with temperature at constant pressure. For a base fluid, it is mathematically defined as(Incropera et al., 1996)

$$\beta_f = -\frac{1}{\rho_f}\left(\frac{\partial \rho_f}{\partial T}\right)_P \tag{1.14}$$

To estimate the thermal expansion coefficient of nanofluids $\beta_{nf}$, Many authors adopt a simplified linear mixing approach that assumes thermal equilibrium and uniform nanoparticle dispersion. The relationship is given by

$$\beta_{nf} = (1-\phi)\beta_f + \phi\beta_p \tag{1.15}$$

where $\phi$ is the nanoparticle volume fraction, $\beta_p$ is the thermal expansion coefficient of the nanoparticles, and $\beta_f$ corresponds to that of the base fluid.

Following the same analytical approach used for determining nanofluid density and specific heat, the thermal expansion coefficient can alternatively be evaluated by expressing the product $(\rho\beta)$ as a linear combination of the properties of the base fluid and the dispersed particles(Khanafer et al., 2003)

$$(\rho\beta)_{nf} = (1-\phi)(\rho\beta)_f + \phi(\rho\beta)_p \tag{1.16}$$

#### 1.2.4.5 Thermal Conductivity of Nanofluids

Numerous theoretical models have been developed to estimate the thermal conductivity of nanofluids, and extensive experimental studies have been conducted to compare the predictions of these models with measured data. These models, which typically assume regular nanoparticle geometries (e.g., spherical shapes), are fundamental for understanding and predicting heat transfer behavior in nanofluids. This section outlines the most commonly used analytical models for estimating nanofluid thermal conductivity

**a) Maxwell Model (1873)**

(Maxwell, 1873) was among the first to analytically investigate the thermal conductivity of mixtures consisting of a fluid matrix with suspended solid spherical particles, while neglecting interactions between the particles. The resulting equation is

$$k_{nf} = k_f \frac{k_s + 2k_f + 2(k_s - k_f)\phi}{k_s + 2k_f - (k_s - k_f)\phi} \tag{1.17}$$

**b) Hamiton–Crosser Model (1962)**

To overcome the limitations of the Maxwell model, which assumes spherical particles, (Hamilton & Crosser, 1962) extended the analysis to account for non-spherical particles. They introduced a shape-dependent empirical factor known as sphericity ($\psi$), which modifies the thermal conductivity relation as follows

$$k_{nf} = k_f \frac{k_s + (n-1)k_f - (n-1)(k_f - k_s)\phi}{k_s + (n-1)k_f + (k_f - k_s)\phi} \tag{1.18}$$

where $n$ is the shape factor is defined as: .For spherical particles $(\psi = 1), n = 3,$ and for cylindrical particles, $n = 6$. Notably, when $\psi = 1$, The Hamilton–Crosser model reduces to Maxwell's expression. These classical models are widely accepted for providing initial approximations, although they do not fully capture complex interfacial phenomena

**c) Yu–Choi Model (2003)**

To address particle–fluid interface effects, (Yu et al., 2003)introduced a more sophisticated model. This formulation incorporates the effect of an interfacial nanolayer between the particle and the fluid, which can alter thermal transport characteristics. However, its application is limited to spherical nanoparticles. The model is expressed as

$$k_{nf} = k_f \frac{k_s + 2k_f + 2\left(k_s - k_f\right)\left(1+\beta\right)^3 \phi}{k_s + 2k_f - \left(k_s - k_f\right)\left(1+\beta\right)^3 \phi} \tag{1.19}$$

where $\beta$ represents the ratio of the nanolayer thickness to the core particle radius, which accounts for the interfacial resistance effects

### 1.2.4.6 Dynamic Viscosity of Nanofluids

Understanding the dynamic viscosity of nanofluids is crucial for optimizing their application in thermal systems, as viscosity directly influences flow characteristics and heat transfer efficiency. Several theoretical and semi-empirical models have been developed to estimate the viscosity of nanofluids, particularly for suspensions containing spherical nanoparticles, with the volume fraction of nanoparticles being the principal variable

**a) Einstein's Model (1905)**

(Einstein, 1905) derived a foundational expression for the dynamic viscosity of dilute suspensions of fine, rigid, spherical particles in a Newtonian base fluid. The model assumes negligible interactions between particles and is valid for volume fractions typically below 1%. The expression is given by

$$\mu_{nf} = \mu_f \left(1 + 2.5\phi\right) \tag{1.20}$$

This formulation has been experimentally validated and is considered reliable for very dilute suspensions. However, it does not account for particle size or interparticle interactions

**b) Brinkman's Model (1952)**

To extend Einstein's model for moderately higher volume concentrations (up to approximately 4%), (Brinkman, 1952) proposed the following relation:

$$\mu_{nf} = \frac{\mu_f}{\left(1-\phi\right)^{2.5}} \tag{1.21}$$

For low volume fractions, this equation reduces to Einstein's model. Nonetheless, like Einstein's, it does not incorporate the effects of particle dimensions or Brownian motion

**c) Batchelor's Model (1977)**

(Batchelor, 1977) introduced a refinement that incorporates hydrodynamic interactions between particles. This leads to a nonlinear dependence of viscosity on the volume fraction, expressed as

$$\mu_{nf} = \mu_f \left(1 + \eta\phi + k_H\phi^2\right) \tag{1.22}$$

where $\eta$ is the intrinsic viscosity and $k_H$ is the Huggins coefficient. For spherical particles, these parameters are typically $\eta = 2.5$ and $k_H = 6.5$. This model is more accurate for suspensions with higher particle concentrations and accounts for two-particle interactions

## 1.3. **Non-Newtonian Fluids**

### 1.3.1. **Basic Rheological Concepts**

Comprehending the fundamental rheological characteristics of fluids is crucial for the examination and simulation of fluid dynamics, especially within intricate frameworks like porous media. This segment elucidates the key principles associated with fluid rheology, encompassing parameters such as viscosity, shear rate, strain rate tensor, and the categorization of fluids based on their rheological properties.

#### **1.3.1.1 Viscosity and Shear Rate**

Viscosity ( $\mu$ ) is a fundamental characteristic that quantifies a fluid's internal resistance to flow. In a simple shear flow context, consider a fluid layer confined between two parallel plates, with the bottom plate fixed. The top plate moves with a constant velocity (Figure 1.4). When the system reaches steady state, the fluid experiences a linear velocity gradient between the plates, leading to the development of shear stress.

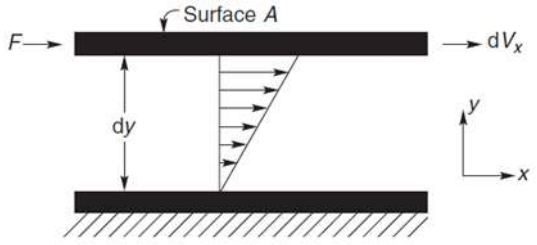



*Figure 1.4 Schematic representation of a unidirectional sheared flow*

The relationship between shear stress ( $\tau$ ) and the velocity gradient ( $du / dy$ ) is defined as:

$$\tau = \mu \frac{du}{dy} = \mu\dot{\gamma} \tag{1.23}$$

Where:

- $\tau$ : $F / A$ The shear stress (Pa)

- $\dot{\gamma}$ : $du / dy$ shear rate ($s^{-1}$)
- $\mu$ : the dynamic viscosity (Pa·s).

In the realm of Newtonian fluids, viscosity is constant and depends only on temperature and pressure, not on the shear rate. Consequently, the flow curve ( $\tau$ vs. $\dot{\gamma}$ ) is a linear relationship (Figure 1.5), with the slope representing the viscosity (Bird et al., 2002)

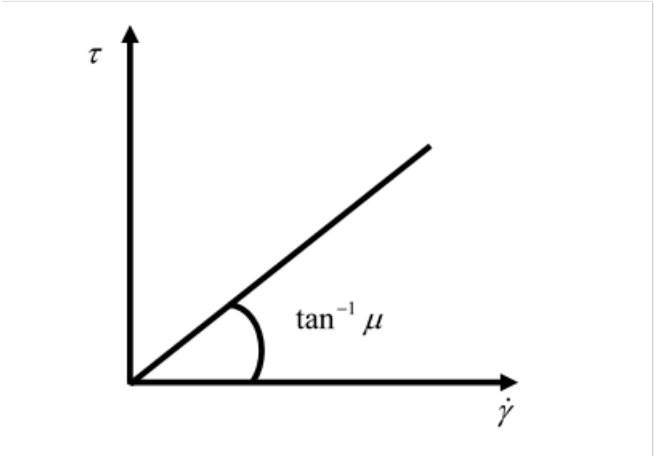



*Figure 1.5 :The shear stress—shear rate curve for incompressible Newtonian fluids*

#### 1.3.1.2 Strain Rate Tensor :

In practical applications requiring intricate geometries or multidirectional flows, shear rate $\dot{\gamma}$ cannot be adequately represented by a singular derivative like $du / dy$ . The strain rate tensor D is employed to depict the deformation of a fluid element in all orientations. The tensor formulation is expressed as:

$$D_{ij} = \frac{1}{2}\left(\frac{\partial u_i}{\partial x_j} + \frac{\partial u_j}{\partial x_i}\right) \qquad (1.24)$$

Where u and x represent velocity and spatial coordinates, respectively. The strain rate tensor's magnitude determines the effective shear rate encountered by a fluid element. In a Newtonian fluid, the Viscous Stress Tensor (τ) is directly proportional to the rate of deformation (D)(White & Majdalani, 2006):

$$\tau = 2\mu D \qquad (1.25)$$

### 1.3.2. Non-Newtonian Fluids

Unlike Newtonian fluids, whose viscosity remains constant under fixed temperature and pressure, non-Newtonian fluids exhibit a viscosity that varies as a function of other parameters such as shear rate, time, the flow apparatus, or the fluid's deformation history. These fluids represent a wide spectrum of rheological behaviors that cannot be described by the linear Newtonian relation Eq(1.23). Instead, they

often follow more complex constitutive laws that link stress and strain rate nonlinearly. The classification of such fluids, for which the flow is not linear, may be divided into three distinct types:

#### 1.3.2.1 Time-Independent Non-Newtonian Fluids

Time-independent non-Newtonian fluids are characterized by a steady-state relation between shear stress and shear rate(Figure 1.6), independent of time. Three common models are:

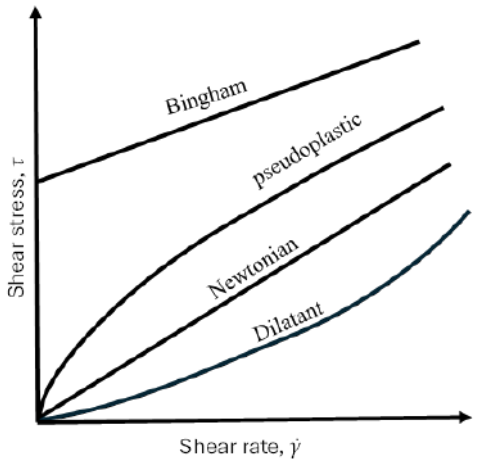



*Figure 1.6: types of non-Newtonian time independent fluids*

**a) Viscoplastic Fluids**

Viscoplastic fluids represent a class of non-Newtonian materials defined by a yield stress $\tau_0$, Under this stress, they behave as solids, whereas surpassing it, they exhibit fluid-like flow (Balmforth et al., 2014). When the shear stress $\tau$ is below $\tau_0$ , the material does not experience continuous deformation and either exhibits elastic behavior or acts as a rigid solid. Material begins to flow only when the stress exceeds this critical threshold, often defined by a shear-dependent viscosity relationship. The Bingham model Eq(1.27) is the most common paradigm for conceiving a viscoplastic fluid.

**b) Pseudoplastic (Shear-Thinning) Fluids**

The pseudoplastic flow phenomenon is characterized by an increase in shear stress that occurs at a decreasing rate as the shear rate increases. In a shear stress–shear rate diagram(Figure 1.6), the flow behavior curve assumes a convex form, characterized by a decrease in tangential slope with increasing shear rate. This behavior demonstrates that viscosity decreases in accordance with an increase in shear rate. This phenomenon is referred to as "shear-thinning" behavior .(Figura & Teixeira, 2007).The commonly employed power-law model(1.24)-(1.25) describes such behavior

**c) Dilatant (Shear-Thickening) Fluids**

Dilatant fluids exhibit an increase in apparent viscosity with increasing shear rate. This is also captured by the power-law model, but with $n>1$. Such behavior is less common and is often seen in concentrated suspensions like starch pastes or wet sand. The mechanism involves dilation—an increase in particle spacing—leading to increased resistance to flow (Barnes et al., 1989)

### 1.3.2.2 Time-Dependent Non-Newtonian Fluids

Time-dependent non-Newtonian fluids exhibit a dynamic viscosity that varies as a function of the applied shear duration even when the shear rate is held constant. This phenomenon is linked to internal structural alterations that transpire during flow. Two typical manifestations of time-dependent behavior (Figure 1.7) are .Thixotropy, marked by a reduction in viscosity over time under consistent shear, and rheopexy, characterized by an increase in viscosity during prolonged shearing(Chhabra & Richardson, 2011)

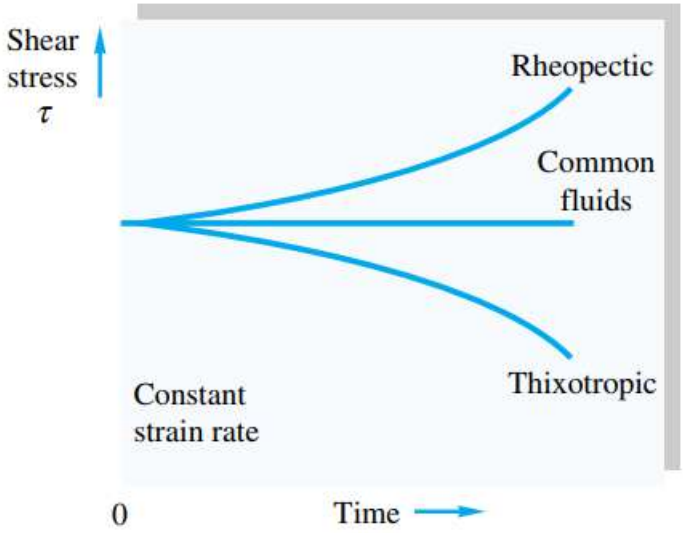



*Figure 1.7:types of non-Newtonian time dependent fluids(Frank, 2011)*

### 1.3.2.3 Viscoelastic Fluids

These fluids exhibit properties of both liquids and solids. When subjected to deformation, they show partial recovery of their original shape, indicating the presence of elastic memory. Their behavior is often modeled using combinations of springs and dashpots in linear viscoelastic models, such as the Maxwell and Kelvin–Voigt models (Barnes, 2000)

## 1.3.3. Constitutive Models for Non-Newtonian Fluids

In fluid mechanics, constitutive models are mathematical expressions that define the relationship between stress ($\tau$) and strain rate ($\dot{\gamma}$) to describe a fluid's deformation. Non-Newtonian fluids exhibit nonlinear behavior in these relations, incorporating elasticity, or structural factors. Choosing a suitable constitutive model is crucial for precise flow prediction .The following are the common models for time-independent non-Newtonian fluids.

#### 1.3.3.1 Power-Law (Ostwald–de Waele) Model

The power-law model stands out as a fundamental and frequently employed framework for characterizing the rheological behavior of shear-thinning and shear-thickening fluids. The equation for this model is given as:

$$\tau = k\dot{\gamma}^{n} \tag{1.26}$$

where $k$ is the consistency index and $0 < n < 1$ is the flow behavior index. The apparent viscosity is:

$$\eta = \tau / \dot{\gamma} = k\dot{\gamma}^{n-1} \tag{1.27}$$

While the power-law model is simple and useful for many practical applications, it fails to capture the Newtonian plateau at low and high shear rates and cannot represent yield stress behavior. Hence, more advanced models are often required (Chhabra & Richardson, 2011)

#### 1.3.3.2 Sisko Model

The Sisko model (Sisko, 1958) is an extension of the power-law model that includes a high shear-rate viscosity asymptote, enabling it to accurately describe fluids that exhibit shear-thinning behavior at intermediate shear rates while approaching Newtonian behavior at high shear rate(Barnes et al., 1989)

$$\tau = -\gamma\left(\mu_{\infty} + K_{s}\left|\tau\right|^{z-1}\right) \tag{1.28}$$

Where

- $\mu_{\infty}$ : infinite-shear-rate viscosity
- $K_{s}$ consistency index
- $z$ : flow behavior index

it simplifies to the conventional power-law model when the infinite-shear-rate viscosity ($\mu_{\infty}$)approaches zero .Furthermore,

#### 1.3.3.3 The Bingham plastic model

Bingham plastics exhibit a yield stress $\tau_Y$, below which no flow occurs. Once this threshold is exceeded, the fluid behaves in a linear (Newtonian) fashion. The constitutive equation is given by

$$\left\{\begin{array}{ll} \tau = \tau_{Y} + \mu_{P}\dot{\gamma} \;\; ; & \left|\tau\right| > \tau_{Y} \\ \dot{\gamma} = 0 \quad , & \left|\tau\right| \le \tau_{Y} \end{array}\right\} \tag{1.29}$$

where $\mu_{p}$ is the plastic viscosity. Typical examples include toothpaste, slurries, drilling muds, and certain food products. The yield stress represents the rigidity of a three-dimensional internal structure, which must be broken down before flow initiates .

#### 1.3.3.4 Herschel–Bulkley Model

The (Herschel & Bulkley, 1926) model combines features of the Bingham plastic and power-law models:

$$\begin{Bmatrix} \tau = \tau_Y + K\dot{\gamma}^n \ , |\tau| > \tau_Y \\ \dot{\gamma} = 0 \quad , \ |\tau| \le \tau_Y \end{Bmatrix} \tag{1.30}$$

This model can represent both yield stress and shear-thinning or shear-thickening behavior. It is widely used for complex fluids such as drilling muds, food emulsions, and polymer gels

#### 1.3.3.5 Carreau model

The Carreau model (Carreau, 1968) is widely employed to describe the rheological behavior that showing significant deviate from the idealized power-law model at both very low and high shear rate viscosities(Chhabra & Richardson, 2011). Unlike previous models, the Carreau model incorporates limiting viscosities, i.e. the zero and infinite-shear rate ,allowing for a more accurate representation over a wide range of shear rates. The general form of this model is:

$$\mu(\dot{\gamma}) = \mu_\infty + (\mu_0 - \mu_\infty)\left[1 + (\lambda\dot{\gamma})^2\right]^{\frac{n-1}{2}} \tag{1.31}$$

where:

- $\mu(\dot{\gamma})$ the apparent viscosity
- $\mu_0$ and $\mu_\infty$ are the zero and infinite shear rate viscosities, respectively,
- $\lambda$ is a time constant (relaxation time).
- $n$ is the flow behavior index (with $n < 1$ for shear-thinning fluids),
- $\dot{\gamma}$ is the shear rate.

#### 1.3.3.6 Cross Model

The Cross model is due to (Cross, 1965) is an empirical formulation that also describes a smooth transition between the two viscosity limits:

$$\mu_{eff} = \mu_\infty + \frac{\mu_0 - \mu_\infty}{1 + k(\dot{\gamma})^n} \tag{1.32}$$

#### 1.3.3.7 Carreau–Yasuda Model

This model effectively describes how viscosity varies smoothly with shear rate. As an extension of the classical Carreau model, the Carreau–Yasuda formulation introduces additional flexibility by remaining continuous across the entire shear-rate spectrum ($\dot{\gamma} \geq 0$) (Bird et al., 1987). The model is mathematically formulated as:

$$\mu(\dot{\gamma}) = \mu_\infty + (\mu_0 - \mu_\infty)\left[1 + \left(\lambda\dot{\gamma}\right)^a\right]^{\frac{n-1}{a}} \tag{1.33}$$

Thereby providing a more accurate fit to experimental data. Unlike the simpler models, the Carreau–Yasuda model incorporates five parameters:

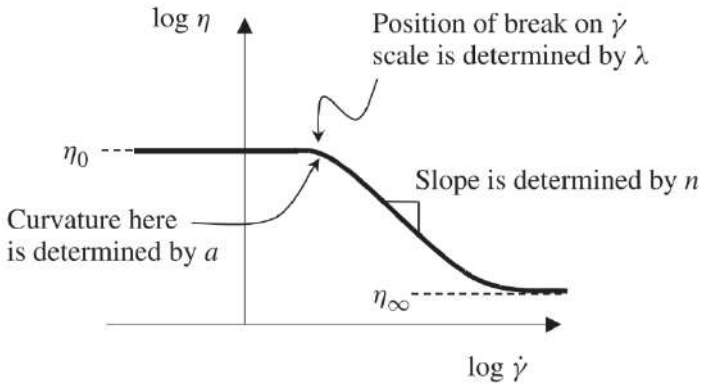



*Figure 1.8: Viscosity behaviour as modelled by the Carreau–Yasuda model(Morrison, 2001)*

- $\mu_0$ ($\eta_0$) and $\mu_\infty$ ($\eta_\infty$) represent the viscosities at zero and infinite shear rates, respectively
- $\lambda$ is the relaxation time parameter that governs the onset of the shear-thinning regime.
- $a$ controls the sharpness of the transition between the Newtonian plateau and the power-law region.
- $n$ defines the slope of the shear-thinning region.

This structure enables the model to fit a wide range of experimentally observed $\mu(\dot{\gamma})$ curves with high fidelity. While analytical solutions using the Carreau–Yasuda model are often challenging due to its complexity, the model is well-suited for implementation in numerical simulations. (Morrison, 2001)

## 1.4. **magnetohydrodynamics (MHD)**

### 1.4.1. **Definition**

Magnetohydrodynamics (MHD) is an interdisciplinary field that integrates the principles of fluid dynamics and electromagnetism to study the behavior of electrically conducting fluids under the influence of magnetic fields. Such fluids include liquid metals, electrolytes, and various types of plasmas. MHD examines the coupled interactions between fluid motion and electromagnetic forces, wherein the magnetic field can alter the fluid flow, and conversely, the movement of the fluid can induce or modify the magnetic field.

The theoretical foundation of MHD was established by the Swedish physicist **(**Alfvén, 1942**),** who demonstrated the existence of magnetohydrodynamic waves—now known as Alfvén waves. His pioneering contributions significantly advanced the understanding of plasma behavior in both laboratory and astrophysical environments, earning him the Nobel Prize in Physics in 1970..

The interaction between a magnetic field, B, and a velocity field, v, is influenced by Faraday's and Ampère's laws, as well as the Lorentz force acting on a current-carrying entity. This coupling can be divided into three parts.(Davidson, 2017)

- The relative motion of a fluid v with electrical conductivity σ in a magnetic field B (Figure 1.9) creates an electromotive force (EMF) within the fluid, described by the emergence of a current density in the fluid of order σ(v × B)
- These currents that are induced must, following Ampère's rule, give birth to a second, induced magnetic field. This adds to the first magnetic field, and the change is typically such that the fluid seemingly 'drag' the magnetic field lines alongside it
- The two types of magnetic field (imposed along with induced) interacts with the induced current density, J, thereby giving rise to a Lorentz force (per unit volume) of $\vec{J} \times \vec{B}$. This force acts upon the conductor and typically exerts a restraining effect on the relative motion between the magnetic field and the fluid.

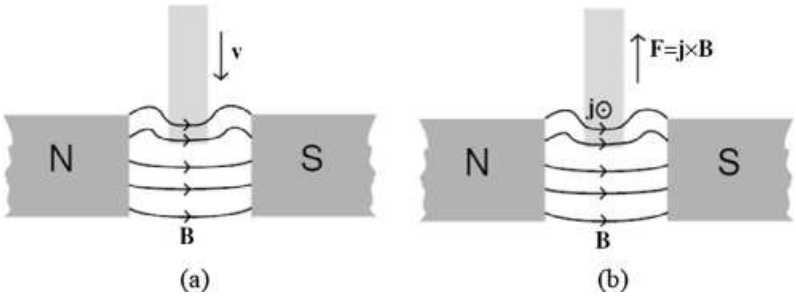



*Figure 1.9: Interaction of a magnetic field and a moving conductor*

### 1.4.2. **The MHD Equations and Essential Dimensionless Parameters**

#### **1.4.2.1 Maxwell's Equations:**

To characterize an electromagnetic field, we use various variables:

- $\vec{\boldsymbol{B}}$: Formally referred to as magnetic flux density, we shall designate it as the magnetic field.
- $\vec{\boldsymbol{H}}$**:** the magnetic field strength
- $\vec{\boldsymbol{E}}$: the electric field
- $\vec{\boldsymbol{D}}$: the electric displacement
- $\vec{\boldsymbol{j}}$: the electric current density

- $\overrightarrow{\boldsymbol{\rho_c}}$: the electric charge density

These are interconnected by Maxwell's equations, which dictate the dynamics of electric and magnetic fields:

$$\left.\begin{aligned} \vec{\nabla}.\vec{D} &= \rho_c, \\ \vec{\nabla}\times\vec{\mathrm{E}} &= -\frac{\partial\vec{B}}{\partial t}, \\ \vec{\nabla}.\vec{B} &= 0, \\ \vec{\nabla}\times\vec{H} &= \vec{j}+\frac{\partial\vec{D}}{\partial t} \end{aligned}\right\} \tag{1.34}$$

In an isotropic medium, which we shall presume.

$$\vec{D} = \varepsilon_e\vec{E}\ ,\vec{B} = \mu_e\vec{E} \tag{1.35}$$

where $\mu_e$ is the medium's magnetic permeability and $\varepsilon_e$ is the permittivity, also known as the dielectric constant.

#### 1.4.2.2 The Lorentz force law :

The Lorentz force law underpins the MHD model. A charged particle moving in an electromagnetic field experiences a force, as described by the Lorentz force equation . This force can be characterized as:

$$\vec{F} = q\left(\vec{u}\times\vec{B}\right) \tag{1.36}$$

where $\vec{F}$ represents the force exerted on a charged particle, $q$ denotes the particle's charge $\vec{u}$ indicates the particle's velocity, and $\vec{B}$ signifies the magnetic induction

#### 1.4.2.3 Ohm's Law

Ohm's law states that the electric current density within an electrically conducting medium is directly proportional to the applied electric field. In addition to the electric field $\vec{E}$ acting on a stationary fluid, a fluid in motion with velocity $\vec{u}$ within a magnetic field $\vec{B}$ experiences an extra electric field represented by $\vec{u}\times\vec{B}$. Ohm's law subsequently provides

$$\vec{J} = \sigma\left(\vec{E}+\vec{u}\times\vec{B}\right) \tag{1.37}$$

#### 1.4.2.4 Navier–Stokes and the induction equation

Equations (1.32) to (1.35) collectively yield the induction equation:

$$\frac{\partial B}{\partial t} = \nabla\times\left(u\times B\right)+\lambda\nabla^2 B, \qquad \lambda = \left(\mu\sigma\right)^{-1} \tag{1.38}$$

or, equivalently, considering that B and u are both solenoidal,

$$\frac{DB}{Dt} = (B.\nabla)u + \lambda\nabla^2 B \tag{1.39}$$

Otherwise, Newton's second law yields the Navier–Stokes equation—the governing equation for fluid flow—which, when the Lorentz force is included, has the following form

$$\rho\frac{Du}{Dt} = -\nabla p + \rho g + \rho\nu\nabla^2 u + J \times B \tag{1.40}$$

where $\nu$ is the kinematic viscosity, $p$ is the pressure, $u$ is the fluid velocity, and $\rho$ is the fluid density.

#### 1.4.2.5 Some dimensionless groups in MHD.

There are a number of dimensionless groups which commonly arise in the MHD literature, and we shall cover some of these in table1-4 (Sheikholeslami & Ganji, 2016)

*Table 1-4:List of Nondimensional Parameters*

| Nondimensional Parameter | Definition |
|---|---|
| Reynolds number | $\mathrm{Re} = \frac{\text{Inertia forces}}{\text{Viscous forces}} = \frac{U_0 L}{\nu}$ |
| Magnetic Reynolds number | $\mathrm{Re}_m = \frac{\text{Convection of B}}{\text{Diffusion of B}} = \frac{\text{Induced field}}{\text{Applied field}} = \frac{U_0 L}{\nu_m} = \mu_0\sigma U_0 L$ |
| Hartmann number | $\mathrm{Ha} = \left(\frac{\text{Electromagnetic forces}}{\text{Viscous forces}}\right)^{1/2} = B_0 L\sqrt{\frac{\sigma}{\nu\rho}}$ |
| Alfvén number | $\mathrm{Al} = \frac{\text{Magnetic field energy}}{\text{Kinetic energy}} = \frac{N}{\mathrm{Re}_m} = \frac{B_0^2}{\mu_0\rho U_0^2}$ |
| Stuart number (interaction parameter) | $N \equiv \mathrm{St} = \frac{\text{Electromagnetic forces}}{\text{Inertia forces}} = \frac{\mathrm{Ha}^2}{\mathrm{Re}} = \frac{\sigma B_0^2 L}{\rho U_0}$ |
| Batchelor number (magnetic Prandtl number) | $\mathrm{Bt} \equiv \mathrm{Pr}_m = \frac{\mathrm{Re}_m}{\mathrm{Re}} = \mu_0\sigma\nu = \frac{\nu}{\nu_m}$ |

Where :

- $U_0$: Characteristic velocity
- $L$: Characteristic length
- $\nu$: Kinematic viscosity
- $\nu_m$: Magnetic viscosity (or magnetic diffusivity)
- $\mu_0$: Permeability of free space
- $\sigma$: Electrical conductivity
- $B_0$: Applied magnetic field strength
- $\rho$: Density

## 1.5. Current State of Research

The use of nanofluids to enhance convective heat transfer in porous media has attracted substantial attention in both academic research and industrial practice in recent decades. This is mostly due to the

many engineering applications that this technique offers. As a result of their improved thermal characteristics, nanofluids are rapidly being used in a variety of applications, including thermal energy storage, electronic cooling, geothermal energy, and solar thermal collectors. Within the body of published work, this subject is discussed in a wide range of comprehensive reviews and resources. Particularly noteworthy are the chapters 11 and 12 of Heat Transfer Enhancement with Nanofluids (Bianco et al., 2015), and Chapter 4 of Convective Heat Transfer in Porous Media(Mahmoudi, 2019) .section 4 of the Handbook of Porous Media (Vafai, 2015)

The term “nanofluid” was first introduced by (Choi & Eastman, 1995) to describe the suspension of solid nanoparticles within a base fluid. In essence, nanofluids are fluids in which nanoparticles, typically less than 100 nm in diameter, are dispersed to enhance thermal conductivity and heat transfer capabilities. Since their introduction, extensive research has focused on nanofluid behavior in enclosures. demonstrating notable improvements in heat transfer performance under various conditions.(Khanafer & Vafai, 2019), conducted a detailed review of nanofluid thermophysical properties and their integration with porous media in applications such as solar energy systems, building insulation, and biomedical devices. Despite highlighting the enhanced heat transfer potential of nanofluids, they also emphasized discrepancies between theoretical predictions and experimental observations, indicating the need for continued investigation. Several numerical studies have addressed natural convection of nanofluids in porous or partially porous cavities (Boualit et al., 2017) examined free convection of a Cu–water nanofluid in a square cavity using a thermal dispersion model and reported that increasing the nanoparticle volume fraction significantly enhances heat transfer, particularly at high Rayleigh numbers. They also found that the influence of nanoparticle size depends on the dispersion intensity. (Faraz, Nisar, et al., 2023) analyzed natural convection of Cu–water nanofluid in a hexagonal cavity with a central square opening using the Galerkin finite element method. The study demonstrated that both the Rayleigh number and the nanoparticle volume fraction exert a positive influence on thermal performance, leading to an increase in the average Nusselt number. Additionally, the spatial distribution of heat transfer was found to be strongly dependent on the location of the heated wall. Using the LTNE model (Kumar et al., 2021) studied natural convection of silver nanofluid in a porous cavity and demonstrated that higher Rayleigh numbers promote stronger vortex development and improve heat transfer. Similarly, (Benygzer et al., 2023) applied Buongiorno’s model to analyze natural convection in a square cavity partially filled with porous medium, showing that increasing the Rayleigh number and reducing the porous-layer thickness enhances convective heat transfer. (Manaa et al., 2024) investigated thermo-solutal natural convection of a Cu–water micropolar nanofluid in a cubic porous enclosure using the Brinkman–Darcy model and the finite volume method. Their results indicated that the micropolar effects reduce heat and mass transfer, whereas the addition of nanoparticles enhances convective

transport, with the Nusselt number increasing by 57.57% as the Darcy number rises from $10^{-3}$ to $10^{-1}$. (Zhang et al., 2021), employed the Galerkin method to analyze Cu-based nanofluid convection in an annular porous region, demonstrating that smaller nanoparticle sizes and higher porosity lead to more efficient heat transfer. More recently,(Faisal et al., 2025)studied thermal convection enhancement in engine oil-based $MoS_4$ nanofluid within a porous square cavity using a Galerkin finite element scheme. Their findings revealed that increasing both the nanoparticle concentration and Rayleigh number significantly improves convective heat transfer, while larger Darcy numbers promote greater fluid mobility.. Other studies have focused on the influence of porous media properties and inertial effects, (Alilat, Alliche, Rebhi, & Borjini, 2020) used a Cu–water nanofluid to analyze natural convection in a Dupuit–Darcy porous medium and concluded that high inertial forces lead to conduction-dominated regimes, whereas increased porosity or nanoparticle concentration tends to reduce heat transfer.(Venkatadri et al., 2023) working with the same nanofluid in a trapezoidal porous cavity, found that heat transfer increases with Rayleigh number but decreases with higher nanoparticle volume fractions, indicating that nanoparticle loading does not always guarantee performance enhancement. Additionally, (Muthtamilselvan & Sureshkumar, 2017) demonstrated that the influence of nanoparticles on heat transfer depends strongly on the enclosure aspect ratio and flow regime, where enhancement may occur under some conditions but may be suppressed in others..

Recent developments in nanofluid research have increasingly focused on the use of multi-component nanoparticle suspensions, referred to as hybrid nanofluids. The central motivation behind employing hybrid nanofluids is to achieve a synergistic enhancement of thermophysical properties—particularly thermal conductivity—beyond what can be attained using conventional base fluids or single-nanoparticle nanofluids alone. For instance,. (Nabwey et al., 2025). statistically examined the MHD natural convection of an $Al_2O_3$–Cu/water hybrid nanofluid within a porous square cavity containing a cross-shaped barrier and heated corners. Based on Darcy's law and the LTNE formulation, the governing equations were solved using the finite difference method. Their results showed that increasing the Hartmann number or applying negative heat sources ($Q = -15$) suppresses fluid motion and promotes conduction-dominated heat transfer, while increasing the Rayleigh number or employing positive heat sources ($Q = 5$) enhances convective heat transport. Furthermore, increasing the nanoparticle volume fraction improved heat transfer, with Cu-based hybrid nanoparticles outperforming $Al_2O_3$-based ones..in another investigation, (Mirza et al., 2025) proposed an intelligent computational framework for analyzing the two-phase motion of a dusty trihybrid nanofluid (THNF) in a Darcy–Forchheimer porous medium using Levenberg–Marquardt neural networks. Their formulation incorporated Marangoni convection and Cattaneo–Christov heat flux effects. The results demonstrated that higher Marangoni numbers increase velocity, while activation energy significantly influences flow structure and thermal

distribution. Similarly,. (Bani-Fwaz et al., 2025) numerically explored $Fe_3O_4$/$MnZnFe_3O_4$–ethylene glycol hybrid nanofluid behavior over a tilted stretching surface under Cattaneo–Christov heat conduction. Using a shooting method with a Runge–Kutta solver, they reported that nanoparticle incorporation increases thermal conductivity, and optimal radiation and heating parameters enhance heat transfer.(Rajenderan & Prasad, 2024) examined MHD thermo-convection of an Ag–GO hybrid nanofluid in a square enclosure with internal heat generation. Their findings showed that increasing the Hartmann number suppresses convection due to magnetic damping, while increasing the Richardson and Reynolds numbers enhances heat transfer.(Mehryan et al., 2019) explores the impact of Cu–$Al_2O_3$/water hybrid nanofluid in conjunction with $Al_2O_3$/water nanofluid on heat transmission and fluid flow within a square cavity including an oscillating hot cylinder. The Galerkin finite element method is used to solve the governing equations on a moving grid. The results reveal that nanoparticles increase the average Nusselt number and heat trensfer at low Rayleigh numbers. However, for large Rayleigh numbers, only the $Al_2O_3$/water nanofluid exhibits an increase in heat transfer, whereas the (Cu–$Al_2O_3$)/water hybrid nanofluid reduce the values of Nu. (Revnic et al., 2024)provide a numerical analysis of natural convection within a porous square cavity filled with a ternary hybrid nanofluid composed of titania ($TiO_2$), copper (Cu), and alumina ($Al_2O_3$). Numerically solving the governing equations employing a Galerkin-based finite element model. Research indicates that, compared to classical fluids, nanofluids, and hybrid nanofluids, ternary hybrid nanofluids have superior heat transport propertie .In addition to hybrid and ferrofluid studies, micropolar nanofluid systems have also been explored. For example,. (Mishra et al., 2025) analyzed the micropolar flow of AA7072 alloy-based nanofluids in a two-dimensional channel with expanding and contracting walls. By solving a modified Navier–Stokes model with a shooting method and Runge–Kutta scheme, they found that increasing the Reynolds number enhanced flow velocity, whereas increasing microrotation reduced it. Thermal radiation effects were also shown to play a significant role, particularly near the lower wall.

Research on non-Newtonian nanofluid flow in porous media has grown substantially due to the industrial relevance of fluids exhibiting complex rheology. (Barnoon & Toghraie, 2018) used the finite volume method to study laminar flow and heat transfer of a pseudoplastic ($Al_2O_3$ + CMC) nanofluid in a porous medium, showing that thickening the porous layer greatly increased the convection rate, despite the Reynolds number having limited effect.(Khechiba et al., 2017) examined convection in a porous enclosure using the Carreau–Yasuda and Darcy–Brinkman–Forchheimer formulations and found that stronger shear-thinning behavior enhances convective performance.. Similar results were reported by (Alloui & Vasseur, 2015) who demonstrated that lower power-law indices strengthen circulation and heat transfer, and that the Carreau–Yasuda model provides more accurate predictions than the power-law model. Furthermore,(Javaherdeh et al., 2021) found that non-Newtonian nanofluids exhibit a 12.8%

improvement in heat transfer compared to Newtonian nanofluids in porous channels modeled using a modified Brinkman–Forchheimer approach..

The influence of magnetic fields introduces an additional dimension to heat transfer control. (Mahmood et al., 2022)studied entropy generation and ferrofluid flow in a wavy porous cavity under magnetic fields, demonstrating that increasing the Hartmann number reduces thermal and viscous irreversibility while increasing the Bejan number. It's noteworthy to observe that as surface waviness expanded, the average Nusselt number declined. Similarly, (Mirzaei et al., 2024) investigated partial magnetic field impacts on free convection in a porous wavy cavity Use the enlarged Brinkman-Forchheimer-Darcy model to analyze fluid flow. and found that magnetic fields suppress fluid motion by compressing the primary vortex, reducing heat transfer efficiency, while increasing the Rayleigh number helps restore convective strength.. (Khan et al., 2022) numerically examined natural convection in a square cavity containing a central solid obstruction subjected to an inclined magnetic field, considering both uniform and non-uniform heating on the lower wall while maintaining an adiabatic moving upper boundary. Using the Boussinesq approximation and the finite element method, they demonstrated that increasing the Hartmann number reduces kinetic energy due to the Lorentz force, whereas increasing the Reynolds number enhances heat transfer, as reflected by higher Nusselt numbers . In another contribution,(Abderrahmane et al., 2022) analyzed free convection of a non-Newtonian nanofluid in a tilted half-annulus porous enclosure using FEM. Their results showed that larger Hartmann numbers weaken convective heat transfer due to magnetic damping, while higher Rayleigh numbers strengthen convective circulation. Moreover, an increase in the power-law index adversely affected local Nusselt numbers and overall heat transfer efficiency. (Faraz, Majeed, et al., 2023) investigated the influence of gap spacing and flow behavior index on hydrodynamic forces acting on cylinders placed in a power-law fluid within a confined channel using the Galerkin finite element method. They reported that both lift and drag forces increase with the power-law index. Additionally, (Adnan et al., 2024) employed the Koo–Kleinstreuer–Li model to analyze hydrocarbon-based Cu–kerosene nanofluid flow in non-Darcy porous media, concluding that higher porous media permeability adversely affects fluid motion and heat transfer. Furthermore, (Reddy et al., 2023) observed reduced heat transfer when studying MHD buoyant convection in an inclined porous annulus using the Brinkman–Forchheimer extended model, with higher Hartmann numbers leading to slower flow and diminished convective effectiveness. (Vahedi et al., 2019) studied the effects of heater geometry, magnetic fields , and sidewall thickness on the augmentation of natural convection in a square enclosure containing Al2O3-water nanofluid using the finite volume technique. The research indicated that as the intensity of the heat source grew, so did the Nusselt number. However, the inclusion of a magnetic field lowered Nusselt numbers because it inhibited fluid circulation, particularly at higher Hartmann numbers.

Moreover,(Alilat, Alliche, Rebhi, & Chamkha, 2020) used the Dupuit–Darcy model to investigate SWCNT–water nanofluid convection in an inclined porous domain under magnetic influence, showing that increasing nanoparticle concentration improves convection up to a viscosity threshold, while higher Hartmann numbers and inertial effects eventually shift heat transfer toward conduction. (Rasool et al., 2020) also emphasized the role of Lorentz forces by examining nanofluid flow between two parallel plates under a compressed Darcy–Forchheimer–MHD formulation, demonstrating that increased magnetic and Forchheimer parameters reduce velocity. The effects of MHD and quadratic natural convection on the porous square cavity containing Cu-water nanofluid were further studied by (Jino & Kumar, 2021) investigated quadratic natural convection of Cu–water nanofluid in a porous cavity and reported suppressed convection and reduced heat transfer under magnetic fields—consistent with the finding of . (Zafar et al., 2023) when MHD was applied to $TiO_2$ nanoparticles distributed in engine oil. (Geridonmez & Oztop, 2019) used the Brinkman–Forchheimer-extended model to study the effects of a partial magnetic field on natural convection in a square porous cavity. Their findings demonstrated that fluctuations in the intensity of the flow's center vortex caused convective heat transfer to decrease as the magnetic field length increased. (Rebhi et al., 2021) confirmed these findings by utilizing the Dupuit-Darcy model to investigate the effects of a slanted magnetic field on double-diffusive convection in a tilted porous enclosure. The results demonstrate that convective flow is obstructed by increasing magnetic and inertial forces, resulting in a transition from convective to conductive heat transfer. A separate investigation , (Kareem & Abdulhadi, 2019) analyzed the synergistic impacts of porous media ,magnetic f, and nanoparticles on thermal transfer and fluid dynamics. Research indicated that whereas nanoparticles augment heat transfer, magnetic fields and porous media diminish fluid velocity .(Vigneshwari et al., 2025) employed the Darcy–Forchheimer method to explore the impact of magnetohydrodynamic (MHD) flow on the heat transfer properties of Jeffrey fluids in a square porous cavity. The Galerkin finite element method (GFEM) is utilized to solve the governing equations. Important results reveal that an increase in the Hartmann number causes the average Nusselt number to decrease at higher Rayleigh numbers ($Ra = 10^6$). On the other hand, despite variations in the Hartmann number, the Nusselt number stays comparably stable for lower Rayleigh numbers ($Ra = 10^3$). (Giwa et al., 2021) provided a comprehensive computational and experimental review showing that magnetic fields strongly modify convection patterns in nanofluid-filled cavities, with implications for thermal management in renewable energy, electronics, and cooling technologies.

In contrast to the extensive literature on Newtonian and power-law nanofluids, studies specifically examining the influence of magnetic fields on heat transfer in Carreau–Yasuda fluids remain relatively limited. Some recent works have addressed this topic in fluid enclosures, while others considered porous media through the Darcy-type formulation. For example,. (Qayyum et al., 2023) investigated the

transient behavior of Carreau–Yasuda nanofluid under a variable magnetic field, taking into account chemical reactions and viscous dissipation effects.. In another sudy, (Alqahtani et al., 2023) .examined heat transfer characteristics of a hybrid Carreau–Yasuda nanofluid exposed to a magnetic field in a fluid-filled cavity. Similarly, (Bilal et al., 2023) explored magnetohydrodynamic effects on thermal transport in a tri-hybrid Carreau–Yasuda nanofluid system. A study by (Salahuddin et al., 2024) further analyzed heat transfer and flow patterns of a Carreau–Yasuda nanofluid over a sinusoidal surface within a fluid medium. With respect to porous media (Akram et al., 2023) assessed mixed convection of a Carreau–Yasuda nanofluid saturated within a porous region under magnetic field influence.. (Abbas et al., 2024) extended this investigation to an enclosure with ciliated walls saturated by a Carreau–Yasuda fluid, highlighting the role of wall microstructure in modifying heat transfer . Additionally, (Iqbal et al., 2025)explored the enhancement of thermal performance using a magnetically influenced Carreau–Yasuda nanofluid for solar aircraft thermal regulation applications. A related study by (Djamel et al., 2023) numerically evaluated heat transfer enhancement in a porous medium saturated with Carreau–Yasuda nanofluid using the Dupuit–Darcy model. However, the influence of magnetic fields was not considered in their analysis, leaving an important aspect of magneto-convective transport unaddressed.

A review of the existing literature reveals that no prior study has simultaneously examined the influence of a magnetic field on free convection of shear-thinning nanofluids within a porous square cavity using both the Dupuit–Darcy model to describe flow through porous media and the Carreau–Yasuda model to represent the effective non-Newtonian viscosity. In response to this gap, the present work investigates the effects of several key parameters on natural convection within the enclosure, including the magnetic field strength, inertial effects,Carreau–Yasuda rheological parameters, nanoparticle volume fraction, and the inclination angle of the cavity. The configuration considered is subjected to a temperature difference imposed across the vertical walls, while the horizontal boundaries are maintained as adiabatic, enabling detailed analysis of heat and fluid transport in the system.

# CHAPTER 2

# PHYSICAL MODEL & MATHEMATICAL FORMULATION

# 2. CHAPTER II :PHYSICAL MODELING AND GOVERNING MATHEMATICAL FORMULATION

## 2.1. Problem description

This section presents a study on natural convection in a porous media saturated with a non-Newtonian nanofluid. The cavity is subjected to an external magnetic field, considering the inertial effects on fluid dynamics and thermal transport. The study examines the natural convection characteristics of two categories of nanofluids: conventional nanofluids, specifically (SWCNT-water) and ($Al_2O_3$-water), and hybrid nanofluids, namely ($Al_2O_3$+Cu-Water.)

The physical configuration of the problem is illustrated in Figure 2.1, with x and y representing the Cartesian coordinates. The dimensions of the cavity are specified by L, for the length, and H, for the height.

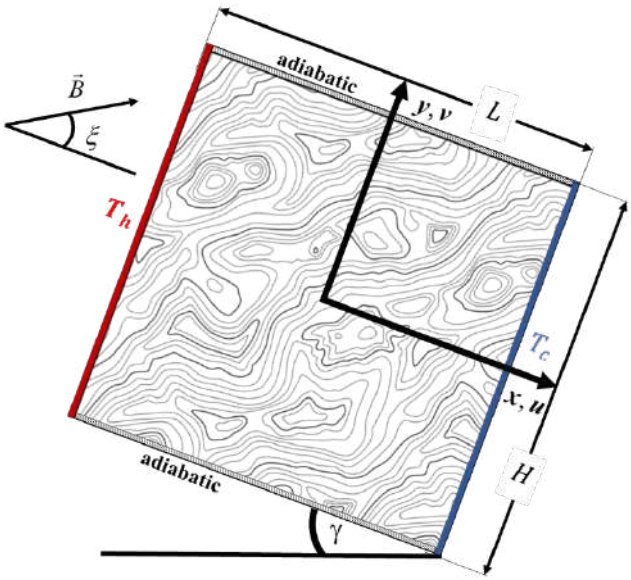



*Figure 2.1: Schematic representation of the problem*

The left vertical wall is maintained at a uniform hot temperature $T_h$, whereas the right vertical wall is kept at a constant cold temperature $T_c$ . The top and bottom horizontal walls are assumed to be adiabatic, implying no heat flux across them. The cavity is inclined at an angle γ with respect to the horizontal plane.

## 2.2. Model Simplifications and Assumptions

To simplify the mathematical modeling and reduce computational complexity, several standard assumptions are adopted (Rashad et al., 2017)

- The cavity is assumed to be subjected to a uniform and constant gravitational field.
- The fluid flow is laminar and incompressible

- The porous medium is treated as isotropic, homogeneous, and permeable.
- No chemical reactions or internal sources of heat or mass are present within the domain, and the effects of thermal radiation are neglected.
- The work done by pressure forces is assumed negligible .
- The suspended nanoparticles are assumed to be spherical.
- Thermal equilibrium between the base fluid and nanoparticles is assumed, allowing the use of a single-phase nanofluid model.
- The thermal effects due to viscous dissipation and Joule heating are neglected
- The thermophysical properties of the nanofluid are constant, except for its density (temperature-dependent in the buoyancy term using Boussinesq approximation) and viscosity (shear-rate dependent).
- The nanofluid is assumed to exhibit non-Newtonian behavior, and its apparent viscosity is modelled using Carreau–Yasuda model.
- The influence of the induced magnetic field is neglected ($Rm \ll 1$).

## 2.3. **Mathematical formulation**

Based on the assumptions outlined previously, the governing equations of the system include the continuity equation, the momentum equation, and the energy equation. The movement of the nanofluid in the porous media is articulated by the Dupuit–Darcy model, wherein the porous matrix is assumed to be completely saturated with a non-Newtonian nanofluid characterized by the Carreau–Yasuda rheology. In addition, the formulation accounts for the effects of a magnetic field, which introduces a Lorentz force acting against fluid motion. The nonlinear inertial term is incorporated into the momentum equation to represent deviations from purely viscous Darcy flow:. Ahmed and Mahdy (2016); (Alilat, Alliche, Rebhi, & Borjini, 2020; Alilat, Alliche, Rebhi, & Chamkha, 2020; Cheng, 2006; Djamel et al., 2023; Hossain & Rees, 1997; Kumari et al., 2019; Mahdy, 2009; Poulikakos & Bejan, 1985; Rebhi et al., 2021; Rebhi et al., 2020 ;Rebhi et al., 2014; Rebhi et al., 2016; Rees, 1996; Rees & Pop, 1995; Riley & Rees, 1985; Rosca et al., 2012; Saeid & Pop, 2005(:

### 2.3.1. **Continuity equation**

The conservation of mass for an incompressible nanofluid is expressed as::

$$\nabla . V = 0 \tag{2.1}$$

### 2.3.2. **Momentum equation**

The local momentum conservation for flow in a porous medium is described using the Dupuit–Darcy model, incorporating magnetic and inertial effects::

$$V\times\left(1+\frac{\tilde{K}}{\mu_a}\rho_{nf}\left|\vec{V}\right|\right)=-\frac{K}{\mu_{nf}}\left(\nabla p-\rho_{nf}g-I\times B\right) \tag{2.2}$$

### 2.3.3. **Energy equation**

Applying the first law of thermodynamics and neglecting viscous dissipation yields the energy transport equation:

$$\frac{\partial T}{\partial \tau}+\left(V.\nabla\right)T=\alpha_{mnf}\nabla^2 T \tag{2.3}$$

In these equations, $V\left(u,v\right)$ is the velocity vector, $B\left(B_x,B_y\right)$ denotes the magnetic induction vector, $I$ represents the electric current. $p$ is the pressure. $g$ is the gravitational acceleration vector.and $\alpha_{mnf}$ is the thermal diffusivity of the nanofluid. The parameter $\mu_a$ refers to the apparent viscosity. While $\tau$ denotes time. The quantities $K$ and represent the permeability of the porous medium and the inertial coefficient, respectively. It is noted that when the inertial term is negligible( $\tilde{K}=0$ ) Equation (2.2) reduces to the classical Darcy law.

The permeability and the inertial parameter $\widetilde{K}$ are evaluated using the (Ergun, 1952) correlation:.

$$K=\frac{d^2\varepsilon^2}{150\left(1-\varepsilon\right)^2},\tilde{K}=\frac{1.75d}{150\left(1-\varepsilon\right)} \tag{2.4}$$

Where $\varepsilon$ and $d$ represents the porosity and the particle diameter

The relationship between the electric current density $I$ and the fluid velocity $V$ is governed by Ohm's law:

$$I=\sigma\left(-\nabla\Phi+V\times B\right) \tag{2.5}$$

$$\nabla.I=0 \tag{2.6}$$

Where :

- $\sigma$ : electrical conductivity
- $\Phi$ : electric potential
- $-\nabla\Phi$ : the associated electric field.

According to (Garandet et al., 1992), Eq(2.5) and Eq(2.6) reduce to the Laplace equation $\nabla^2\Phi=0$, which, for an electrically insulated cavity, admits a unique solution of the form $\nabla\Phi=0$

Upon considering the governing equations in the x and y directions, the resulting system of equations is as follows:

$$\frac{\partial u}{\partial x}+\frac{\partial v}{\partial y}=0 \tag{2.7}$$

$$\frac{\mu_a}{K}\left(1+\frac{\tilde{K}}{\mu_a}\rho_{nf}\left|\vec{V}\right|\right).u=-\frac{\partial p}{\partial x}-\rho_{nf}g\sin\gamma+\sigma_{nf}\left(vB^2 sin\xi cos\xi-uB^2\sin^2\xi\right) \tag{2.8}$$

$$\frac{\mu_a}{K}\left(1+\frac{\tilde{K}}{\mu_a}\rho_{nf}\left|\vec{V}\right|\right).v=-\frac{\partial p}{\partial y}-\rho_{nf}g\cos\gamma+\sigma_{nf}\left(uB^2 sin\xi cos\xi-vB^2\cos^2\xi\right) \tag{2.9}$$

$$\frac{\partial T}{\partial\tau}+u\frac{\partial T}{\partial x}+v\frac{\partial T}{\partial y}=\alpha_{nf}\left(\frac{\partial^2 T}{\partial x^2}+\frac{\partial^2 T}{\partial y^2}\right) \tag{2.10}$$

Elimination of the pressure field from the momentum system is achieved through cross-differentiation, which entails taking the partial derivative of the x-momentum equation with respect to y and the y-momentum equation with respect to x, followed by the subtraction of the two resulting expressions. Implementing this cross-differentiation, in conjunction with the Boussinesq approximation for buoyancy,( $\rho_{nf}=\rho_{nf,0}\left[1-(\beta_T)_{nf}\left(T-T_c\right)\right]$ The final set of equations therefore describes the coupled magneto-convective transport of momentum and heat in a saturated porous medium, accounting for inertial porous resistance, magnetic damping, and thermal buoyancy.:

$$\begin{aligned}&\frac{\partial u}{\partial y}-\frac{\partial v}{\partial x}+\frac{\tilde{K}}{\mu_a}\rho_{nf}\left[\frac{\partial}{\partial y}\left(\left|\vec{V}\right|.u\right)-\frac{\partial}{\partial x}\left(\left|\vec{V}\right|.v\right)\right]=-\frac{gK\rho_{nf}}{\mu_a}\beta_{T_{nf}}\left(\frac{\partial T}{\partial x}\cos\gamma+\frac{\partial T}{\partial y}\sin\gamma\right)\\&+\frac{\sigma_{nf}KB_0^2}{\mu_a}\left(\frac{\partial u}{\partial y}\sin^2\xi+2\frac{\partial v}{\partial y}sin\xi cos\xi+\frac{\partial v}{\partial x}\cos^2\xi\right)\end{aligned} \tag{2.11}$$

$$\frac{\partial T}{\partial\tau}+u\frac{\partial T}{\partial x}+v\frac{\partial T}{\partial y}=\alpha_{nf}\left(\frac{\partial^2 T}{\partial x^2}+\frac{\partial^2 T}{\partial y^2}\right) \tag{2.12}$$

The effective thermophysical properties of the nanofluid and hybrid nanofluid are given as follows:

Density was evaluated using the model proposed by :(Pak & Cho, 1998)

- For the nanofluid case

$$\rho_{nf}=(1-\phi)\rho_f+\phi\rho_p \tag{2.13}$$

- For the hybrid nanofluid case

$$\rho_{hnf}=\phi_{p1}\rho_{p1}+\phi_{p2}\rho_{p2}+\left(1-\phi_{p1}-\phi_{p2}\right)\rho_f \tag{2.14}$$

Specific heat capacity was determined using the formulation introduced by (Xuan & Roetzel, 2000)

- For the nanofluid case

$$(\rho Cp)_{nf} = (1-\phi)(\rho Cp)_f + \phi(\rho Cp)_p \tag{2.15}$$

- For the hybrid nanofluid case

$$(\rho Cp)_{hnf} = \phi_{p1}\rho_{p1}C_{p,p1} + \phi_{p2}\rho_{p2}C_{p,p2} + (1-\phi_{p1}-\phi_{p2})C_{p,f} \tag{2.16}$$

The coefficient of thermal expansion may be determined through the following approach.(Khanafer et al., 2003)

- For the nanofluid case

$$(\rho\beta_T)_{nf} = (1-\phi)(\rho\beta_T)_f + \phi(\rho\beta)_p \tag{2.17}$$

- For the hybrid nanofluid case

$$(\rho\beta_T)_{hnf} = (1-\phi_{p1}-\phi_{p2})\rho_f\beta_f + \phi_{p1}\rho_{p1}\beta_{p_1} + \phi_{p2}\rho_{p2}\beta_{p_2} \tag{2.18}$$

Viscosity was calculated using (Brinkman, 1952) model

- For the nanofluid case

$$\mu_{nf} = \frac{\mu_f}{(1-\phi)^{2.5}} \tag{2.19}$$

- For the hybrid nanofluid case

$$\mu_{hnf} = \frac{\mu_f}{(1-\phi_{p1}-\phi_{p2})^{2.5}} \tag{2.20}$$

Thermal and Electrical conductivity were evaluated respectively using the (Maxwell, 1904) model

- For the nanofluid case

$$K_{nf} = K_f\left[\frac{(K_p+2K_f)-2\phi(K_f-K_p)}{(K_p+2K_f)+2\phi(K_f-K_p)}\right] \tag{2.21}$$

$$\frac{\sigma_{nf}}{\sigma_f} = 1+\frac{3(\chi-1)\phi}{(\chi+2)-(\chi-1)\phi} \tag{2.22}$$

Where $f$ and $P$ stand for the base fluid and the nanoparticle,$\phi$ for the particle volume fraction, and $\chi = \sigma_p / \sigma_f$

- For the hybrid nanofluid case

$$k_{hnf} = k_f \left[ \frac{\left( \frac{\phi_{p1}k_{p1} + \phi_{p2}k_{p2}}{\phi_{hnf}} \right) + 2k_f + 2\left(\phi_{p1}k_{p1} + \phi_{p2}k_{p2}\right) - 2\phi_{hnf}k_{bf}}{\left( \frac{\phi_{p1}k_{p1} + \phi_{p2}k_{p2}}{\phi_{hnf}} \right) + 2k_f - \left(\phi_{p1}k_{p1} + \phi_{p2}k_{p2}\right) + \phi_{hnf}k_f} \right] \quad (2.23)$$

$$\sigma_{hnf} = \sigma_f \left[ 1 + \frac{3\left(\sigma_{hnp} - \sigma_f\right)\phi_{hnf}}{\left(\sigma_{hnp} + 2\sigma_f\right) - \left(\sigma_{hnp} - \sigma_f\right)\phi_{hnf}} \right] \quad (2.24)$$

Where $\phi_{hnf} = \phi_{p1} + \phi_{p2}$ and $\sigma_{hnp} = \frac{\phi_{p1}\sigma_{p1} + \phi_{p2}\sigma_{p2}}{\phi_{hnf}}$

The effective thermal conductivity predicted by the Maxwell model (Eq. (2.21)) is strictly valid for nanofluids containing spherical nanoparticles. Accordingly, this model has been employed in the present work for estimating the thermal conductivity of the $Al_2O_3$-water nanofluid. However, due to their cylindrical geometry, single-walled carbon nanotubes (SWCNTs) do not conform to the assumptions underlying the Maxwell formulation. Therefore, for the SWCNT–water nanofluid, the effective thermal conductivity is calculated using the model proposed by(Xue, 2005) which explicitly accounts for the nanotubes' spatial configuration and aspect ratio effects.:

$$K_{nf} = k_f \left[ \frac{1 - \phi + 2\phi \frac{K_{CNT}}{K_{CNT} - K_f} \ln\left( \frac{K_{CNT} + K_f}{2K_f} \right)}{1 - \phi + 2\phi \frac{K_f}{K_{CNT} - K_f} \ln\left( \frac{K_{CNT} + K_f}{2K_f} \right)} \right] \quad (2.25)$$

The thermophysical characteristics of the base fluid (water) and the nanoparticles utilized (SWCNT, $Al_2O_3$, and Cu) are provided in Table 2.1.(Alilat, Alliche, Rebhi, & Chamkha, 2020; Ghalambaz et al., 2019)

*Table 2-1:Thermophysical properties of base fluid (water) and nanoparticles used*

| **Physical Properties** | **Water** | **SWCNT** | **Cu** | **$Al_2O_3$** |
|---|---|---|---|---|
| $C_p\ (J \cdot kg^{-1} \cdot K^{-1})$ | 4179 | 425 | 385 | 765 |
| $k$ ($W \cdot m^{-1} \cdot K^{-1}$) | 0.613 | 6600 | 401 | 40 |
| $\beta$ ($K^{-1}$) | $21 \times 10^{-5}$ | $1.6 \times 10^{-5}$ | $1.67 \times 10^{-5}$ | $0.85 \times 10^{-5}$ |
| $\rho$ ($kg \cdot m^{-3}$) | 997.1 | 2600 | 8933 | 3970 |
| $\sigma(\Omega\, m^{-1})$ | 0.05 | $4.8 \times 10^{-7}$ | $5.96 \times 10^{7}$ | $35 \times 10^{6}$ |

This study views the nanofluid as non-Newtonian, in which the viscosity is expressed through the Carreau-Yasuda model(Carreau, 1968; Yasuda, 1979):

$$\mu_f = \mu_\infty + (\mu_0 - \mu_\infty)\left[1 + (E'\dot{\gamma}')^a\right]^{\frac{n-1}{a}} \quad (2.26)$$

Where:

- $\mu_f$ : base fluid viscosity (Pa·s)
- $\mu_0$: Zero-shear viscosity (Pa·s) (viscosity at very low shear rates)
- $\mu_\infty$: Infinite-shear viscosity (Pa·s) (viscosity at very high shear rates)
- $E'$ : Consistency index (s) (characteristic time)
- $n$ : Power-law index(dimensionless) (describes the degree of shear-thinning behavior)
- $a$ : Transition parameter (dimensionless) (controls the transition between Newtonian and power-law regions)
- $\dot{\gamma}'$ Effective Shear rate ($s^{-1}$ ). given by the following expression:

$$\dot{\gamma}' = \left\{2\left[\left(\frac{\partial u}{\partial x}\right)^2 + \left(\frac{\partial v}{\partial y}\right)^2\right] + \left[\frac{\partial u}{\partial y} + \frac{\partial v}{\partial x}\right]^2\right\}^{\frac{n-1}{2}} \quad (2.27)$$

After replacing equation (2.26) in equation (2.19) for the nanofluid case and in the equation (2.20) for the hybrid nanofluid. The apparent viscosity of the two cases assumes the following form:

$$\mu_a = \frac{\mu_\infty + (\mu_0 - \mu_\infty)\left[1 + (E'\dot{\gamma}')^a\right]^{\frac{n-1}{a}}}{(1-\phi)^{2.5}} \quad (2.28)$$

For convenience, this research assumes that the cavity is square. (L=H). Furthermore, the equations governing the problem are presented in dimensionless form. In this case, the dimensionless formulation is obtained by considering the following dimensionless parameters:

$$X = \frac{x}{L}, Y = \frac{y}{L},\ U = \frac{uL}{\alpha_f},\ V = \frac{vL}{\alpha_f}, \theta = \frac{T - T_C}{\Delta T}, t = \frac{\tau \alpha_f}{HL}, \eta = \frac{\mu_a}{\mu_0},\ U = \frac{\partial \Psi}{\partial Y},\ V = -\frac{\partial \Psi}{\partial X}\ . \quad (2.29)$$

The introduction of Eqs. (2.13)–(2.25) of thermophysical properties of nanofluid and hybrid nanofluid and dimensionless variables (2.29) into Eqs. (2.11)–(2.12) results in the governing equations in their dimensionless form:

- For the nanofluid case :

$$\left[\eta_{nf} + V_a \times G \times F_{nf}(\phi)\right]\nabla^2\Psi + \frac{G \times F_{nf}(\phi)}{V_a} S_{Q1} = -R_T . H_{nf}(\phi)\left(\frac{\partial \theta}{\partial X}\cos\gamma - \frac{\partial \theta}{\partial Y}\sin\gamma\right) - Ha^2 C_{nf} S_{Q2} \quad (2.30)$$

$$\frac{\partial \theta}{\partial t} + \frac{\partial \psi}{\partial Y}\frac{\partial \theta}{\partial X} - \frac{\partial \psi}{\partial X}\frac{\partial \theta}{\partial Y} = E_{nf}(\phi)\left(\frac{\partial^2 \theta}{\partial X^2} + \frac{\partial^2 \theta}{\partial Y^2}\right) \quad (2.31)$$

- For the hybrid nanofluid case :

$$\left[\eta_{hnf}+V_a\times G\times F_{hnf}\left(\phi_{hnf}\right)\right]\nabla^2\Psi+\frac{G\times F_{hnf}\left(\phi_{hnf}\right)}{V_a}S_{Q1}=-R_T.H_{hnf}\left(\phi_{hnf}\right)\left(\frac{\partial\theta}{\partial X}\,cos\gamma-\frac{\partial\theta}{\partial Y}\,sin\gamma\right)-Ha^2C_{hnf}S_{Q2} \tag{2.32}$$

$$\frac{\partial\theta}{\partial t}+\frac{\partial\psi}{\partial Y}\frac{\partial\theta}{\partial X}-\frac{\partial\psi}{\partial X}\frac{\partial\theta}{\partial Y}=E_{hnf}\left(\phi_{hnf}\right)\left(\frac{\partial^2\theta}{\partial X^2}+\frac{\partial^2\theta}{\partial Y^2}\right) \tag{2.33}$$

Where $\eta$ is the dimensionless form of the apparent viscosity for the two cases, the conventional and the hybrid nanofluid, which takes the following form.

$$\eta\left(\dot{\gamma}\right)=\frac{s+\left(1-s\right)\left[1+\left(E\dot{\gamma}\right)^a\right]^{\frac{n-1}{a}}}{\left(1-\phi\right)^{2.5}} \tag{2.34}$$

Where $s=\mu_\infty/\mu_0$ is the viscosity ratio, $E=E'/\left(\alpha_f L^2\right)$ is a dimensionless characteristic time, and $\dot{\gamma}$ is the dimensionless magnitude of the effective shear rate, which is given as:

$$\left(\dot{\gamma}\right)=\sqrt{4\left(\frac{\partial\Psi}{\partial \mathrm{X}\partial \mathrm{Y}}\right)^2+\left(\frac{\partial^2\Psi}{\partial \mathrm{Y}^2}-\frac{\partial^2\Psi}{\partial \mathrm{X}^2}\right)^2} \tag{2.35}$$

The parameters $S_{Q1},S_{Q2},G,Ha,R_T\ and\ Va$ are defined as follows:

$$\left.\begin{aligned}S_{Q1}&=\left[\left(\frac{\partial\Psi}{\partial X}\right)^2\frac{\partial^2\Psi}{\partial X^2}+\left(\frac{\partial\Psi}{\partial Y}\right)^2\frac{\partial^2\Psi}{\partial Y^2}+2\frac{\partial\Psi}{\partial X}\frac{\partial\Psi}{\partial Y}\frac{\partial^2\Psi}{\partial X\partial Y}\right]\\ S_{Q2}&=\left[\frac{\partial^2\Psi}{\partial Y^2}\sin^2\xi+2\frac{\partial^2\Psi}{\partial X\partial Y}\sin\xi\cos\xi+\frac{\partial^2\Psi}{\partial X^2}\cos^2\xi\right]\\ R_T=\frac{gKLT\left(\rho\beta_T\right)_f}{\mu_f\alpha_f}&,V_a=\left[\left(\frac{\partial\Psi}{\partial X}\right)^2+\left(\frac{\partial\Psi}{\partial Y}\right)^2\right]^{\frac{1}{2}},G=\frac{\tilde{K}\alpha_f}{\nu_f L},Ha=B_0\sqrt{\frac{\sigma K}{\mu_f}}\end{aligned}\right\} \tag{2.36}$$

The dimensionless parameters that depend on the thermophysical properties of nanofluid and hybrid nanofluid ,which encompass the attributes of the base fluid and nanoparticles, along with the nanoparticle concentration are as follows:

- For the nanofluid case

$$\left.\begin{aligned} C_{nf} &= \left[1+\frac{3(\chi-1)\phi}{(\chi+2)-(\chi-1)\phi)}\right] \\ F_{nf}(\phi) &= \left(1-\phi+\phi\frac{\rho_p}{\rho_f}\right) \\ H_{nf}(\phi) &= \left(1-\phi+\phi\frac{(\rho\beta)_p}{(\rho_\beta)_f}\right) \\ E_{nf}(\phi) &= \frac{k_{nf}}{k_f}\frac{(\rho C_p)_f}{(1-\phi)(\rho C_p)_f+\phi(\rho C_p)_p} \end{aligned}\right\} \quad (2.37)$$

- For the hybrid nanofluid case

$$\left.\begin{aligned} C_{hnf} &= \left[1+\frac{3(\chi_1-1)\phi_{hnf}}{(\chi_1+2)-(\chi_1-1)\phi_{hnf})}\right], Where\ \chi_1=\frac{\phi_{p1}\sigma_{p1}+\phi_{p2}\sigma_{p2}}{\sigma_f} \\ F_{hnf}(\phi_{hnf}) &= 1-\phi_{hnf}+\frac{\phi_{p1}\rho_{p1}+\phi_{p2}\rho_{p2}}{\rho_f} \\ H_{hnf}(\phi_{hnf}) &= 1-\phi_{hnf}+\frac{\phi_{p1}(\rho\beta)_{p1}+\phi_{p2}(\rho\beta)_{p2}}{\rho_f} \\ E_{hnf}(\phi_{hnf}) &= \frac{k_{hnf}}{k_f}\frac{(\rho C_p)_f}{(1-\phi)(\rho C_p)_f+\phi_{p1}(\rho C_p)_{p2}+\phi_{p2}(\rho C_p)_{p2}} \end{aligned}\right\} \quad (2.38)$$

When $\phi=0\rightarrow F_{nf}(\phi)=H_{nf}(\phi)=E_{nf}(\phi)=1$ and $\phi_{hnf}=0\rightarrow F_{hnf}(\phi_{hnf})=H_{hnf}(\phi_{hnf})=E_{hnf}(\phi_{hnf})=1$ represents a clear fluid. $R_T$ is the Darcy-Rayleigh number, $G$ represents the parameter for inertial effects and $Ha$ is the Hartmann number. The governing equations (2.30)-(2.33) are suitable for application to Newtonian and non-Newtonian nanofluids in Darcian or non-Darcian porous media, with or without the magnetic field effect.

## 2.4. Boundary conditions

### 2.4.1. Hydrodynamic boundary conditions

The hydrodynamic boundary conditions ensure that no fluid penetrates the solid walls of the cavity. Therefore, the normal component of the velocity vanishes along all boundaries, implying impermeability. This condition is expressed as:

$$\left.\begin{aligned} X = \pm\frac{1}{2} \rightarrow \Psi = 0 \\ Y = \pm\frac{1}{2} \rightarrow \Psi = 0 \end{aligned}\right\} \tag{2.39}$$

### 2.4.2. Thermal boundary conditions

The adiabatic walls and different heating are described by these conditions.:

$$\left.\begin{aligned} X = -\frac{1}{2} \rightarrow \theta = 0.5 \\ X = +\frac{1}{2} \rightarrow \theta = -0.5 \\ Y = \pm\frac{1}{2} \rightarrow \frac{\partial\theta}{\partial Y} = 0 \end{aligned}\right\} \tag{2.40}$$

## 2.5. Quantifying Heat Transfer: Local and Average Nusselt Number Analysis

The investigation aims to determine the heat transfer rate by analyzing the local and average Nusselt numbers, which are defined as.

### 2.5.1. Local Nusselt Number

- For nanofluid

$$Nu = \frac{k_{nf}}{k_f}\left(\frac{\partial\theta}{\partial X}\right)_{X=\pm 0.5} \tag{2.41}$$

- For hybrid nanofluid

$$Nu = \frac{k_{hnf}}{k_f}\left(\frac{\partial\theta}{\partial X}\right)_{X=\pm 0.5} \tag{2.42}$$

### 2.5.2. Average Nusselt Number

$$Nu_m = \int_{-1/2}^{+1/2} Nu\, dY \tag{2.43}$$

where $\overline{Nu_R}$ and $\overline{Nu_L}$ denote the average Nusselt numbers evaluated along the right (cold) and the left (hot) vertical walls, respectively.

# CHAPTER 3
# NUMERICAL METHOD

# 3. CHAPTER III :NUMERICAL METHODOLOGY

This chapter presents the numerical strategy adopted to solve the system of nonlinear governing equations describing the physical behavior of the nanofluid and hybrid nanofluid under investigation. The Finite Difference Method (FDM) is employed due to its simplicity, robustness, and suitability for problems defined over regular geometries. Historically introduced by Euler in the 18th century, this method remains one of the most widely used numerical techniques for solving partial differential equations.

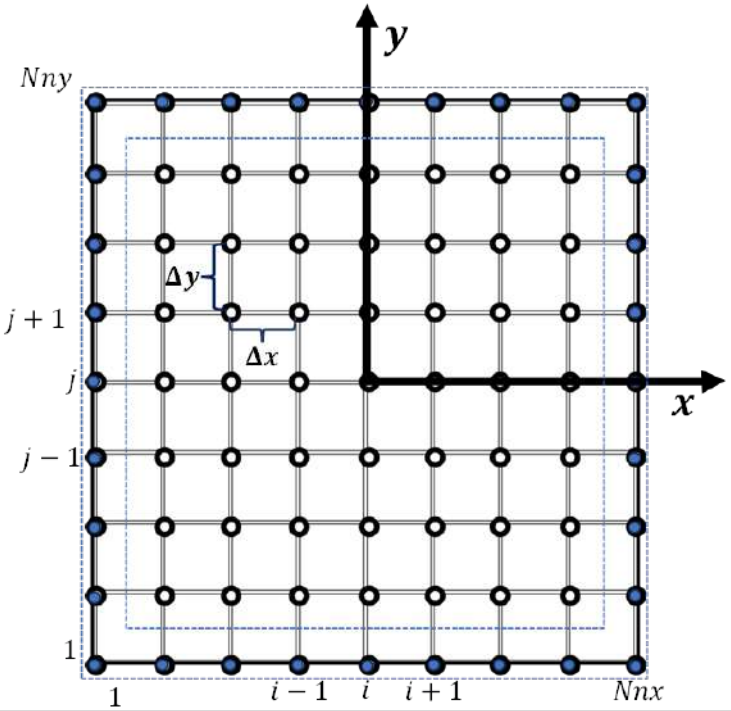



*Figure 3.1 Mesh size of the study area in (i,j)*

In the present study, the computational domain is discretized using a structured uniform mesh in a Cartesian coordinate system. Each node of the mesh is identified by two indices (i,j), corresponding to the intersection of grid lines along the x- and y-directions. Neighboring nodes are obtained by incrementing or decrementing these indices by one integer unit.

The energy equations (2.31) and (2.33) are discretized using a second-order centered scheme for spatial derivatives. The convective terms are treated in conservative form. To solve the resulting algebraic system at each time step, the Alternating Direction Implicit (ADI) scheme is employed (Peaceman & Rachford, 1955)he ADI technique decomposes each time step into two fractional steps:

- .In the first half-step, the equations are treated implicitly along the x-direction and explicitly along the y-direction.

- In the second half-step, the equations are treated implicitly along the y-direction and explicitly along the x-direction.

This decomposition yields two tridiagonal matrix systems per time step. The solution progresses by sweeping the computational domain line-by-line, first along the x-direction and then along the y-direction.

Subsequently, the stream function field (Ψ) is calculated from the discretized momentum equation (2.30) (2.32) using a classical centered scheme. The resulting system is solved with the Successive Overrelaxation (SOR) method, based on the temperature field at time (n+1) Δt. Proposed by (Frankel, 1950) and (Young, 1950)The SOR method is an iterative technique that explicitly computes the value of Ψ at the node under consideration for time (n+1) Δt. The process continues for enough iterations to ensure convergence to the desired accuracy.

## 3.1. Thermal boundary conditions discretization

The boundary conditions, Eqs. (2.39) and (2.40) , are discretized using a finite difference scheme. This scheme employs second-order accuracy and is decentered either to the right or to the left, depending on the specific wall being analyzed:

### 3.1.1. For the adiabatic and impermeable walls:

$$\theta_{i,1} = \frac{4\theta_{i,2} - \theta_{i,3}}{3} \qquad at \qquad Y = -\frac{1}{2} \tag{3.1}$$

$$\theta_{I,Nny} = \frac{4\theta_{i,Nny-1} - \theta_{i,Nny-2}}{3} \qquad at \qquad Y = +\frac{1}{2} \tag{3.2}$$

### 3.1.2. For active walls

$$\theta_{1,j} = \frac{4\theta_{2,j} - \theta_{3,j} + 2\Delta X}{3} \qquad at \qquad X = -\frac{1}{2} \tag{3.3}$$

$$\theta_{Nnx,j} = \frac{4\theta_{Nnx-1,j} - \theta_{Nnx-2,j} - 2\Delta X}{3} \qquad at \qquad X = +\frac{1}{2} \tag{3.4}$$

## 3.2. Energy equation discretization

The energy equation is parabolic in time and elliptic in space; therefore, the Alternating Direction Implicit (ADI) method is adopted as the numerical solution strategy. Based on Eqs. (2.31) and (2.33), the general form of the energy equation is expressed as::

$$\frac{\partial \theta}{\partial t}+\frac{\partial (U\theta)}{\partial X}+\frac{\partial (V\theta)}{\partial Y}=E(\phi)\left(\frac{\partial^2 \theta}{\partial X^2}+\frac{\partial^2 \theta}{\partial Y^2}\right) \tag{3.5}$$

Considering that in the case of the conventional nanofluid $E(\phi)=E_{nf}(\phi)$ and in the case of hybrid nanofluid $E(\phi)=E_{hnf}(\phi_{hnf})$

### 3.2.1. **Implicit Scheme in the x-Direction and Explicit in the y-Direction**

In this sub-step, the second-order derivatives in the x-direction are evaluated at time level (n+1/2), while those in the y-direction are treated explicitly at time level n. Each term in equation (3.5) is discretized as follows:

$$\left.\frac{\partial^2 \theta}{\partial X^2}\right|_{i,j}=\frac{\theta_{i+1,j}^{n+1/2}-2\theta_{i,j}^{n+\frac{1}{2}}+\theta_{i-1,j}^{n+1/2}}{\Delta X^2}, \qquad \left.\frac{\partial^2 \theta}{\partial Y^2}\right|_{i,j}=\frac{\theta_{i,j+1}^{n}-2\theta_{i,j}^{n}+\theta_{i,j-1}^{n}}{\Delta Y^2}. \tag{3.6}$$

$$\left.\frac{\partial (U\theta)}{\partial X}\right|_{i,j}=\frac{U_{i+1,j}^{n}\theta_{i+1,j}^{n+1/2}-U_{i-1,j}^{n}\theta_{i-1,j}^{n+1/2}}{2\Delta X}, \qquad \left.\frac{\partial (V\theta)}{\partial Y}\right|_{i,j}=\frac{-V_{i,j-1}^{n}\theta_{i,j-1}^{n}}{2\Delta Y} \tag{3.7}$$

$$\left.\frac{\partial \theta}{\partial t}\right|_{i,j}=2\frac{\theta_{i,j}^{n+1/2}-\theta_{i,j}^{n}}{\Delta t} \tag{3.8}$$

By substituting Eqs. (3.6)–(3.8) into Eq. (3.5), the following tridiagonal matrix system is obtained:

$$A_i\theta_{i+1,j}^{n+\frac{1}{2}}+B_i\theta_{i,j}^{n+\frac{1}{2}}+C_i\theta_{i-1,j}^{n+\frac{1}{2}}=D_i \tag{3.9}$$

with coefficients:

$$A_i=\left[\frac{U_{i+1,j}^{n}}{2\Delta X}-\frac{E(\phi)}{\Delta X^2}\right],\ B_i=2\left[\frac{1}{\Delta t}+\frac{E(\phi)}{\Delta X^2}\right],\ C_i=-\left[\frac{U_{i-1,j}^{n}}{2\Delta X}+\frac{E(\phi)}{\Delta X^2}\right] \tag{3.10}$$

$$D_i=\left[-\frac{V_{i,j+1}^{n}}{2\Delta Y}+\frac{E(\phi)}{\Delta Y^2}\right]\theta_{i,j+1}^{n}+2\left[\frac{1}{\Delta t}-\frac{E(\phi)}{\Delta Y^2}\right]\theta_{i,j}^{n}+\left[\frac{V_{i,j-1}^{n}}{2\Delta Y}+\frac{E(\phi)}{\Delta Y^2}\right]\theta_{i,j-1}^{n} \tag{3.11}$$

Applying boundary conditions (3.1)–(3.4) into equation (3.9) yields the discrete implicit form in the x-direction:

For: $i=2$

$$\left[A_2-\frac{1}{3}C_2\right]\theta_{3,j+1}^{n+1/2}+\left[B_2+\frac{4}{3}C_2\right]\theta_{2,j}^{n+1/2}+C_2\theta_{1,j}^{n+1/2}=D_2-\frac{2}{3}C_2\Delta X \tag{3.12}$$

For : $i = N_{nx-1}$

$$\left[\frac{4}{3}A_{Nnx-1} + B_{Nnx-1}\right]\theta^{n+\frac{1}{2}}_{Nnx-1,j} + \left[C_{Nnx-1} - \frac{1}{3}A_{Nnx-1}\right]\theta^{n+\frac{1}{2}}_{Nnx-2,j} = D_{Nnx-1} + \frac{2}{3}A_{Nnx-1}\Delta X \qquad (3.13)$$

### 3.2.2. **Implicit Scheme in the y-Direction and Explicit in the x-Direction**

In the second sub-step, spatial derivatives in the y-direction are treated implicitly at time level (n+1), while derivatives in the x-direction are handled explicitly at time level (n+1/2). The corresponding discretizations are:

$$\left.\frac{\partial^2\theta}{\partial X^2}\right|_{i,j} = \frac{\theta^{n+\frac{1}{2}}_{i+1,j} - 2\theta^{n+\frac{1}{2}}_{i,j} + \theta^{n+\frac{1}{2}}_{i-1,j}}{\Delta X^2}, \qquad \left.\frac{\partial^2\theta}{\partial Y^2}\right|_{i,j} = \frac{\theta^{n+1}_{i,j+1} - 2\theta^{n+1}_{i,j} + \theta^{n+1}_{i,j-1}}{\Delta X^2} \qquad (3.14)$$

$$\left.\frac{\partial(U\theta)}{\partial X}\right|_{i,j} = \frac{U^n_{i+1,j}\theta^{n+1/2}_{i+1,j} - U^n_{i-1,j}\theta^{n+1/2}_{i-1,j}}{2\Delta X}, \qquad \left.\frac{\partial(V\theta)}{\partial Y}\right|_{i,j} = \frac{V^n_{i,j+1}\theta^{n+1}_{i,j+1} - V^n_{i,j-1}\theta^{n+1}_{i,j-1}}{2\Delta Y} \qquad (3.15)$$

$$\left.\frac{\partial\theta}{\partial t}\right|_{i,j} = 2\frac{\theta^{n+1}_{i,j} - \theta^{n+\frac{1}{2}}_{i,j}}{\Delta t} \qquad (3.16)$$

By substituting Eqs. (3.14)–(3.16) into Eq. (3.5), the following tridiagonal matrix system is obtained:

$$A'_j\theta^{n+1}_{i,j+1} + B'_j\theta^{n+1}_{i,j} + C'_j\theta^{n+1}_{i,j-1} = D'_j \qquad (3.17)$$

with coefficients :

$$A'_j = \left[\frac{V^n_{i,j+1}}{2\Delta Y} - \frac{E(\phi)}{\Delta Y^2}\right],\ B'_j = 2\left[\frac{1}{\Delta t} + \frac{E(\phi)}{\Delta Y^2}\right],\ C'_j = -\left[\frac{V^n_{i,j-1}}{2\Delta Y} + \frac{E(\phi)}{\Delta Y^2}\right] \qquad (3.18)$$

$$D'_i = \left[-\frac{U^n_{i+1,j}}{2\Delta X} + \frac{E(\phi)}{\Delta X^2}\right]\theta^{n+1/2}_{i+1,j} + 2\left[\frac{1}{\Delta t} - \frac{E(\phi)}{\Delta X^2}\right]\theta^{n+1/2}_{i,j} + \left[\frac{U^n_{i-1,j}}{2\Delta X} + \frac{E(\phi)}{\Delta X^2}\right]\theta^{n+1/2}_{i-1,j} \qquad (3.19)$$

Applying boundary conditions (3.1)–(3.4) into equation (3.17) yields the discrete implicit form in the y-direction:

For : $j = 2$

$$\left[A'_2 - \frac{1}{3}C'_2\right]\theta^{n+1}_{i,3} + \left[B'_2 + \frac{4}{3}C'_2\right]\theta^{n+1}_{i,2} = D'_2 \qquad (3.20)$$

For : $j = N_y$

$$\left[\frac{4}{3}A'_{Nny-1} + B'_{Nny-1}\right]\theta^{n+1}_{i-Nny-1} + \left[C'_{Nny-1} - \frac{1}{3}A'_{Nny-1}\right]\theta^{n+1}_{i,Nny-2} = D_{Nny-1} \qquad (3.21)$$

### 3.3. **Momentum equation discretization**

The general form of the momentum equation is expressed as::

$$\left[\eta + V_a \times G \times F(\phi)\right]\nabla^2\Psi + \frac{G \times F(\phi)}{V_a}\left[U^2\frac{\partial^2\Psi}{\partial X^2} + V^2\frac{\partial^2\Psi}{\partial Y^2} - 2UV\frac{\partial^2\Psi}{\partial X \partial Y}\right] = -R_T.H(\phi)\left(\frac{\partial\theta}{\partial X}\cos\gamma - \frac{\partial\theta}{\partial Y}\sin\gamma\right) - Ha^2 C_1 S_{Q2} \quad (3.22)$$

For the nanofluid case $\eta = \eta_{nf}, F(\phi) = F_{nf}(\phi), H(\phi) = H_{nf}(\phi)$ and $C_1 = C_{nf}$ and for the hybrid nanofluid case $\eta = \eta_{nf}$ , $F(\phi) = F_{hnf}(\phi_{hnf}), H(\phi) = H_{hnf}(\phi_{hnf})$ and $C_1 = C_{nf}$

Prior to the discretization of equation (3.22), it is assumed that the variables $V_a$, $U$, and $V$ are already known. Each term of the equation is discretized using a classical centered scheme.

$$\left.\frac{\partial^2\Psi}{\partial X^2}\right|_{i,j} = \frac{\Psi^{n+1}_{i+1,j} - 2\Psi^{n+1}_{i,j} + \Psi^{n+1}_{i-1,j}}{\Delta X^2}, \quad \left.\frac{\partial^2\Psi}{\partial Y^2}\right|_{i,j} = \frac{\Psi^{n+1}_{i,j+1} - 2\Psi^{n+1}_{i,j} + \Psi^{n+1}_{i,j-1}}{\Delta X^2} \quad (3.23)$$

$$\left.\frac{\partial\theta}{\partial X}\right|_{i,j} = \frac{\theta^{n+1}_{i+1,j} - \theta^{n+1}_{i-1,j}}{2\Delta X} \quad , \left.\frac{\partial\theta}{\partial Y}\right|_{i,j} = \frac{\theta^{n+1}_{i,j+1} - \theta^{n+1}_{i,j-1}}{2\Delta Y} \quad (3.24)$$

A cross discretization is applied to the term below:

$$\left.\frac{\partial^2\Psi}{\partial X \partial Y}\right|_{i,j} = \frac{1}{4\Delta x \Delta y}\left[\Psi^{n+1}_{i+1,j+1} - \Psi^{n+1}_{i-1,j+1} + \Psi^{n+1}_{i-1,j-1} - \Psi^{n+1}_{i+1,j-1}\right] \quad (3.25)$$

By substituting expressions Eqs (3.23)-(3.25) into Eq (3.22), the general expression of the following function is obtained:

$$\Psi^{(n+1),(k+1)}_{i,j} = \Psi^{(n+1),k}_{i,j} + \omega\left\{\begin{array}{l} a_x(\Psi^{(n+1),k}_{i+1,j} + \Psi^{(n+1),(k+1)}_{i-1,j}) + a_y(\Psi^{(n+1),k}_{i,j+1} + \Psi^{(n+1),(k+1)}_{i,j-1}) \\ +a_{xy}(\Psi^{(n+1),k}_{i+1,j+1} - \Psi^{(n+1),k}_{i-1,j+1} + \Psi^{(n+1),(k+1)}_{i-,j-1} - \Psi^{(n+1),k}_{i+1,j-1}) \\ +a_{TSx}(T^{(n+1)}_{i+1,j} - T^{(n+1)}_{i-1,j}) + a_{TSy}(T^{(n+1)}_{i,j+1} - T^{(n+1)}_{i,j+1}) \end{array}\right\} \quad (3.26)$$

Where the parameters ap, $a_x$, $a_y$, $a_{xy}$, $a_{TSx}$, and $a_{TSy}$ are defined as follows:

$$a_p = \frac{\left(\begin{array}{l} 2\left(\eta + V_a \cdot F(\phi)\cdot G\right)\left(\Delta X^2 + \Delta Y^2\right)V_a + \\ \left(V^2\Delta Y^2 + U^2\Delta X^2\right)F(\phi)\cdot G + \\ Ha^2.C_1.Va\left(\sin^2\xi.\Delta x^2 + \cos^2\xi.\Delta y^2\right) \end{array}\right)}{V_a \Delta X^2 \Delta Y^2} \quad (3.27)$$

$$a_x = \frac{\left[\left(\eta + V_a \cdot G \cdot F(\phi) + Ha^2.C_1.\cos^2\xi\right)V_a + V^2.G.F(\phi)\right]}{V_a.\Delta X^2 \cdot a_p} \tag{3.28}$$

$$a_y = \frac{\left[\left(\eta + V_a \cdot G \cdot F(\phi) + Ha^2.C_1.\sin^2\xi\right)V_a + U^2.G.F(\phi)\right]}{V_a.\Delta Y^2 \cdot a_p} \tag{3.29}$$

$$a_{xy} = \frac{[-U.V.G.F(\phi) + Ha^2.C_1.\sin\xi.Va]}{2V_a\Delta X\Delta Y \cdot a_p} \tag{3.30}$$

$$a_{TSx} = \frac{R_T H(\phi)\cos\gamma}{2\Delta X \cdot a_p}, a_{TSy} = -\frac{R_T H(\phi)\sin\gamma}{2\Delta Y \cdot a_p} \tag{3.31}$$

The parameter $\omega$ is the over-relaxation factor, used to accelerate convergence. Its optimal value lies in the interval $1<\omega_{opt}<2$ and, for a rectangular uniformly discretized domain, is estimated by:

$$\omega_{opt} = \frac{2}{\zeta^2}\left[1-\sqrt{1-\zeta^2}\right] \tag{3.32}$$

Where:

$$\zeta = \frac{\cos\left(\frac{\pi}{N_{x+1}}\right) + \left(\frac{\Delta x^2}{\Delta y^2}\right)\cos\left(\pi / N_{y+1}\right)}{1+\left(\Delta x^2 / \Delta y^2\right)} \tag{3.33}$$

$N_{x+1}$ and $N_{y+1}$ denote the number of grid nodes in the x and y directions, respectively.

### 3.4. **Velocity fields discretization**

Using the relations in equation (2.29), the velocity field's components (U,V) are obtained from the stream function. Employing a first-order centered finite difference scheme to discretize these equations produces the following results:

$$U_{i,j}^{n+1} = \frac{\Psi_{i,j+1}^{n+1} - \Psi_{i,j-1}^{n+1}}{2\Delta Y} \tag{3.34}$$

$$V_{i,j}^{n+1} = \frac{\Psi_{i,j+1}^{n+1} - \Psi_{i,j-1}^{n+1}}{2\Delta X} \tag{3.35}$$

### 3.5. **Discretization of velocity boundary conditions**

The boundary conditions of the velocity are discretized using a finite difference scheme, decentered to the right or left, with third-order accuracy:

$$\left.\begin{aligned} U_{1,j}=0, \quad V_{i,1}=-\frac{18\Psi_{2,j}-9\Psi_{3,j}+2\Psi_{4,j}}{6\Delta X}\, at\ X=-\frac{1}{2} \\ U_{Nnx,j}=0\ ,\ V_{i,Nny}=\frac{18\Psi_{Nnx-1,j}-9\Psi_{Nnx-2,j}+2\Psi_{Nnx-3,j}}{6\Delta X}\, at\ X=\frac{1}{2} \end{aligned}\right\} \quad (3.36)$$

$$\left.\begin{aligned} V_{i,1}=0, \quad U_{1,j}=\frac{18\Psi_{i,2}-9\Psi_{i,3}+2\Psi_{i,4}}{6\Delta Y}\, at\ y=-\frac{1}{2} \\ V_{i,Nny}=0\ ,\ U_{Nnx,j}=-\frac{18\Psi_{i,Nny-1}-9\Psi_{i,Nny-2}+2\Psi_{i,Nny-3}}{6\Delta Y}\, at\ X=\frac{1}{2} \end{aligned}\right\} \quad (3.37)$$

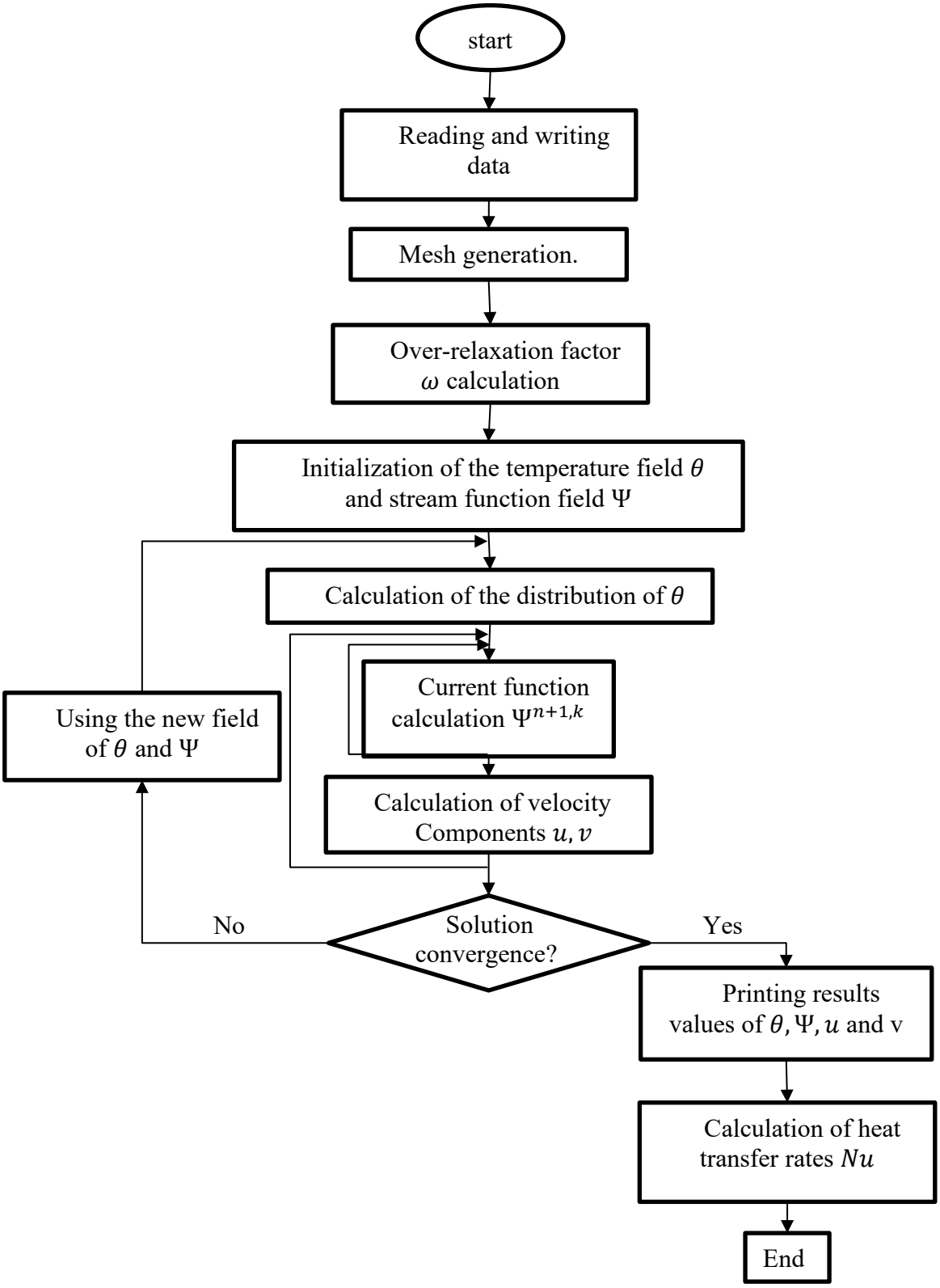
## 3.6. **Calculation algorithm**

The calculation algorithm is composed of the following primary steps

1. Mesh Generation: Create the computational grid.
2. Initialization and Data Input: Initialize parameters and read the input data.
3. Over-Relaxation Factor Calculation: Compute the optimal over-relaxation factor ω
4. Application of Initial Conditions: Apply initial conditions for temperature and the stream function .
5. Initial Velocity Field Assessment: Calculate the initial velocity components $U_{i.j}$ and $V_{i.j}$.
6. Start of the Time Loop
   a. Solve the energy equations (3.9) and (3.17) using the ADI method to compute the temperature field $\theta_{i.j}$
   b. Solve the motion equation (3.26) using the SOR method to calculate the stream function field
   c. Calculate the velocity components $U_{i,j}$ , $V_{i,j}$.
   d. Iterate step (a) until the solution reaches either a stable or oscillatory state.
7. Output Results: Print the computed results.
8. End of the program

The convergence criterion for solving equation (3.26) is defined as follows:

$$\frac{\sum_i \sum_j \left|\Psi_{i,j}^{k+1}-\Psi_{i,j}^{k}\right|}{\sum_i \sum_j \left|\Psi_{i,j}^{k}\right|} \leq 10^{-6}$$


start
Reading and writing data
Mesh generation.
Over-relaxation factor $\omega$ calculation
Initialization of the temperature field $\theta$ and stream function field Ψ
Calculation of the distribution of $\theta$
Current function calculation $\Psi^{n+1,k}$
Calculation of velocity Components $u, v$
Solution convergence?
No
Yes
Using the new field of $\theta$ and Ψ
Printing results values of $\theta, \Psi, u$ and v
Calculation of heat transfer rates $Nu$
End

# CHAPTER 4

# RESULTS AND DISCUSSION

# 4. CHAPTER IV: PRESENTATION AND DISCUSSION Of RESULTS

This chapter presents and discusses the results of natural convection for two non-Newtonian fluids within an inclined square porous cavity exposed to an external magnetic field. It is divided into two main sections. The first section presents the SWCNT–water nanofluid findings, while the second section highlights o ($Al_2O_3$–Cu/water) hybrid nanofluid. Each section examines the fluid flow, heat transfer performance, and the apparent viscosity behavior, which are studied with respect to numerous governing parameters. These include the four Carreau–Yasuda model parameters—namely the power-law index (n), the dimensionless time constant (E), the viscosity ratio between infinite and zero shear rates (s), and the dimensionless Carreau–Yasuda parameter (a)—in addition to the inertial parameter (G) ,the Hartmann number (Ha), the nanoparticle volume fraction ($\phi$), the Rayleigh number ($R_T$), and the inclination angle of the cavity ($\gamma$).

## 4.1. First Section: The Non-Newtonian SWCNT–Water Nanofluid

The objective of this numerical study is to examine the interrelations between the Hartmann number (Ha), the Carreau–Yasuda rheological parameters, ( $n, E, a$ , and $s$ ), and the inertia parameter (G), and their influences on the free convective heat transfer rate and flow intensity of a SWCNT–water non-Newtonian nanofluid within a saturated square porous medium. The numerical investigations were carried out under the conditions of $R_T = 200$ and $\xi = 0°$ The following ranges are to be considered: $0 \le Ha \le 10$; $0.2 \le n \le 1$; $0 \le E \le 100$; $0.2 \le a \le 1$; $0.2 \le s \le 1$; $0 \le G \le 10$; $0 \le \phi \le 0.1$; and $-90° \le \gamma \le 90°$.

Table 4-1 showcases an investigation into grid independence, wherein the grid resolution is altered from 20x20 to 120x120 while maintaining all the parameters constant, to assess the numerical stability of the maximum stream function ( $|\Psi|_{max}$ ) and average Nusselt number ( $\overline{Nu_l}$ ). The findings demonstrates significant discrepancies at lower grid resolutions. However, the convergence is achieved beyond 100x100. As indicated by marginal relative percentage variances ($\Delta$) signifying grid autonomy. Consequently, a grid size of 100x100 was opted for subsequent analyses, striking a balance between computational efficacy and solution precision.

*Table 4-1: the convergence tests conducted for $|\Psi|_{max}$ and $\overline{Nu_l}$ at $Ha = 2$, $G = 0.5$, $R_T = 200$ and $n = 1$.*

| Grid size | 20×20 | 40×40 | 60×60 | 80×80 | 100×100 | 120×120 |
|---|---|---|---|---|---|---|
| $\lvert\Psi\rvert_{max}$ | 2.28615 | 2.27678 | 2.27527 | 2.27478 | 2.27456 | 227445 |
| $\overline{Nu_l}$ | 2.2300 | 2.2315 | 2.2317 | 2.2318 | 2.2318 | 2.2318 |

| | | | | | | |
|---|---|---|---|---|---|---|
| $\Delta\lvert\Psi\rvert_{max} = \frac{\lvert\Psi_{i,j} - \Psi_{120\times120}\rvert}{\lvert\Psi_{120\times120}\rvert}\times100\%$ | 0.5 | 0.10 | 0.03 | 0.01 | 0.004 | - |
| $\Delta\overline{Nu_L} = \frac{\lvert\overline{Nu}_{l\,i,j} - \overline{Nu}_{l\,120\times120}\rvert}{\lvert\overline{Nu}_{l\,120\times120}\rvert}\times100\%$ | 0.08 | 0.01 | 0.004 | 0 | 0 | - |

The accuracy of the findings was ensured through a comprehensive validation process that involved comparing the outcomes with the previous studies.

Initially, the validation was conducted against the research of (Khechiba et al., 2017) and (Djamel et al., 2023), which utilized the Carreau–Yasuda viscosity model. Various values of $n$ were examined, and the comparison, depicted in Figs 4.1 and 4.2, Tables 4-2 and 4-3, demonstrated the concordance, thus affirming the precision of the current methodology.

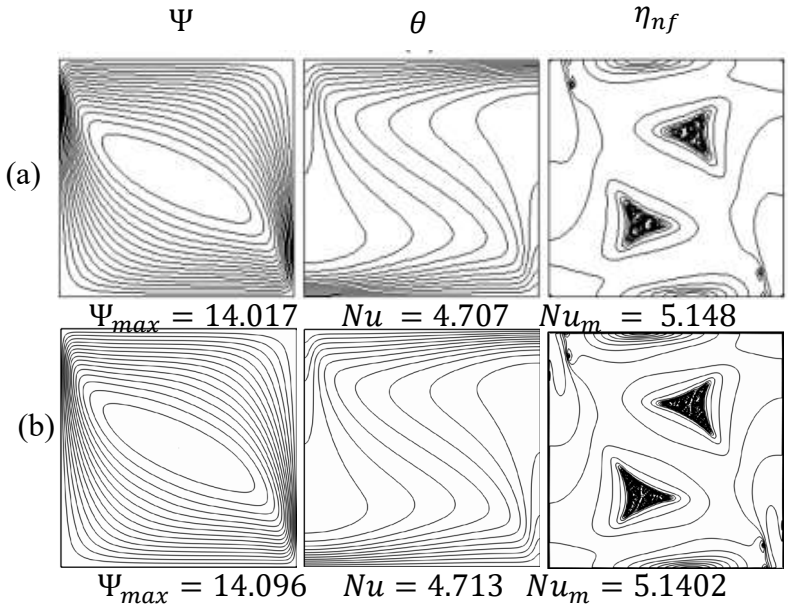



*Figure 4.1 validation in terms of streamline (in the left), isotherms (in the middle and the apparent viscosity) to what reported by (Khechiba et al., 2017)(a) with this present work (b) at $R_T = 70$, $n = 0.6$, $s = 0.01$, $E = 0.6$ and $a = 2$.*

*Table 4-2 comparison between the present results and those of (Khechiba et al., 2017) regarding of $\lvert\Psi\rvert_{max}$ and $Nu_m$ across various n values.*

| $n$ | Results of (*Khechiba et al., 2017*) | | Present work | | Present results vs . *Khechiba et al., 2017* | |
|---|---|---|---|---|---|---|
| | $\lvert\Psi\rvert_{max}$ | $Nu_m$ | $\lvert\Psi\rvert_{max}$ | $Nu_m$ | $\lvert\Delta\lvert\Psi\rvert_{max}\rvert$ | $\lvert\Delta Nu_m\rvert$ |
| 1.0 | 3.715 | 2.046 | 3.7234 | 2.0484 | 0.22 | 0.11 |

| | | | | | | |
|---|---|---|---|---|---|---|
| 0.8 | 6.685 | 3.178 | 6.68610 | 3.1752 | 0.014 | 0.088 |
| 0.6 | 14.017 | 5.148 | 14.096 | 5.1402 | 0.56 | 0.15 |

*Table 4-3 comparison between the present results and those of Djamel et al., 2023 regarding of across various n values.*

| $n$ | Results of Djamel et al., 2023. | | Present work | | Present results vs (Djamel et al., 2023) | |
|---|---|---|---|---|---|---|
| | $\lvert\Psi\rvert_{max}$ | $Nu_m$ | $\lvert\Psi\rvert_{max}$ | $Nu_m$ | $\lvert\Delta\lvert\Psi\rvert_{max}\rvert$ | $\lvert\Delta Nu_m\rvert$ |
| 1.0 | 2.828 | 2.359 | 2.830 | 2.369 | 0.07 | 0.42 |
| 0.8 | 2.983 | 2.399 | 2.988 | 2.409 | 0.16 | 0.41 |
| 0.6 | 3.091 | 2.426 | 3099 | 2.432 | 0.25 | 0.26 |

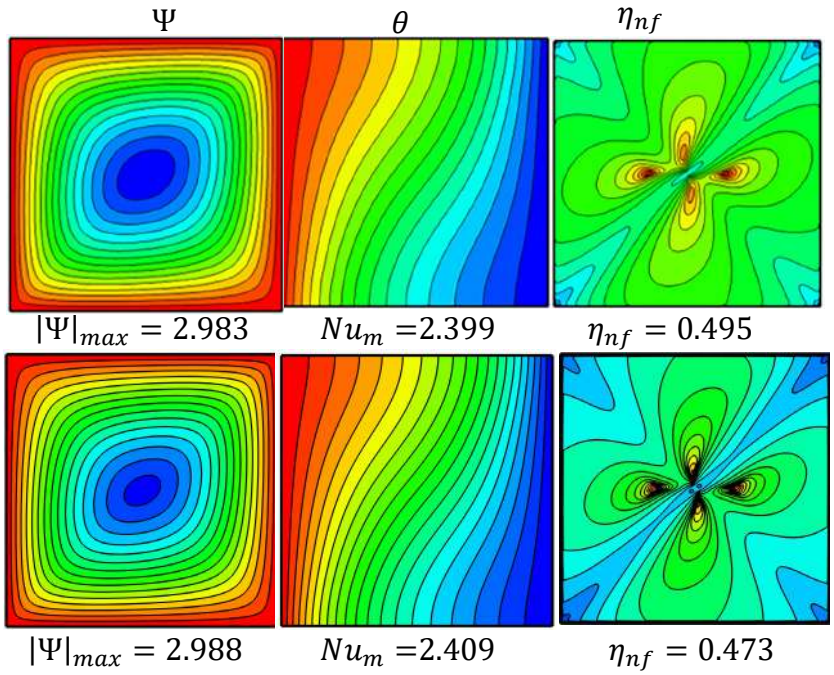



*Figure 4.2 validation in terms of streamline, isotherms and the apparent viscosity to what reported by (Djamel et al., 2023) (Top) with this present work (Bottom) at* $R_T = 200$, $n = 0.8$, $s = 0.01$, $E = 0.6$, $G = 0.5$ *and* $a = 2$.

Subsequently, further validation was carried out by comparing the results with another work by (Alilat, Alliche, Rebhi, & Chamkha, 2020), which utilized the Dupuit–Darcy model. The evaluation encompassed different Hartmann numbers to study the impact of the magnetic field. The coherence observed in Table 6 provided additional support for the robustness of the model.

*Table 4-4an additional comparative analysis with the study conducted by Alilat, Alliche, Rebhi, & Chamkha, 2020. across various values of Ha.*

| $Ha$ | Results of Alilat et al. (Alilat, Alliche, Rebhi, & Chamkha, 2020) | | Present work | | Present results vs Alilat et al. (Alilat, Alliche, Rebhi, & Chamkha, 2020) | |
|---|---|---|---|---|---|---|
| | $\lvert\Psi\rvert_{max}$ | $Nu_m$ | $\lvert\Psi\rvert_{max}$ | $Nu_m$ | $\lvert\Delta\lvert\Psi\rvert_{max}\rvert$ | $\lvert\Delta Nu_m\rvert$ |
| 0.0 | 1.052 | 1.970 | 1.0552 | 1.9699 | 0.30 | 0.005 |

| | | | | | | |
|---|---|---|---|---|---|---|
| 5.0 | 0.656 | 1.935 | 0.6557 | 1.9344 | 0.014 | 0.088 |
| 10 | 0.246 | 1.91 | 14.096 | 5.1402 | 0.56 | 0.15 |

Additionally, a qualitative validation of flow structure was conducted by comparing the streamline patterns with those reported by(Mahmud & Fraser, 2004) , as illustrated in Fig 4.3. The analysis revealed a high level of agreement in the flow pattern.

Collectively, these validation steps confirm the accuracy, robustness, and predictive capability of the numerical method used in this study..

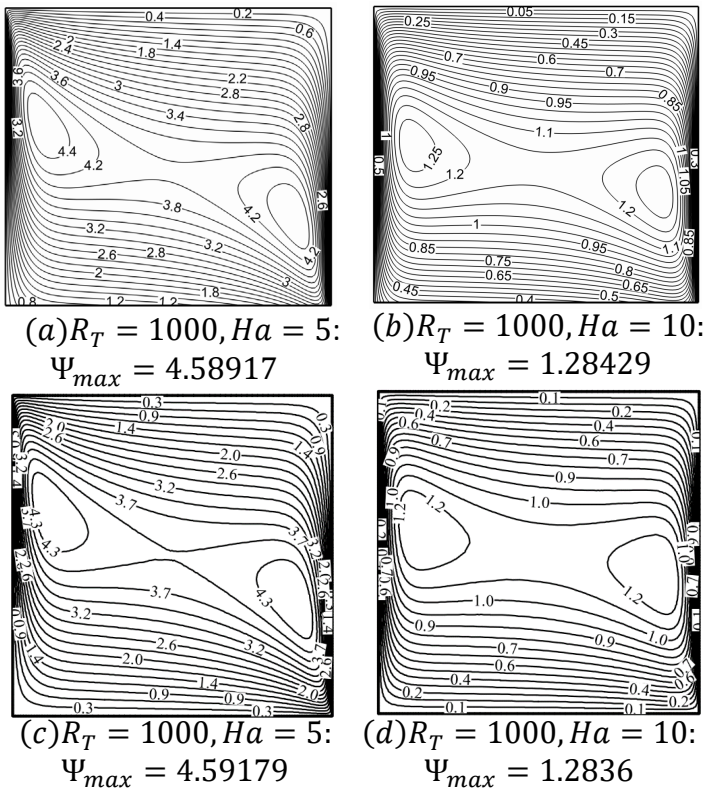



*Figure 4.3 Validation in terms of streamline for different Ha to with Mahmud & Fraser, 2004.*

Figure 4.4 examines how the Hartmann number Ha affects the stream function contours (Fig. 4.4.a), isotherm lines (Fig. 4.4.b), and apparent viscosity (Fig. 4.4.c) for $R_T = 200$ , $G = 0.5$ $\phi = 0.05, E = 0.6, n = 0.8$ $s = 0.01$ and $a = 2$. Strong internal circulation and a discernible clockwise convective cell are produced when buoyancy forces propel fluid motion in the square porous cavity in the absence of a magnetic field (Ha=0).

As the magnetic field is introduced and the Hartmann number increases, the resulting Lorentz force acts in opposition to the buoyancy-driven motion. This counteracting force diminishes the overall flow intensity and weakens the shear-thinning effects. Consequently, a substantial portion of the nanofluid exhibits reduced mobility, becoming nearly stagnant in the central region of the cavity, as depicted in Fig. 4.4a for $Ha = 10$.

The isotherm contours shown in (fig. 4.4 b) reveal that, with increasing Ha, the initially distorted temperature lines gradually become more parallel, signifying a transition from a convection-dominated regime to a quasi-conductive one. This stabilization reflects the suppression of convective transport due to the Lorentz force, which is corroborated by a notable decrease in the average Nusselt number from $\overline{Nu_L} = 2.2557$ to $\overline{Nu_L} = 1.9119$. The attenuation of convective motion reduces thermal boundary layer distortion, resulting in a more stratified temperature field. These observations are consistent with the findings reported by. (Alilat, Alliche, Rebhi, & Chamkha, 2020) .Furthermore, (Fig. 4.4 c) demonstrates that the apparent viscosity $\eta_{nf}$ increases progressively with the Hartmann number Ha, whereas the maximum stream function$|\Psi|_{max}$ (Fig. 4.4 a) decreases accordingly. This inverse relationship is characteristic of shear-thinning fluids. As the magnetic field strengthens (higher Ha), Lorentz forces dampen fluid motion, leading to a reduction in the local shear rate. This decrease in shear rate causes the non-Newtonian nanofluid to exhibit higher viscosity, approaching Newtonian behavior. At Ha=10, the apparent viscosity $\eta_{nf}$ tends toward unity ($\eta_{nf}$ ≈1), indicating that the applied magnetic field effectively suppresses non-Newtonian characteristics.

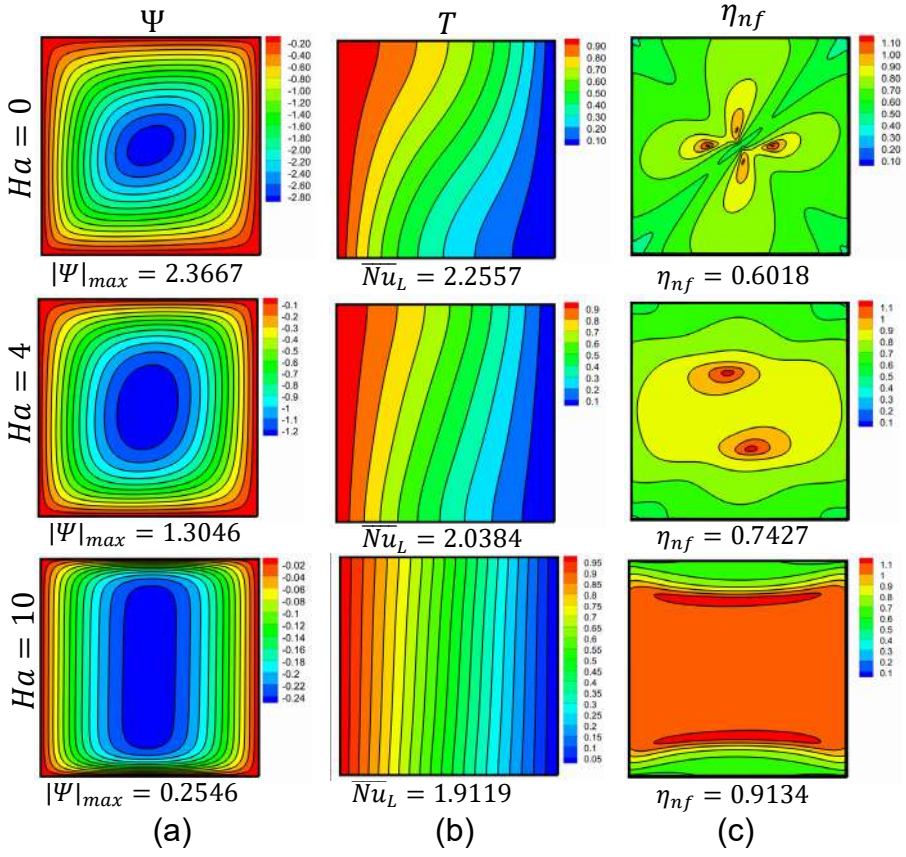



*Figure 4.4 Variation of Hartmann number (Ha) for streamlines (4a), isotherms (4b) and the apparent viscosity (4c) with the following parameters* $R_T = 200$ , $G = 0.5$ , $\gamma = 0, \phi = 0.05$, $E = 0.6, n = 0.8$ $s = 0.01$ *and* $a = 2$.

Figure 4.5 illustrates the influence of the power-law index(n) influence the stream function contours (Fig 4.5.a), isotherms lines(Fig 4.5.b), and apparent viscosity distributions (Fig 4.5.c) for three representative cases: $n = 1$ (Newtonian fluid), $n = 0.6$ and $n = 0.2$ (shear thinning fluid). As the value of $n$ decreases from $n = 1$ to $n = 0.2$, the flow within the cavity becomes significantly more vigorous, as reflected by the denser and more dynamic streamlines. This intensification of circulation enhances convective currents and consequently increases the overall heat transfer rate. The observed improvement in convective motion is primarily attributed to the reduction in effective viscosity under shear-thinning conditions, which promotes stronger fluid recirculation and the formation of more pronounced vortex structures within the cavity.

The impact of this rheological behavior on the thermal field is clearly visible in the isotherm distributions (Fig 4.5.b), Lower values of ($n$) produce steeper thermal gradients, signifying a more efficient heat transfer process resulting from diminished effective viscosity. (Fig 4.5.c) further substantiates this observation, displaying the spatial variation of the apparent viscosity $\eta_{nf}$. As $n$ decreases, the apparent viscosity markedly drops in regions of high shear, particularly near the central zone of the cavity where velocity gradients are most intense. This localized viscosity reduction enhances fluid mobility and reinforces the strength of convective circulation.

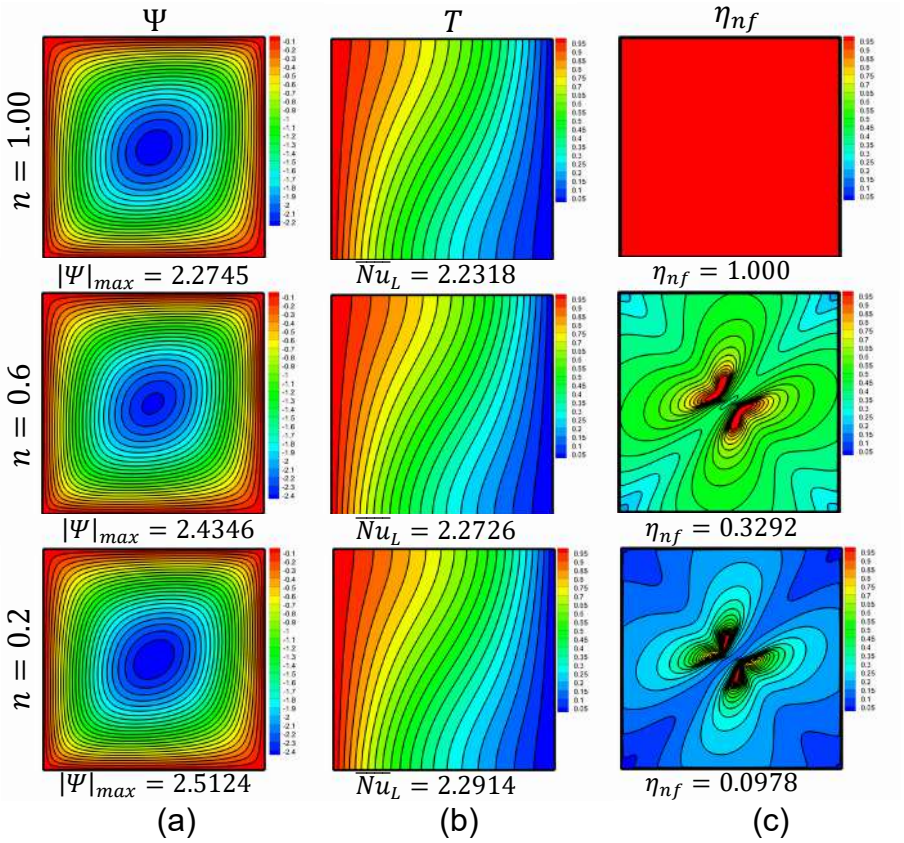



*Figure 4.5 Variation of the power law index(n) for streamlines (5a), isotherms (5b) and the apparent viscosity (5c) with the following parameters* $R_T = 200, Ha = 2, G = 0.5, \phi = 0.05, \gamma = 0°, E = 0.6, s = 0.01$ *and* $a = 2$

Figure 4.6 depicts the effects of varying single-walled carbon nanotube (SWCNT) concentrations (ϕ) on the stream function contours Ψ (Fig.4.6.a), temperature distribution $\theta$( Fig.4.6.b) and apparent viscosity fields $\eta_{nf}$ (Fig.4.6 .c) considering three nanoparticle volume fractions ($\phi$) = 0, 0.04 and 0.1. Across all cases, a single clockwise circulating cell is observed within the cavity. The introduction of a 4% SWCNT concentration leads to a noticeable enhancement in flow strength, as indicated by the increase in the maximum absolute stream function value from $|\Psi|_{max} = 2.31913$ to $|\Psi|_{max} = 2.4313$. reflecting intensified convective motion. This improvement is primarily attributed to the superior thermal conductivity of the nanofluid, which strengthens buoyancy-driven circulation within the porous cavity.

However, when the concentration of SWCNTs is further increased to $\phi = 0.10$ the flow intensity diminishes below that observed at 4% as a result of the pronounced rise in effective viscosity. The apparent viscosity contours in (Fig.4.6 c).clearly demonstrate this effect, where the increased viscous

resistance limits fluid mobility and weakens the convective velocity field. Despite this reduction in flow strength, the thermal field shown in (Fig.4.6.b) indicates that the overall heat transfer performance remains enhanced. The isotherms become more compressed and distorted near the heated and cooled boundaries, suggesting an improved convective heat transfer rate.

This seemingly paradoxical behavior—where weaker fluid motion coincides with superior heat transfer—can be explained by the substantial increase in the nanofluid's thermal conductivity. The enhanced conductive properties of SWCNTs offset the adverse impact of elevated viscosity, thereby maintaining efficient heat diffusion within the cavity.

Consequently, while excessive nanoparticle loading may impede flow development due to increased viscous resistance, the overall thermal performance remains favorable owing to the dominant contribution of enhanced thermal conductivity.

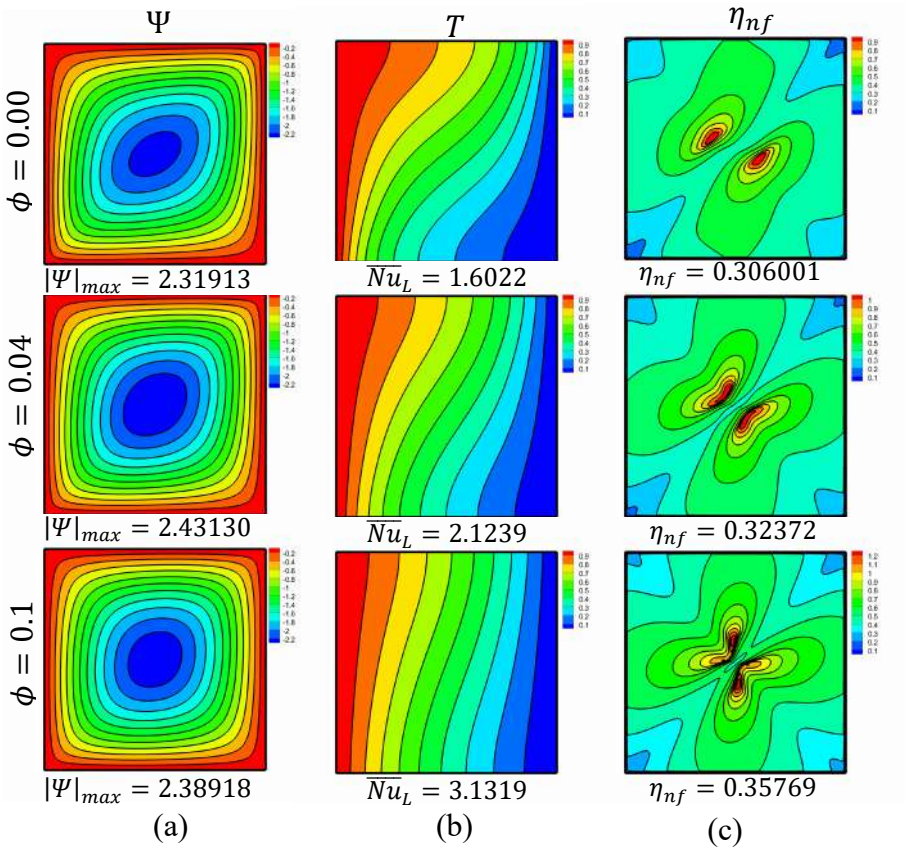



*Figure 4.6 effect of varying the concentration of SWCNTs nanoparticles on the streamlines (6a), isotherms (6b) and the apparent viscosity (6c) with the following parameters* $R_T = 200, Ha = 2, G = 0.5, n = 0, \gamma = 0°, E = 0.6, s = 0.01$ *and* $a = 2$

Figures (4.7-4.10) investigate the influence of the rheological parameters of the Carreau–Yasuda model on flow dynamics and heat transfer characteristics for $R_T = 200, G = 0.5, \gamma = 0°$ and $\phi = 0.05$.

Figure 4.7 specifically illustrates the effect of the power-law index (n) on the fluid dynamics (Fig.4.7.a), the convection strength (Fig.4.7b), and the apparent viscosity (Fig.4.7.c) at $E=0.6, s=0.01,$ and $a=2$. for various Hartmann numbers $(Ha)$ 0, 2, 4, 6, 8 and 10.

It is evident that increasing the power-law index from $n$ = 0.2 (strongly shear-thinning behavior) to n = 1.0 (Newtonian behavior) results in a noticeable reduction in flow intensity, as reflected by the decreasing magnitude of the stream function in (Fig. 4.7 a). This reduction can be attributed to the weakening of shear-thinning effects at higher $n$ values, where the apparent viscosity of the fluid remains relatively high even under shear .Consequently, the circulation patterns become weaker, and the buoyancy-driven flow is suppressed. Correspondingly, (Fig.4.7 b) shows a decline in convective strength with increasing $n$ underscoring the strong coupling between the fluid's rheological behavior and buoyancy-induced motion.

As $n$ increases, the attenuation of shear-thinning effects produces a thickening response, which elevates the apparent viscosity $\eta_{nf}$. This behavior is quantitatively confirmed in Fig.4.7.c, where higher $n$ values correspond to visibly larger viscosity magnitudes. Interestingly, the sensitivity of $(\eta_{nf})$ to $n$ is more pronounced at lower Hartmann numbers (i.e., $Ha = 0$ or 2), where both flow and thermal variations are more responsive to rheological changes. In the absence or under weak magnetic fields, the fluid's non-Newtonian nature is fully expressed, strongly influencing both flow structure and heat transfer mechanisms.

At higher Hartmann numbers, however, the influence of the magnetic field becomes dominant. The Lorentz force increasingly counteracts fluid motion, suppressing the impact of shear-dependent viscosity. This magnetic damping effect leads to a noticeable flattening of the curves in (Fig.4.7.a) and (fig.4.7.c), indicating that at strong magnetic field intensities, the role of shear-thinning behavior in governing the system's dynamics becomes substantially diminished.

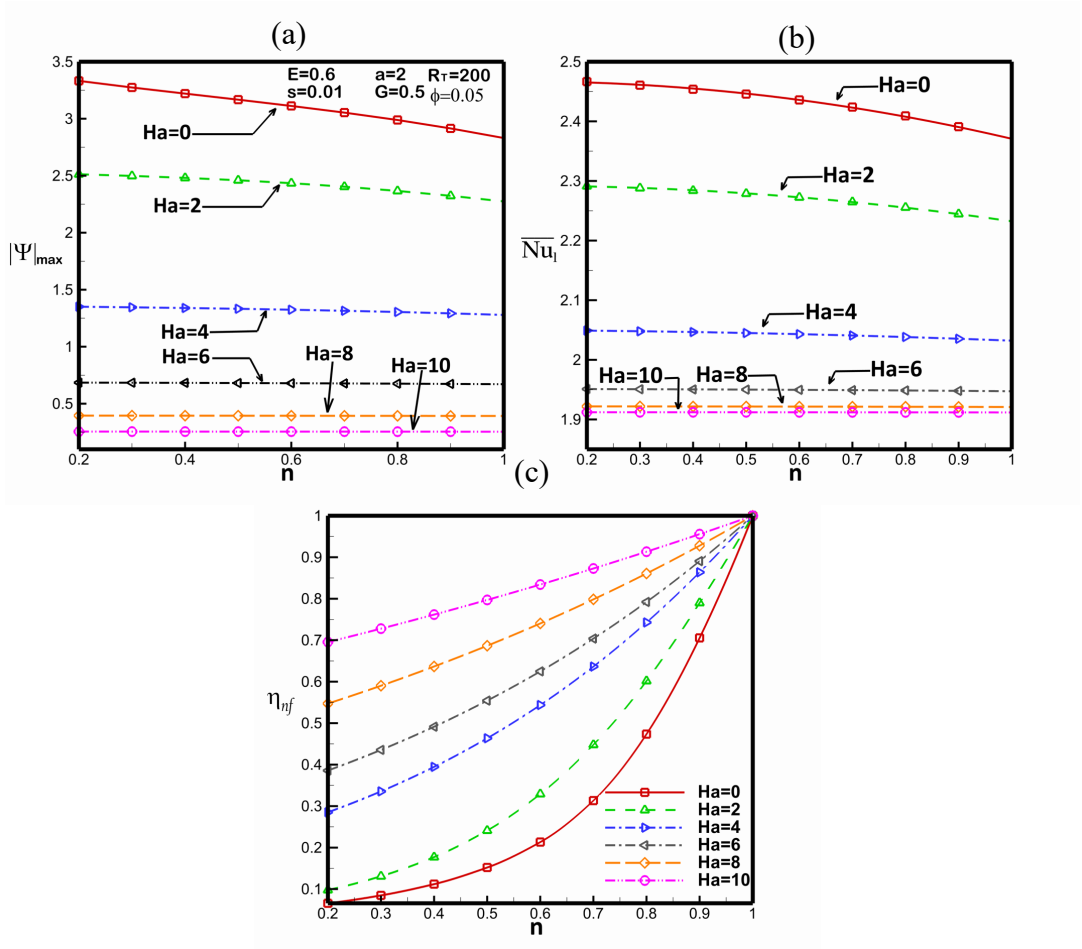



*Figure 4.7 variation of stream function at the center* $|\Psi|_{max}$ *(7a) ,the maximum average Nusselt number* $\overline{Nu_L}$*(7b), apparent viscosity* $\eta_{nf}$*(7c) versus n for various values of Ha, with* $R_T = 200, G = 0.5\ \phi = 0.05, \gamma = 0°, E = 0.6, s = 0.01$ *and* $a = 2$

Figure 4.8 illustrates the influence of the time constant parameter (E) on the flow dynamics and heat transfer characteristics for $n=0.6, s=0.01$ and $a=2$ .Unlike the power-law index which primarily governs the degree of shear-thinning, the time constant E regulates the fluid's relaxation behavior under shear deformation. As depicted in Figure 4.8, increasing $E$ from 0 to 100 initially leads to a marked enhancement in both the stream function magnitude $|\Psi|_{max}$ and convection heat transfer rate $\overline{Nu_l}$ within the range $0 \le E \le 20$ , This trend indicates a reduction in the fluid's resistance to deformation, facilitating stronger convective circulation and thereby improving heat transfer performance.

Beyond this range, however, the rate of improvement diminishes, and the curves corresponding to all Hartmann numbers (Ha) begin to level off, revealing a saturation effect. The rise in E is also accompanied by a noticeable reduction in the apparent viscosity ( $\eta_{nf}$ ), with this influence being more significant at lower magnetic field strengths. At higher Hartmann numbers (8 and 10) the curves flatten, indicating that as Ha increases the dominance of the Lorentz force suppresses the influence of shear-dependent viscosity.

As the magnetic field strength grows, the Lorentz force increasingly counteracts buoyancy-driven motion, leading to a general decline in both the average Nusselt number and stream function magnitude for a given E. This confirms that stronger magnetic fields inhibit natural convection by damping fluid motion and weakening thermal circulation.

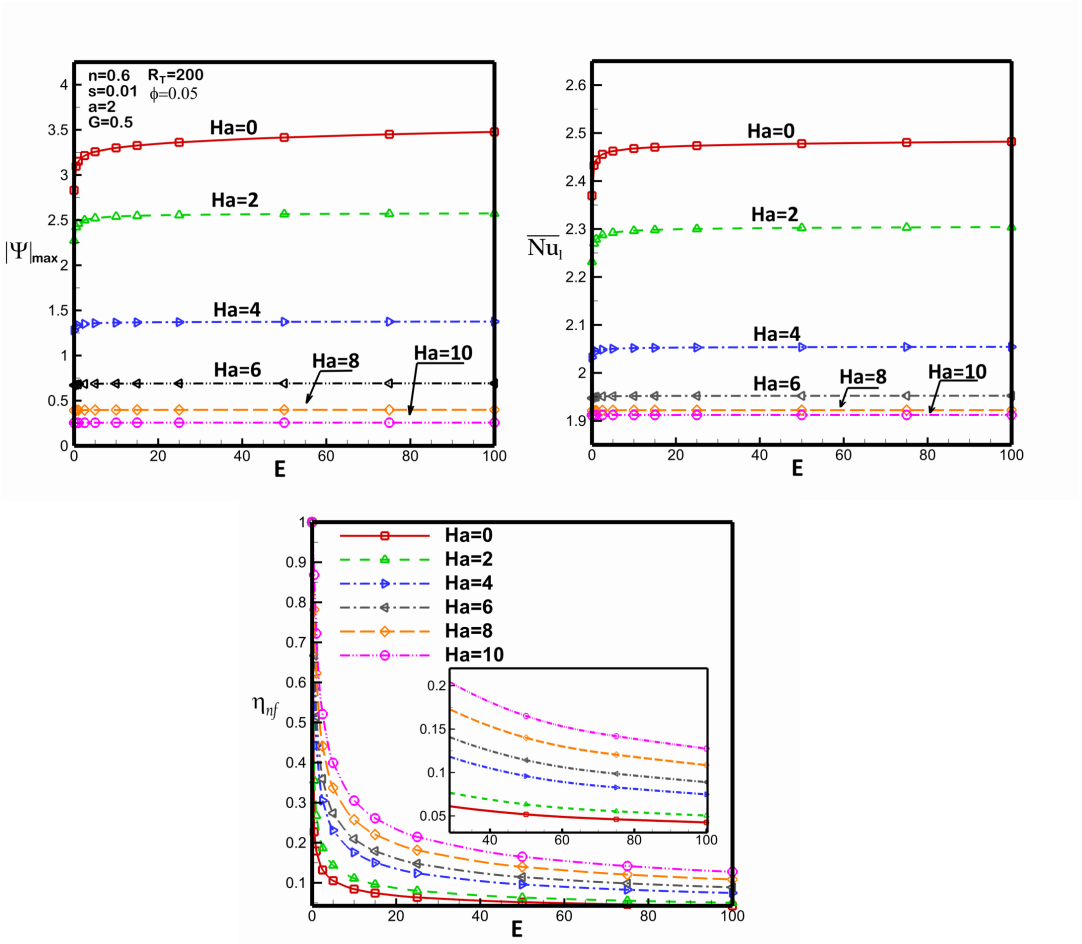



*Figure 4.8 relationship between the time constant parameter E and of stream function at the center $|\Psi|_{max}$ (8a) ,the maximum average of Nusselt number $\overline{Nu_l}$ (8b), and the apparent viscosity (8c) for various Hartmann numbers (Ha) at $R_T = 200, G = 0.5\ \phi = 0.05, \gamma = 0°, n = 0.6, s = 0.01$ and $a = 2$.*

Figure 4.9 presents the variation of the maximum absolute stream function $|\Psi|_{max}$, the average Nusselt number $\overline{Nu_L}$, and the apparent viscosity $\eta_{nf}$ with the dimensionless Carreau–Yasuda model parameter ($a$) for different Hartmann numbers, at $E=0.6, s=0.01$ and $n=0.6$. It is observed that as the parameter ($a$) increases to approximately $a=0.6$, there is a pronounced rise in the effective viscosity, followed by a gradual stabilization as (a) continues to increase. This behavior adversely affects both the flow intensity and free convection within the cavity, particularly at lower Hartmann numbers.

From a physical perspective, the Carreau–Yasuda parameter (a) dictates the rate of transition from the zero-shear (Newtonian) region to the shear-thinning regime. Higher values of (a) correspond to a

slower transition, maintaining elevated viscosity levels even under significant shear. This increased viscosity enhances the fluid's resistance to motion thereby reducing momentum transport and weakening convective heat transfer.

As the Hartmann number increases, the influence of the parameter (a) on both the flow structure and heat transfer becomes progressively less significant. The magnetic field, through the Lorentz force, increasingly dominates the flow dynamics, diminishing the sensitivity of the system to rheological variations. These results are consistent with the previously discussed trends for the parameters $n$ and $E$,confirming the interplay between magnetic damping and non-Newtonian rheological effects in governing convection behavior.

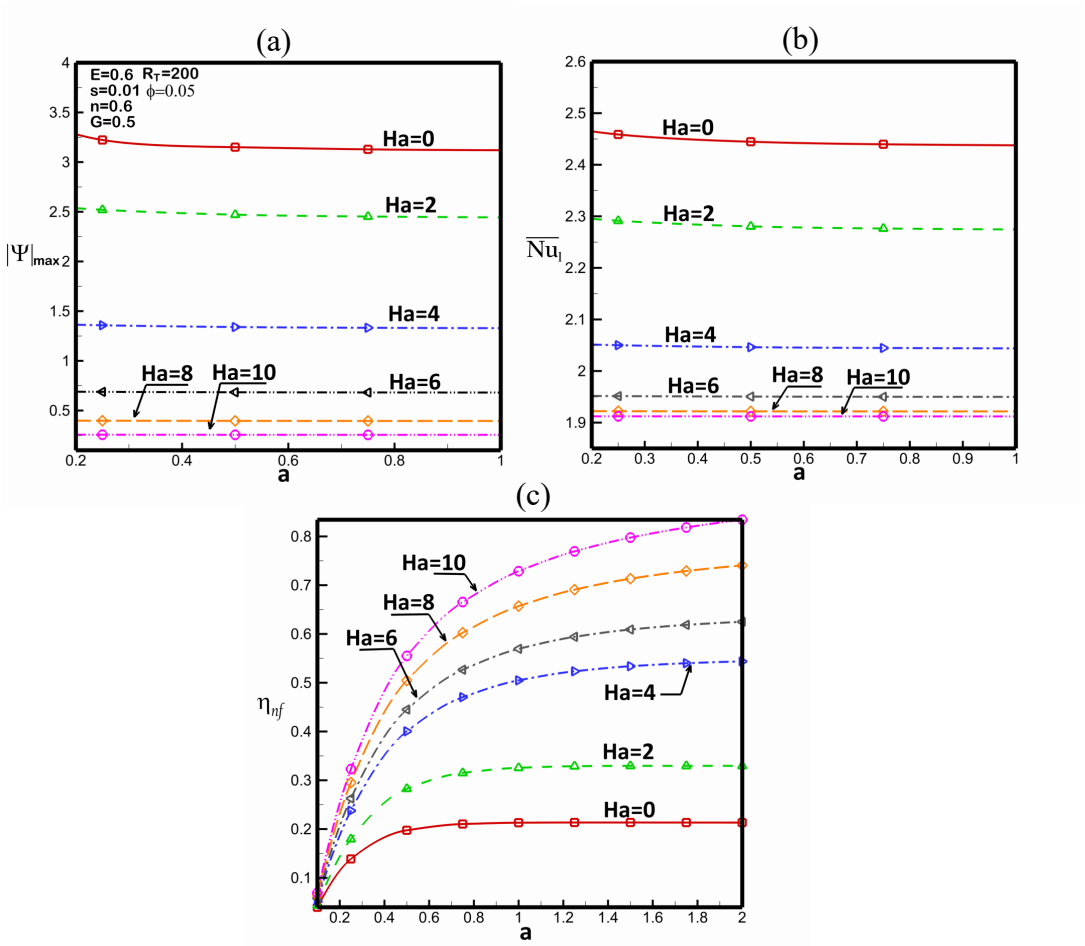



*Figure 4.9 Variation of stream function at the center $|\Psi|_{max}$ (09a), the maximum average Nusselt number $\overline{Nu_L}$(09b), apparent viscosity $\eta_{nf}$(09c) versus the parameter (a) for various values of $Ha$ at $R_T$ = 200, $\phi$=0.05, $s = 0.01$, $E = 0.6$ and $n = 0.6$.*

This section investigates the influence of the viscosity ratio parameter ( $s$ ) on the flow dynamics and convective heat transfer characteristics. As illustrated in Figure 4.10 a decrease in the viscosity ratio from $s = 1$ (Newtonian behavior) to $s = 0.2$ (shear thinning behavior) leads to a notable enhancement in convective heat transfer across all Hartmann numbers. This improvement is evidenced by the increase

in the average Nusselt number ( $\overline{Nu_L}$ ), indicating that lower viscosity ratios facilitate stronger convective currents and improved thermal performance.

However, for a fixed value of (s) , an increase in magnetic field intensity results in a reduction in both the average Nusselt number $\overline{Nu_L}$ and the maximum absolute stream function $|\Psi|_{max}$, This decline signifies a suppression of fluid motion and convective transport due to the intensification of the Lorentz force, which acts as a resistive force opposing the buoyancy-driven circulation within the cavity.

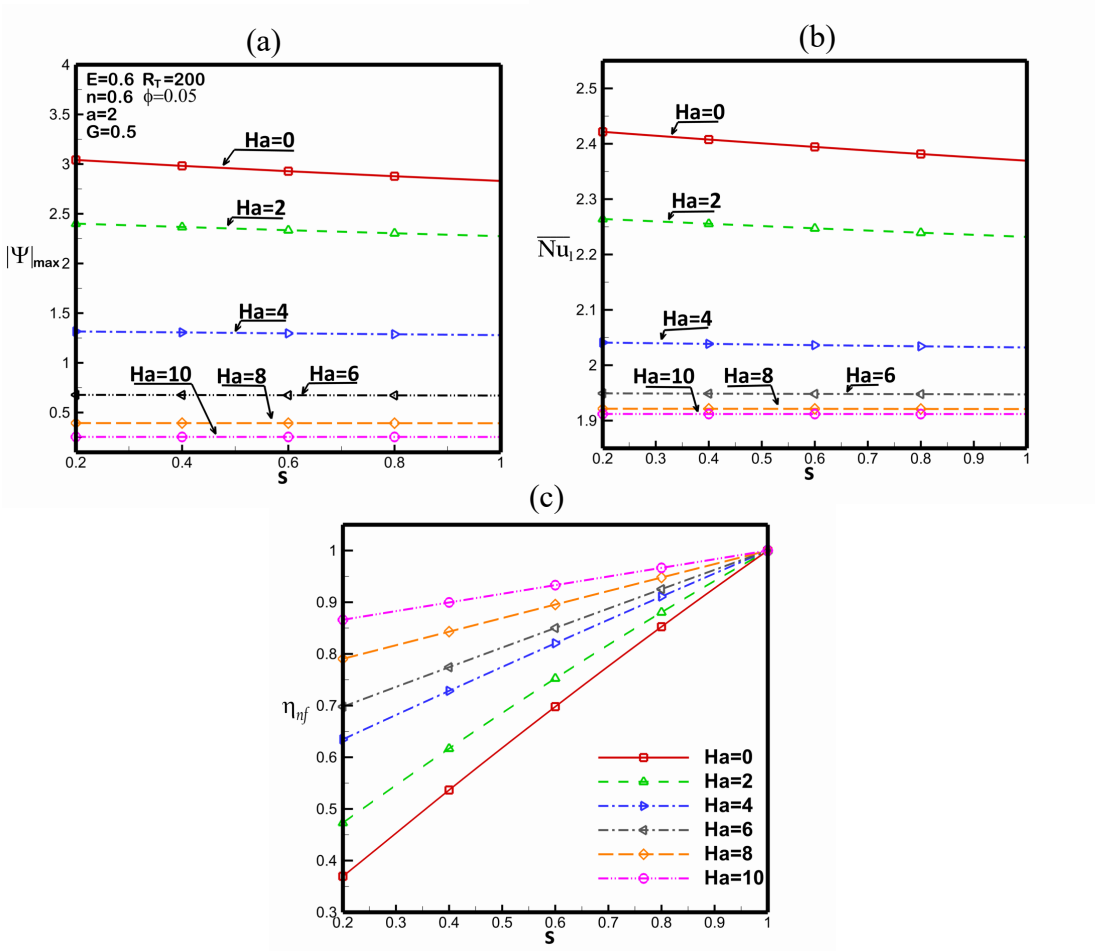



*Figure 4.10. variation of stream function at the center* $|\Psi|_{max}$ *(10a) ,the maximum average Nusselt number* $\overline{Nu_L}$*(10b), apparent viscosity* $\eta_{nf}$*(10c) versus the parameter (s) for various values of* $Ha$ *at* $R_T = 200, G = 0.5\ \phi = 0.05, \gamma = 0°, E = 0.6, s = 0.01$ *and* $a = 2.$

*nd* $a = 2.$

These collective results presented in Figures 4.7-4.10 highlight the intricate interplay between the nanofluid's rheological parameters and the applied magnetic field. While shear-thinning behavior generally enhances convective heat transfer by reducing effective viscosity and promoting fluid mobility, the dominance of the Lorentz force under strong magnetic fields counteracts these beneficial effects. This combined influence of magnetic damping and non-Newtonian behavior is consistent with the observations reported by Afsana et al.(Afsana et al., 2021).

Figure 4.11 illustrates the variation of $|\Psi|_{max}$, $\overline{Nu_l}$ and $\eta_{nf}$ with respect to inertial parameter (G) for different Hartmann numbers ( $Ha$ ) at $R_T = 200, n = 0.6, \phi = 0.05, \gamma = 0°, E = 0.6, s = 0.01$ and $a = 2$ . The combined influence of $G$ and $Ha$ exhibits a pronounced effect on both the flow dynamics and heat transfer characteristics. For a fixed $Ha$, increasing the inertial parameter $G$ leads to a reduction in both the flow intensity and convective strength, as evidenced by the decrease in $|\Psi|_{max}$ and $\overline{Nu_l}$. This decline signifies a gradual transition from a convection-dominated regime toward conduction-dominated heat transfer.

At lower magnetic field intensities (i.e., $Ha \leq 2$), a sharp drop in nanofluid flow intensity is observed as G increases up to approximately 2.This behavior is primarily attributed to the enhanced inertial resistance, which impedes fluid motion and weakens buoyancy-induced circulation.

However, as the magnetic field strength increases further, particularly for Ha ≥ 8. the combined effects of inertia and magnetic damping become dominant. Under these conditions, the nanofluid flow becomes nearly stagnant, and heat transfer occurs predominantly through conduction rather than convection. This transition highlights the strong suppressive influence of the Lorentz force and inertial effects on convective transport. The present findings regarding the combined damping effects of Ha and G on flow and convection intensity are consistent with those reported by (Rebhi et al., 2021). Furthermore, (Figure 4.11 c) depicts the intricate interaction between these two parameters on the apparent viscosity ( $\eta_{nf}$ ). As $Ha$ increases from 0 to 6, multiple intersections appear among the viscosity curves, indicating a complex coupling between magnetic and inertial influences on the non-Newtonian nanofluid behavior. However, at higher Hartmann numbers (Ha = 8–10), the magnetic field suppresses the shear-thinning characteristics, rendering the fluid less sensitive to inertial variations and eventually eliminating these intersections.

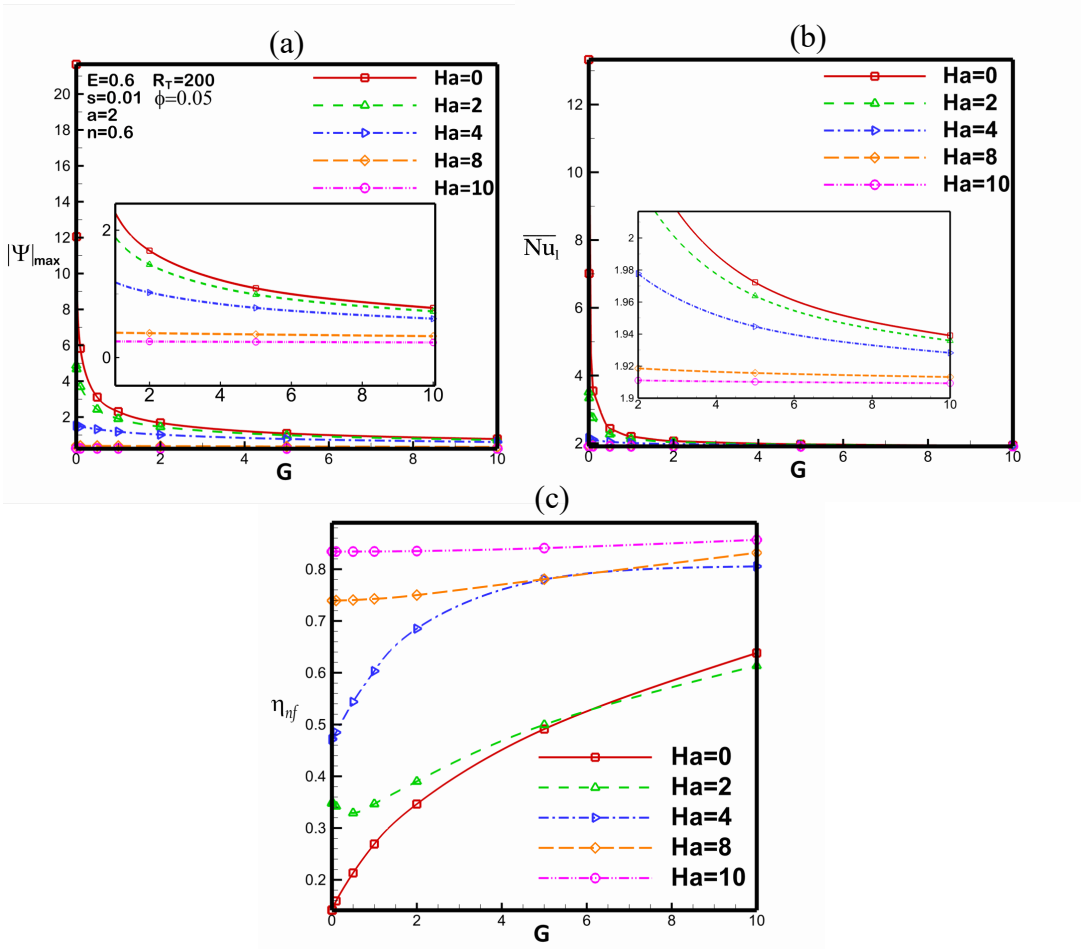



*Figure 4.11. . variation of stream function at the center* $|\Psi|_{max}$ *(11a) ,the maximum average Nusselt number* $\overline{Nu_L}$*(11b), apparent viscosity* $\eta_{nf}$*(11c) versus the parameter (G) for various values of Ha at* $R_T = 200, n = 0.6\ \phi = 0.05, \gamma = 0°, E = 0.6, s = 0.01$ *and* $a = 2$.

Figure 4.12 illustrates the variations of the maximum stream function $|\Psi|_{max}$ average Nusselt number $\overline{Nu_L}$ and apparent viscosity $\eta_{nf}$ with respect to the nanoparticle volume fraction $\phi$ for different Hartmann numbers *Ha* under fixed parameters of $R_T = 200$ , $G = 0.5$ , $n = 0.6, \gamma = 0°, E = 0.6, s = 0.01$ and $a = 2$. For any given concentration of SWCNTs $\phi$ , an increase in the Hartmann number leads to a noticeable reduction in both flow intensity and heat transfer rate. This decline is primarily attributed to the intensification of the Lorentz force, which impedes the motion of the conducting nanofluid and suppresses the natural convection circulation, thereby diminishing convective heat transfer efficiency.

However, for a fixed Hartmann number, the addition of SWCNT nanoparticles exhibits varying influence depending on the magnetic field intensity. At low magnetic field strengths (Ha = 0–2), increasing the nanoparticle concentration slightly affects the flow strength. In contrast, at higher Hartmann numbers, the dominant magnetic damping effect overshadows the influence of nanoparticle addition, resulting in negligible variation in flow circulation. Despite the increase in apparent viscosity

with higher SWCNT loading $\phi > 5\%$ —which generally reduces the nanofluid velocity and weakens flow intensity, the substantial enhancement in thermal conductivity due to the superior heat transport capability of SWCNTs compensates for this effect. Consequently, the overall convective heat transfer performance improved, as evidenced by the rise in the average Nusselt number $\overline{Nu_L}$ (from 1.8339 to 3.231 when the nanoparticle volume fraction increases from $\phi = 0.0$ to $\phi$=0.1).

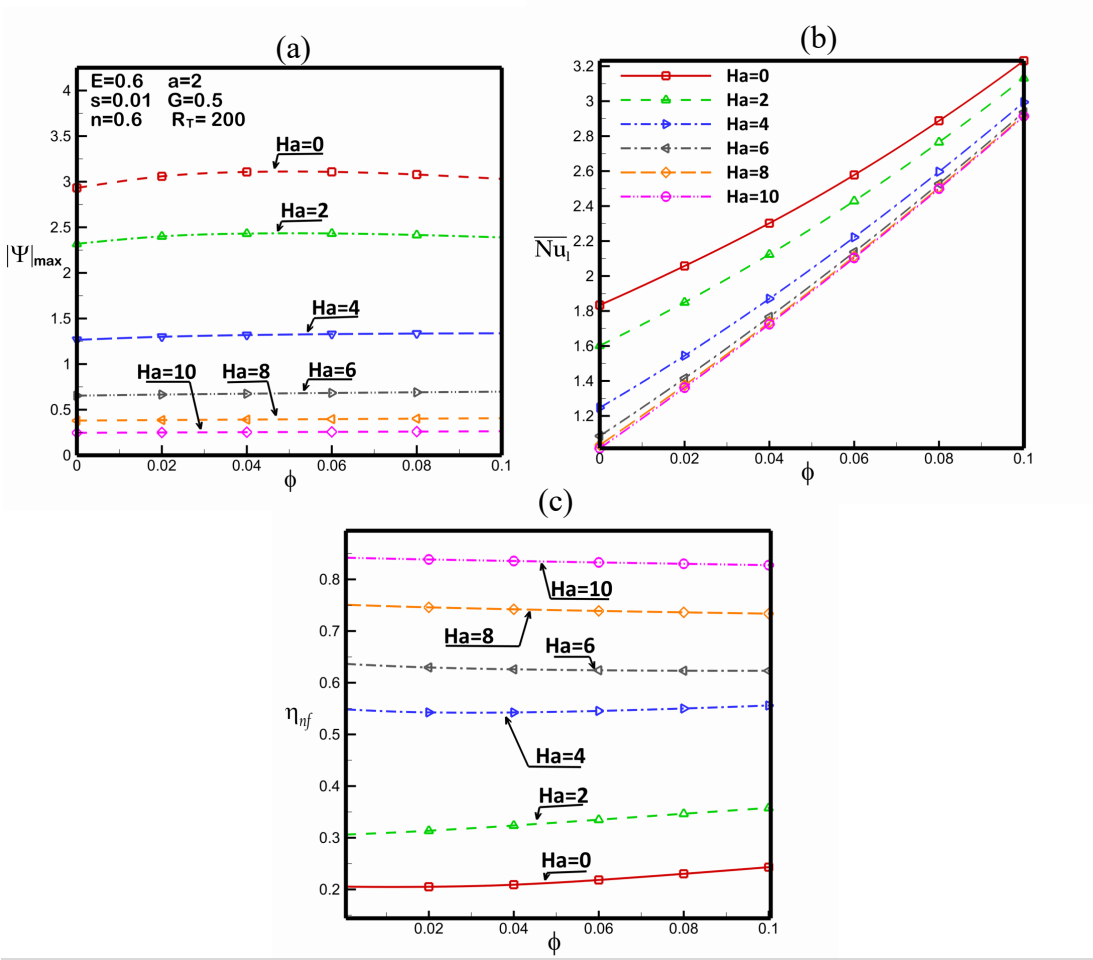



*Figure 4.12 variation of stream function at the center* $|\Psi|_{max}$ *(12a) ,the maximum average Nusselt number* $\overline{Nu_L}$*(12b), apparent viscosity* $\eta_{nf}$*(12c) versus* $\phi$ *for various values of* $Ha$ *at* $R_T = 200, G = 0.5\ n = 0.6, \gamma = 0°, E = 0.6, s = 0.01$ *and* $a = 2.$

Figure 4.13 depicts the influence of the inclination angle $(\gamma)$ varying from $\gamma = -90°$ *to* $\gamma = 90°$ and the Hartmann number ( $Ha = 0 - 10$ ) on the flow characteristics(fig.4.13.a),convection rate (fig.4.13.b) and apparent viscosity (fig.4.13.c) for the parameters $R_T = 200,\ G = 0.5\ , \phi = 0.05, n = 0.6, E = 0.6, s = 0.01$ and $a = 2.$

It is observed that increasing the Hartmann number $Ha$ results in a noticeable reduction in both the stream function magnitude and convection strength over the entire range of inclination angles. This

reduction stems from the Lorentz force, which acts as a magnetic damping mechanism that suppresses fluid motion and weakens convective heat transfer.

The analysis reveals an optimal inclination angle of approximately, $\gamma = 30°$, where both the stream function and heat transfer attain their maximum values in the absence of magnetic effects $(Ha = 0)$. This inclination corresponds to the most favorable alignment of buoyancy forces, leading to the formation of well-developed convective cell and enhanced thermal circulation. As the magnetic field intensity increases, however, this optimal angle gradually shifts toward smaller values, eventually reaching( $\gamma = 0°$ ) when $Ha = 10$ .This behavior indicates that the magnetic field mitigates the influence of inclination by stabilizing the flow structure and flattening convection patterns.

Moreover, the Nusselt number distribution shows that thermal performance is maximized within the intermediate range $-30° < \gamma < 60°$, where convective motion remains sufficiently strong despite moderate magnetic damping .Outside this range, particularly near the extreme inclinations $\gamma = \pm 90°$, heat transfer decreases sharply. At these orientations, gravity acts parallel to the heated or cooled vertical boundaries, thereby minimizing buoyancy-driven motion and resulting in negligible stream function values( $|\Psi|_{max} = 0$ ) Consequently, heat transfer in these cases occurs predominantly through conduction rather than convection.

As shown in (Fig 4.13 c),the apparent viscosity $\eta_{nf}$ decreases significantly as the Hartmann number decreases, particularly within the intermediate inclination range (i.e., $-30° < \gamma < 60°$ ) where shear rates are elevated. This reduction in effective viscosity is a direct manifestation of shear-thinning behavior, which enhances fluid mobility. Conversely, as the magnetic field strength increases, the velocity gradients are dampened, lowering the local shear rate and thereby increasing the apparent viscosity. This magnetic-induced viscosity augmentation intensifies flow resistance, further suppressing convective circulation at high Hartmann numbers

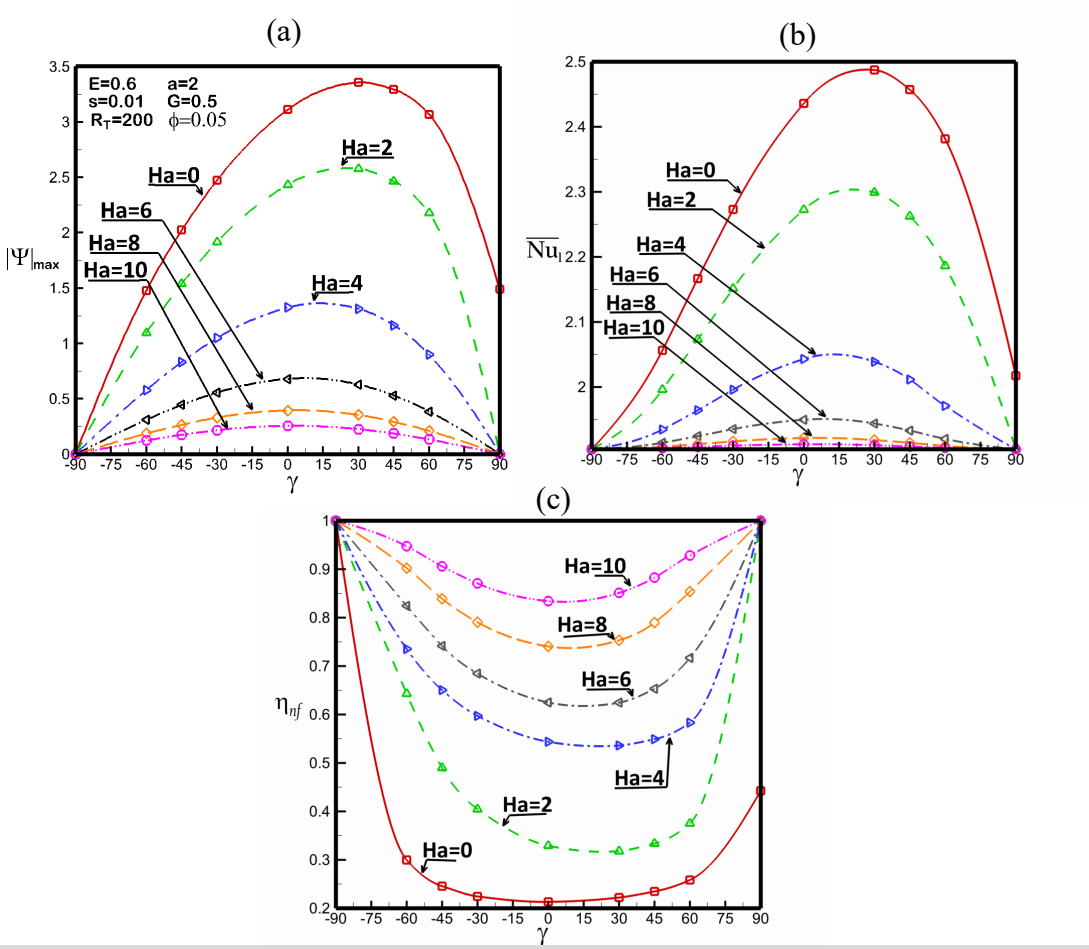



*Figure 4.13 Variation of stream function at the center $|\Psi|_{max}$ (13a), the maximum average Nusselt number $\overline{Nu_L}$(13b), apparent viscosity $\eta_{nf}$(13c) versus $\gamma$for various values of $Ha$ at $R_T = 200, G = 0.5\ \phi = 0.05, n = 0.6, E = 0.6, s = 0.01$ and $a = 2$.*

Figure 4.14 presents a comparative assessment of the thermal and flow behavior of two—( $Al_2O_3$–water) and (SWCNT–water)—as functions of the power-law index $n$ and various Hartmann numbers $Ha$, under the fixed conditions $R_T = 200, G = 0.5 \phi = 0.05, \gamma = 0°, E = 0.6, s = 0.01$ and $a = 2$. For any given value of n, an increase in Ha from 0 to 10 results in a marked decrease in both the maximum stream function magnitude $|\Psi|_{max}$ and the average Nusselt number. This trend reflects the damping influence of the Lorentz force, which progressively suppresses fluid motion and convective heat transfer in both nanofluids as the magnetic field strength intensifies.

Notably, the SWCNT–water nanofluid consistently exhibits superior thermal and hydrodynamic performance compared to the $Al_2O_3$–water nanofluid across the entire range of Ha and n values. This enhancement is primarily attributed to its intrinsically lower apparent viscosity and higher thermal conductivity, which promote more effective convective circulation and heat transport.

Furthermore, as the power-law index ( $n$ ) decreases from $n = 1$ to $n = 0.2$, the apparent viscosity ( $\eta_{nf}$ ) of both nanofluids declines, leading to an enhancement in flow intensity and convective efficiency.

This observation underscores the advantage of shear-thinning non-Newtonian nanofluids, which exhibit superior flowability and heat transfer characteristics compared to Newtonian counterparts under equivalent conditions.

The superior behavior of the SWCNT–water nanofluid is further corroborated by its consistently lower apparent viscosity relative to the $Al_2O_3$–water nanofluid. This reduced viscous resistance facilitates stronger convective currents and more efficient heat transport, highlighting the potential of SWCNT-based nanofluids for advanced thermal management applications where both enhanced heat transfer and optimized fluid dynamics are essential.

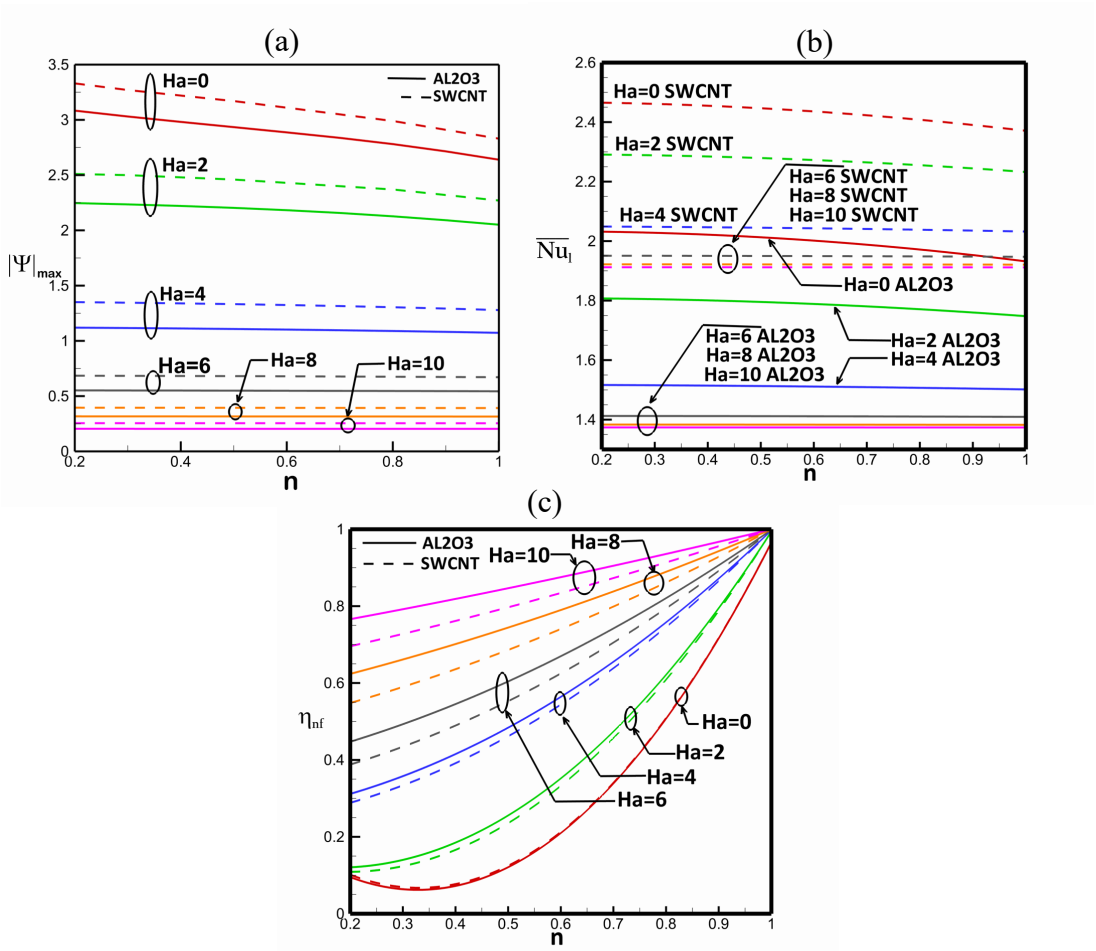



*Figure 4.14 comparison between SWCNT and $AL_2O_3$ nanoparticles on the maximum absolute stream function $|\Psi|_{max}$(14a) the average Nusselt number $\overline{Nu_l}$ (14b) and the apparent viscosity at $R_T = 200, G = 0.5\ \phi = 0.05, \gamma = 0°, E = 0.6, s = 0.01, and\ a = 2$*

## 4.2. **Second part: The Non-Newtonian hybrid nanofluid (Cu-Al2O3- water)**

A grid independence test was conducted to guarantee the correctness and numerical stability of the current simulation. The investigation included altering the grid size from 5 × 5 to 200 × 200, with all parameters held constant. Figure 4.15 depicts the relationship between the average Nusselt number (

$\overline{Nu_L}$) and the maximum stream function ( $|\Psi|_{max}$) in relation to grid size. Both numbers initially show significant changes with increasing grid resolution; however, above a grid size of around 100 × 100, the results become practically constant, suggesting grid convergence. A uniform grid of 100 × 100 was used for all future calculations, since it offers an adequate balance between computational expense and solution precision.

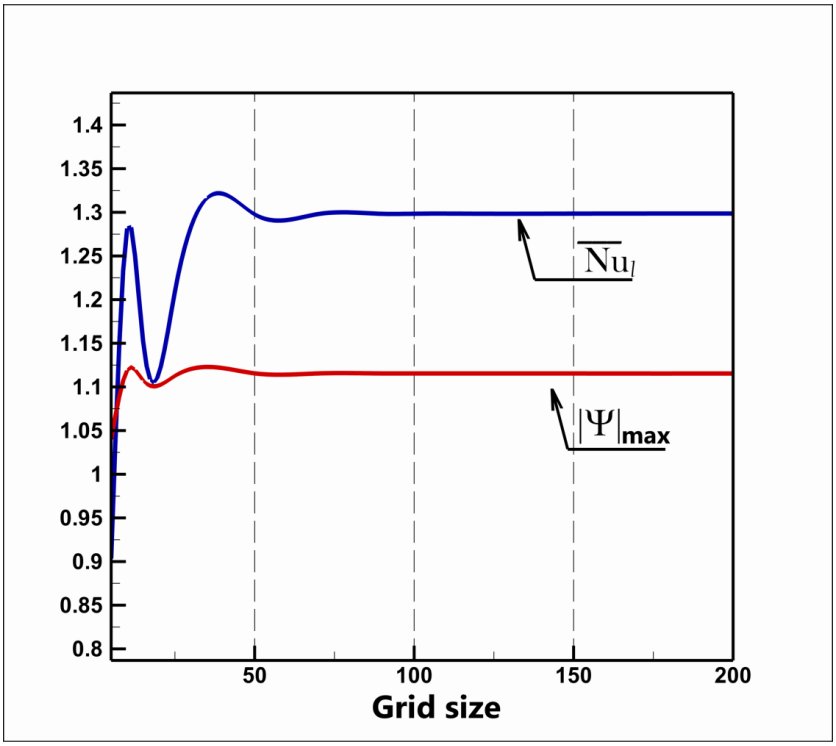



*Figure 4.15:Variation of the average Nusselt number and maximum stream function with grid size for the grid independence test*

To rigorously validate the present methodology and numerical code, a comprehensive two-pronged approach was adopted. First, the computed average Nusselt number Nu was benchmarked against established and published data from the peer-reviewed literature (as detailed in Table 4-5). This comparative analysis serves as a primary validation step to confirm the reliability of the calculations.

*Table 4-5: Comparison of $\overline{Nu}$ with some previous numerical results*

| Author | $\overline{Nu}$ | |
|---|---|---|
| | $R_T = 100$ | $R_T = 1000$ |
| (Walker & Homsy, 1978) | 3.097 | 12.960 |
| (Gross et al., 1986) | 3.141 | 13.448 |
| (Lauriat & Prasad, 1989) | 3.09 | 13.41 |
| (Manole, 1992) | 3.118 | 13.637 |
| (Baytaş, 2000) | 3.160 | 14.060 |
| (Sheremet et al., 2017) | 3.104 | 13.839 |
| Present study | 3.1211 | 13.585 |

Second, the resulting streamline trajectories were compared with the work presented by Revnic et al., 2024.The visual and quantitative congruence observed between the two datasets demonstrates a high degree of fidelity and robust agreement in the numerical solution, thereby affirming the overall accuracy and trustworthiness of the numerical model.

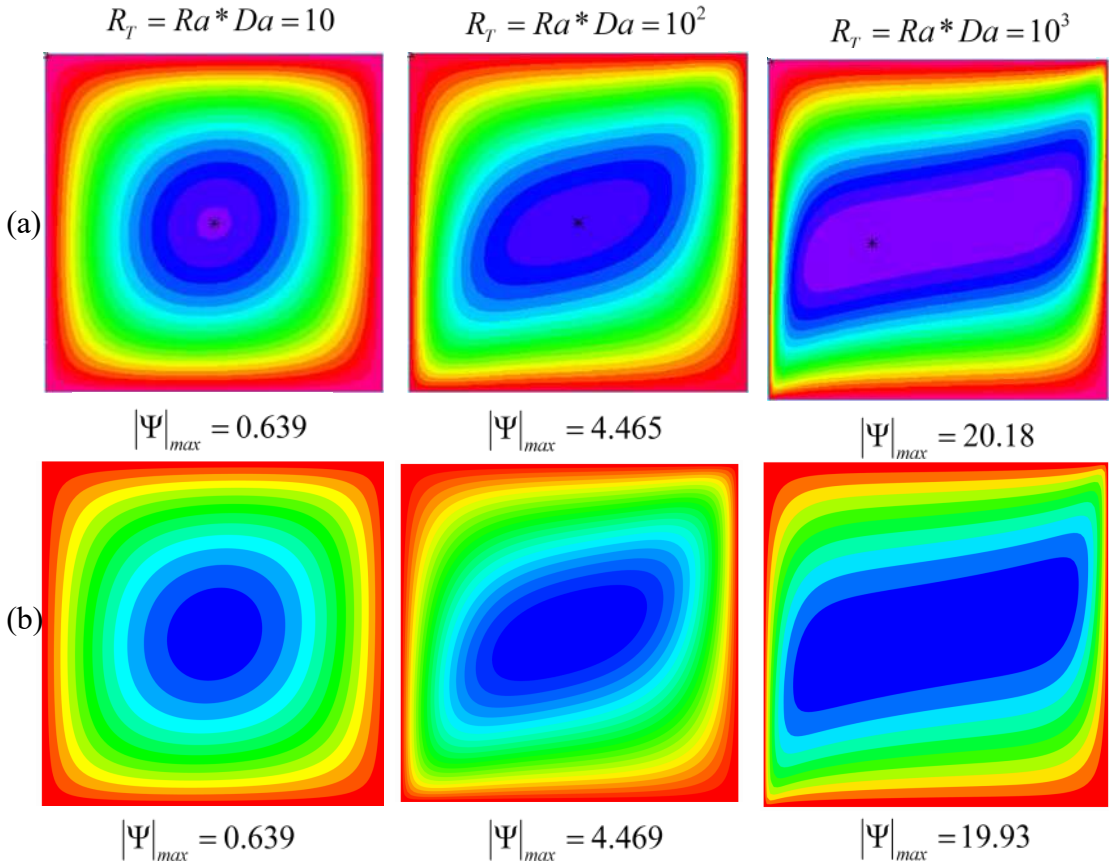



*Figure 4.16 :Comparison in terms of streamline for different $R_T$ values between the current results (b) and those of (Revnic et al., 2024) (a) at $(\phi)_{hnf}$=0.04 , G=0, Ha=0, n=1*

Figure 4.17 depicts the influence of the power-law index ($n$) on flow circulation Ψ (a), temperature field $T$ (b), and the rheological behavior of the hybrid nanofluid $\eta_{hnf}$ (c). For the Newtonian case (n=1), the fluid reaches its maximal apparent viscosity ($\eta_{hnf} = 1.107$), which remains uniform throughout the cavity, independent of the local shear rate. Under these conditions, the convective circulation remains relatively weak $|\Psi|_{max} = 1.09877$), and the related isotherms show mild distortion, with limited convective contribution ($\overline{Nu}_L = 1.2919$).

As the power-law index drops ($n = 0.6$), shear-thinning effects become noticeable. The apparent viscosity reduces due to decreasing viscous resistance. As a result, buoyancy-driven motion is reinforced, which leads to a stronger convective cell. This is indicated by the increase in the maximum stream function value from $|\Psi|_{max} = 1.09877$ to 1.12854 and enhanced heat transfer, as confirmed by

the increased curvature of the isotherms (b); therefore, the average Nusselt number rises to ($\overline{Nu_L} = 13032$).

A further reduction to $n = 0.2$ amplifies the shear-thinning effect, maximizing the observed trends. The hybrid nanofluid attains its lowest apparent viscosity of $\eta_{hnf} = 0.312327$, resulting in the generation of the highest circulation ($|\Psi|_{max} = 1.14611$). The isotherms exhibit more extreme distortion, and the Nusselt number reaches its peak $\overline{Nu_L} = 1.3094$. Overall, the results indicate that decreasing the power-law index intensifies shear-thinning behavior, consequently reducing viscosity, promoting stronger flow circulation, and greatly increasing natural convection performance.

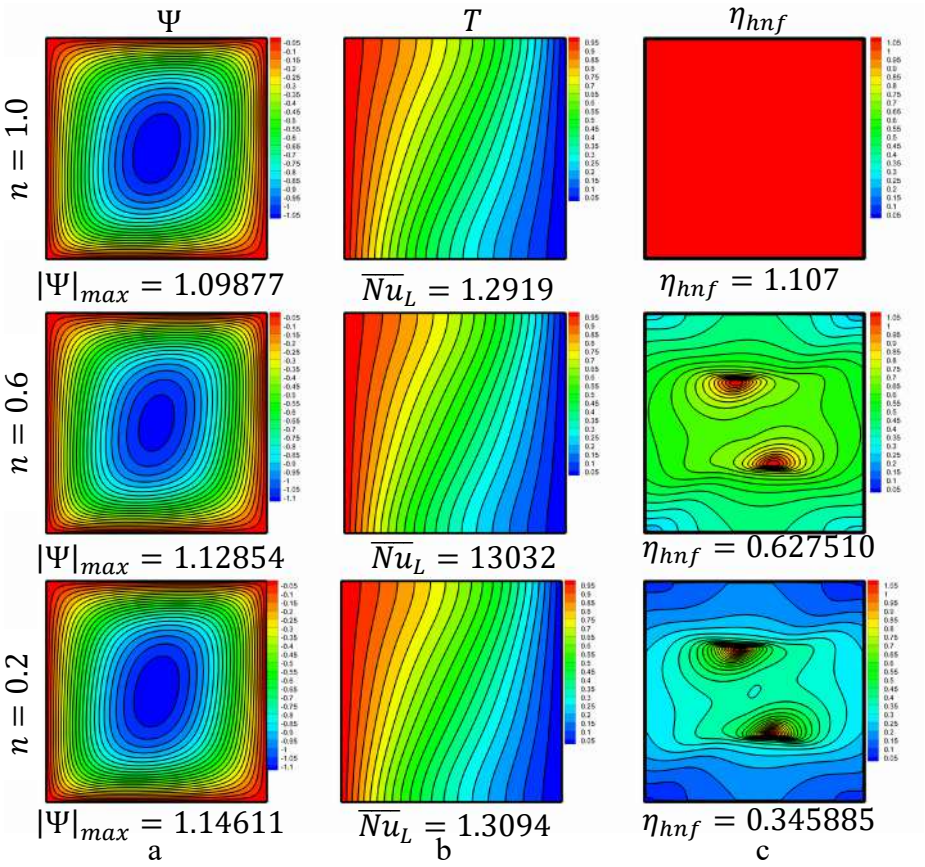



*Figure 4.17 streamlines (a) , isotherms (b) , and (c) apparent viscosity contours at various values of power-law index (n) at $R_T$=200,G=0.5,Ha=4,a=2,E=0.6 ,s=0.01 and $\phi_{hnf} = 0.04$*

Figure 4.18 depicts the influence of the Hartmann number (Ha) on the streamline Ψ (a), isotherm $T$ (b), and apparent viscosity $\eta_{hnf}$ (c). In the absence of a magnetic field ($Ha = 0$), buoyancy forces dominate, leading to the formation of a circular convection cell within the cavity characterized by a maximum circulation strength of $|\Psi|_{max} = 2.65836$.The thermal distribution displays notably distorted isotherms, and the average Nusselt number attains $\overline{Nu_L} = 1.7783$, showing the dominance of convective heat transfer mechanisms.

With the application of a magnetic field, the Lorentz force counteracts the buoyancy force, thereby leading to a gradual suppression of circulation. At Ha=5, the stream function diminishes to $|\Psi|_{max} = 0.787242$. This damping effect leads to a reduction in the average Nusselt number to $\overline{Nu}_L = 1.2231$, as convection diminishes and conduction gains prominence.

At Ha=10, the circulation is almost entirely suppressed, resulting in a substantial decrease in the maximum absolute value of the stream function ($|\Psi|_{max}$), to only 0.214229. This change causes the isotherms to become practically vertical and exhibit uniform distribution. Concurrently, the Nusselt number diminishes to $\overline{Nu}_L = 1.1338$, indicating a complete transition to conduction-dominated heat transfer.

These hydromagnetic changes directly alter the rheological characteristics of the shear-thinning hybrid nanofluid($Cu + Al_2O_3$) water. At Ha=0, the strong shear rate induces a drop in viscosity to $\eta_{hnf} = 0.524$. With an increase in Hartmann number and the flow diminishes, the apparent viscosity grows gradually, reaching $\eta_{hnf} = 0.864$ at Ha=5 and subsequently increasing to a high of $\eta_{hnf} = 1.031$

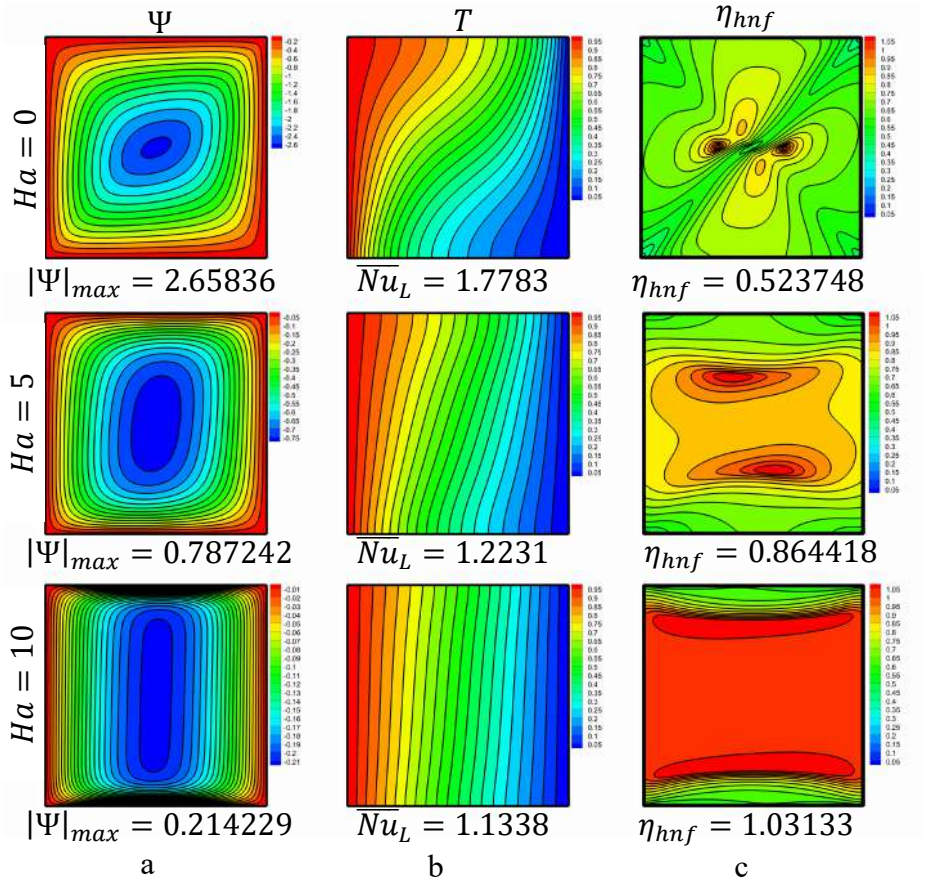



*Figure 4.18 streamlines (a) , isotherms (b) , and (c) apparent viscosity contours at various values of Hartmann numbers (Ha)at $R_T$=200,G=0.5,n=0.4,a=2,E=0.6 ,s=0.01 and $\phi_{hnf} = 0.04$*

at Ha=10. This almost twofold rise in viscosity reveals a strong relationship between magnetic damping and shear-thinning rheological characteristics, which hinders convective flow and promotes conduction.

Figure 4.19 depicts the effect of a hybrid nanoparticle ($Cu + Al_2O_3$)concentration ($\phi_{hnf}$ = 0, 0.05, and 0.10) on streamlines Ψ (a), isotherms $T$ (b), and apparent viscosity contours $\eta_{hnf}$ (c). A single circulation cell fills the cavity for all instances, although its intensity diminishes progressively with increasing $\phi_{hnf}$. The maximum stream function reduces from $|\Psi|_{max} = 1.27698$ for the base fluid to $|\Psi|_{max} = 1.10589$ at $\phi_{hnf} = 0.05$, and further to $|\Psi|_{max} = 0.9552$ at $\phi_{hnf} = 0.10$, reflecting the damping effect of higher viscous resistance. This behavior is consistent with the apparent viscosity distribution (Fig. 3c), where $\eta_{hnf}$ increases from 0.401741 for the pure fluid to 0.59136 at $\phi_{hnf} = 0.10$.

Despite the attenuation of internal circulation and the decreased distortion of isotherms, heat transfer performance demonstrates a continuous enhancement. The average Nusselt number across the hot wall increases from $\overline{Nu}_L = 1.2518$ at $\phi_{hnf} = 0$ to 1.4415 at $\phi_{hnf} = 0.10$. This seeming contradiction can be explained by the improved conductivity provided by the nanoparticles, which mitigates the adverse effects of diminished convective motion, as indicated by the reduced distortion of the isotherms. Thus, at higher $\phi_{hnf}$ values, conduction becomes more pronounced in heat transfer. This trend indicates a concurrent increase in the effective thermal conductivity $K_{hnf}$, with apparent viscosity $(\eta_{hnf})_{hnf}$ as $\phi$ increasing

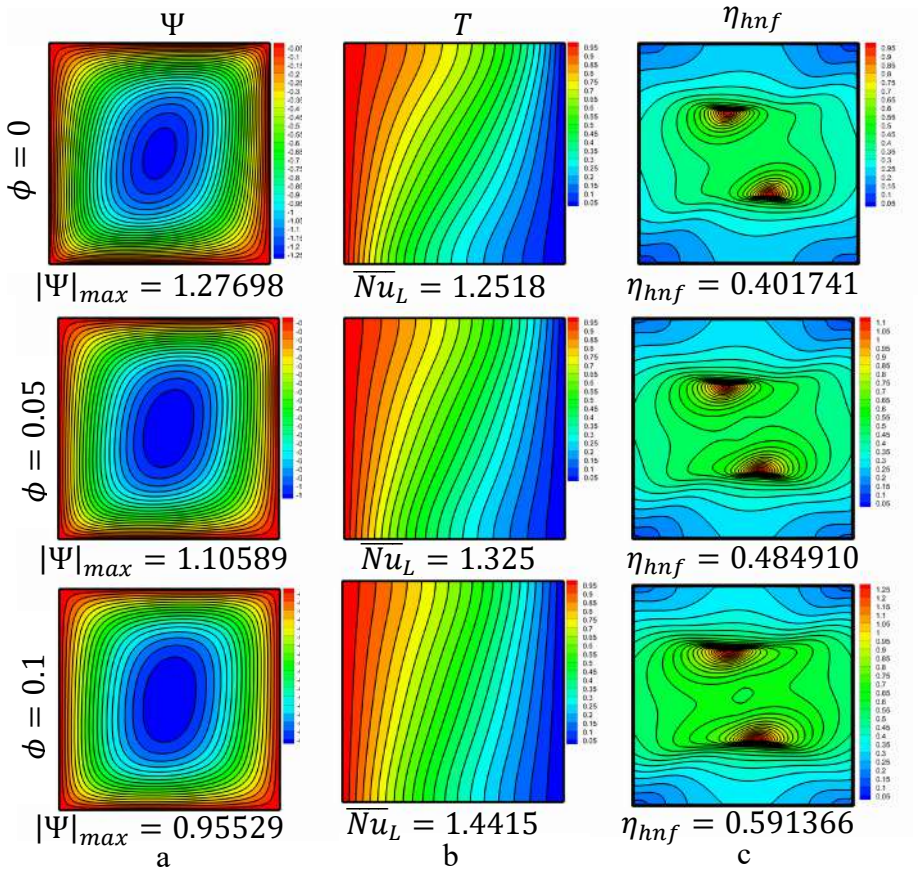



*Figure 4.19 :streamlines (a) , isotherms (b) , and (c) apparent viscosity contours at various values of nanoparticles percentage $\phi_{hnf}$ at $R_T$=200,G=0.5,n=0.4,a=2,E=0.6 ,s=0.01 and $Ha = 4$*

Figure 4.20 depicts alterations in the apparent viscosity profiles ($\eta_{hnf}$) along the mid-horizontal line (Y=0) for various values of (a) the Hartmann number Ha, (b) the inertial parameter G, and (c) the nanoparticle volume fraction $\phi_{hnf}$. In (fig 4.20-a), the absence of the magnetic field ($Ha = 0$) results in a viscosity distribution that displays two clear minima located near the cavity center and walls, corresponding to regions of high shear rate. This behavior highlights the shear-thinning behavior. With an increase in Hartmann number ($Ha$), the Lorentz force counteracts the buoyancy-driven motion, suppressing the velocity gradients and a subsequent decrease in shear rate. Moreover, at higher magnetic intensities ($Ha = 8 - 10$), the shear thinning effect gradually decreases as the viscosity profile flattens and approaches its limit (zero shear value)

Additionally, an upward trend in apparent viscosity was also observed alongside a rise in the inertial effect coefficient G (fig 4.20-b) and nano-concentration $\phi_{hnf}$ (fig 4.20-c). An increase in the inertial coefficient G leads to a rise in the hydrodynamic resistance, subsequently reducing flow velocity and shear rate, which results in a higher apparent viscosity $\eta_{hnf}$ . In addition, the influence of the nanoparticle volume fraction ($\phi_{hnf}$) further enhances the apparent viscosity $\eta_{hnf}$ . As $\phi_{hnf}$

increases from 0 to 0.1, the profile shifts upward uniformly due to enhanced internal friction and inhibits the fluid flow

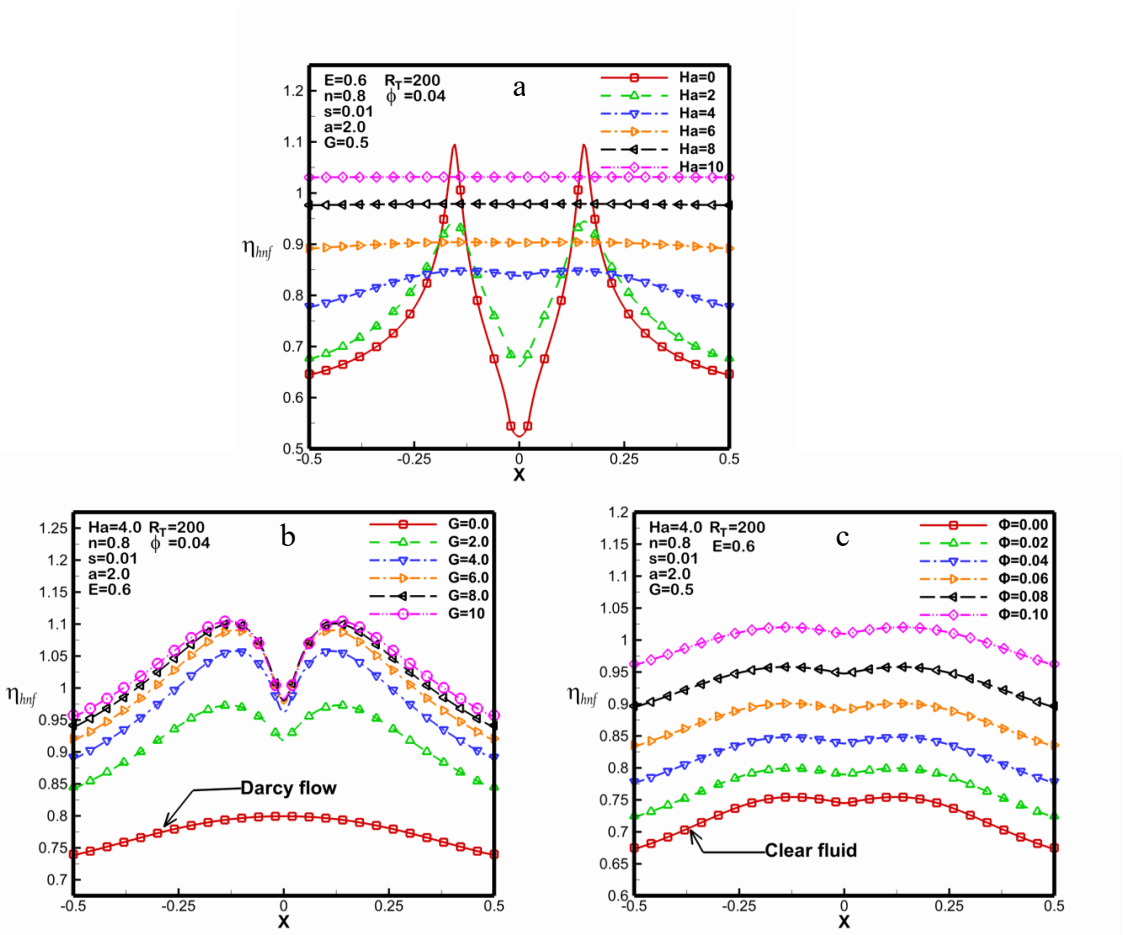



*Figure 4.20: Profiles of the apparent viscosity versus the X-axis with various value of: (a) Hartmann number, (b)inertial parameter G and (c) nanoparticle volumetric fraction, at Y=0*

Figure 4.21 displays the influence of the Carreau–Yasuda parameters ($n$, $E$, $s$, and $a$) on the apparent viscosity profile $\eta_{hnf}$ along the X axis at Y=0. Moreover, in cases of lowered $n$ ,$a$ and $s$ or increased $E$ , an increased shear-thinning effect is noticed, considerably evident at the cavity's central area and in its solid boundaries due to the higher shear rate, culminating in a significant decline in fluid viscosity.

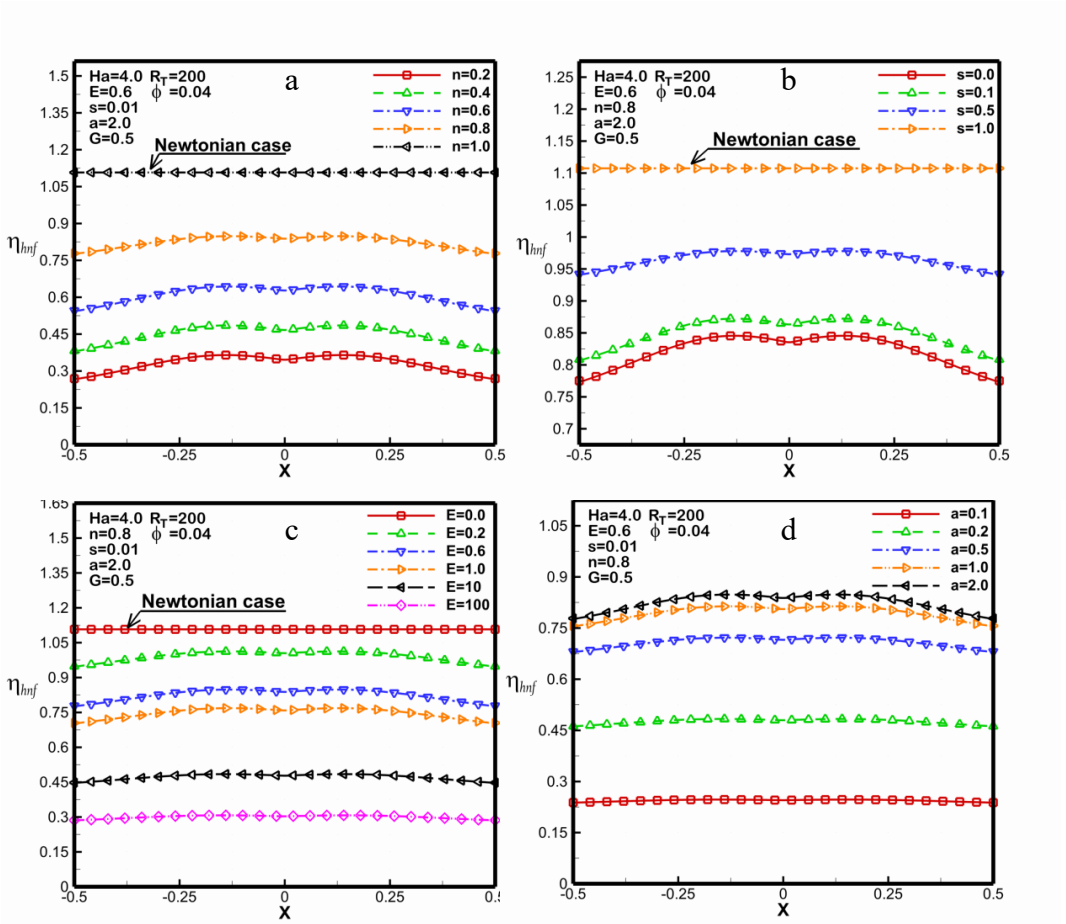



*Figure 4.21:Profiles of the apparent viscosity versus the X-axis under the influence of: (a) the power law index a , (b) time constant parameter E, (c) viscosity ratio parameter s and (d) dimensionless parameter of the Carreau-Yasuda model a, at Y=0.*

Figure 4.22 investigates the influence of both the hybrid nanofluid volume fraction ($\phi_{hnf}$) and the power-law index (n) on the natural convection behavior of (Al2O3+Cu/water) hybrid nanofluid, through the variations of the maximum stream function ($|\Psi|_{max}$), The average Nusselt number ($\overline{(Nu)}_l$), and the effective viscosity ($\eta_{hnf}$) ,at $R_T$=200,G=0.5,Ha=4,a=2,E=0.6 ,and s=0.01 Figure 1(c) shows a substantial decrease in effective viscosity as the power-law index ($n$) decreases, from 1 (Newtonian case) to approximately $\eta_{hnf} = 0.3$ at n=0.2. This rheological behavior implies a shear-thinning characteristic. The reduction in viscosity leads to lower internal resistance within the fluid which in turn makes its movement within the cavity easier.

Consequently, this enhanced fluidity is reflected in (fig 4.22-a). Where, for any given value of the fraction volume, a lower value of ($n$) , results in a higher maximum stream function ($|\Psi|_{max}$), indicating intensified internal circulation. This improvement is further reflected in the overall enhancement of convective flow, which is expressed by the increasing of the average Nusselt number $\overline{(Nu)}_l$ by 1.35% from $n = 1$ to $n = 0.2$ at $\phi_{hnf} = 0.04$ which reaches its peak at lower values of $n$

However, while decreasing $n$ enhances the convective motion , increasing the nanoparticle volume fraction ($\phi_{hnf}$)from 0 to 0.1 leads to a decline in ($|\Psi|_{max}$), regardless of the ($n$) value. This is attributed to the increase in fluid inertia and viscosity at higher particle loadings, which restricts the fluid flow. Nevertheless, the enhancement in thermal conductivity due to higher nanoparticle volume fraction counteracts this adverse impact in reduced mobility, resulting in improved heat transfer rates., as demonstrated by the consistent increase of ($\overline{(Nu)}_l$). The highest enhancement in($\overline{(Nu)}_l$) observed for $n = 0.2$ , highlighting the significant role of shear-thinning behavior in augmenting heat transfer.

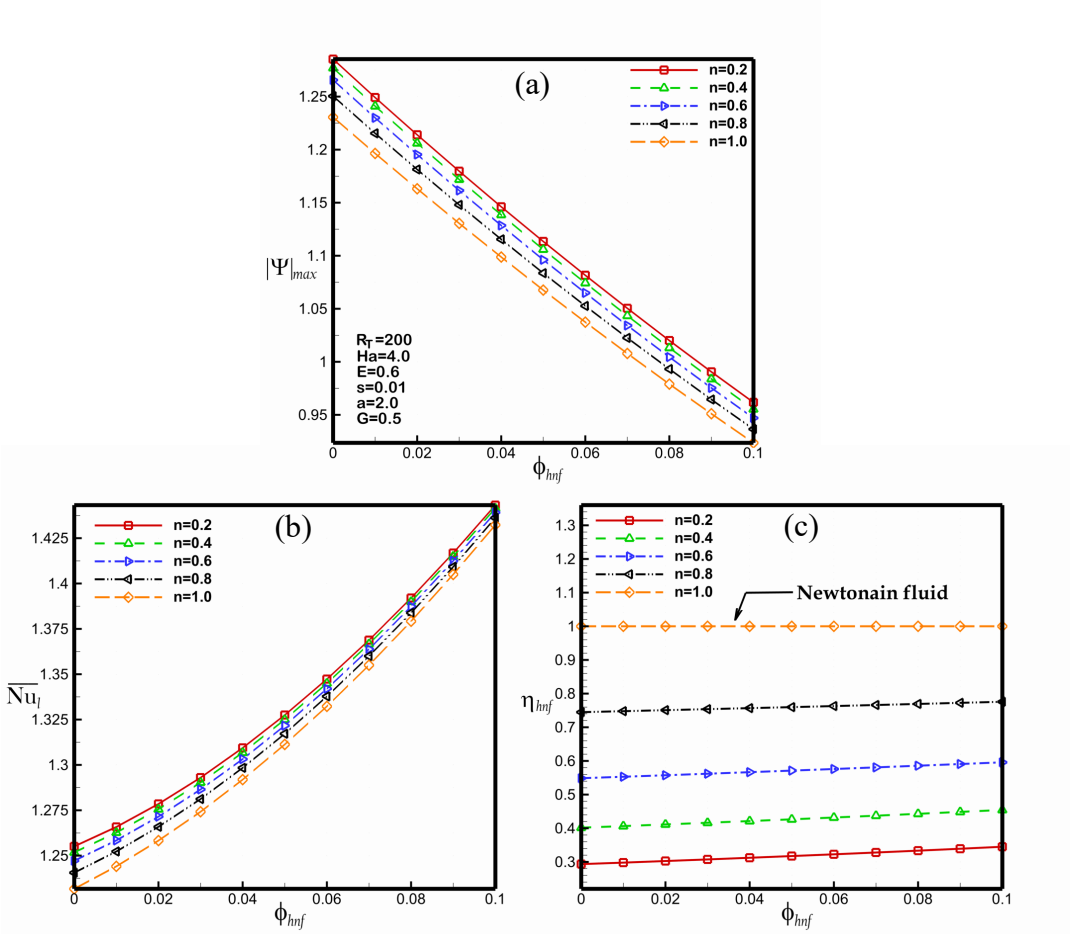



*Figure 4.22:The dependency of: (a) the maximum absolute stream function; (b) the average Nusselt number on the left wall; and (c) the apparent viscosity of the hybrid nanofluid on the function of the concentration percentage ($\phi$) and various power law index values (n)*

Figure 4.23 illustrates the influence of the dimensionless time constant E on natural convection of the ($Al_2O_3 - Cu$ water) hybrid nanofluid. Subfigures (4.23-a), (4.23-b), and (4.23-c) present the maximum absolute stream function ($|\Psi|_{max}$ ) , the average Nusselt number ($\overline{(Nu)}_l$) and the apparent viscosity $\eta_{hnf}$ respectively as a function of the nanoparticle volume fraction $\phi_{hnf}$ for various $E$ values. At $R_T$=200,G=0.5,Ha=4,a=2,n=0.8 ,and s=0.01. The results presented in fig 4.23-c demonstrate that the increase in the non-dimensional time constant ($E$) from the Newtonian case $E = 0\ to\ E = 100$ enhances the shear-thinning effect, resulting in a significant decline of 72% in the apparent viscosity $\eta_{hnf}$ . This

viscosity reduction diminishes the internal viscous resistance, thereby promoting flow circulation. This enhanced circulation is evidenced in fig 4.23-a by a 4.66% increase in the maximum stream function $|\Psi|_{max}$ between these two cases ($E = 0\ and\ E = 100$) at $\phi = 0.04$ . This intensified circulation enhances convective heat transfer, accordingly leading to a 1.40% rise in the average Nusselt number ($\overline{(Nu)}_l$) with increasing $E$.

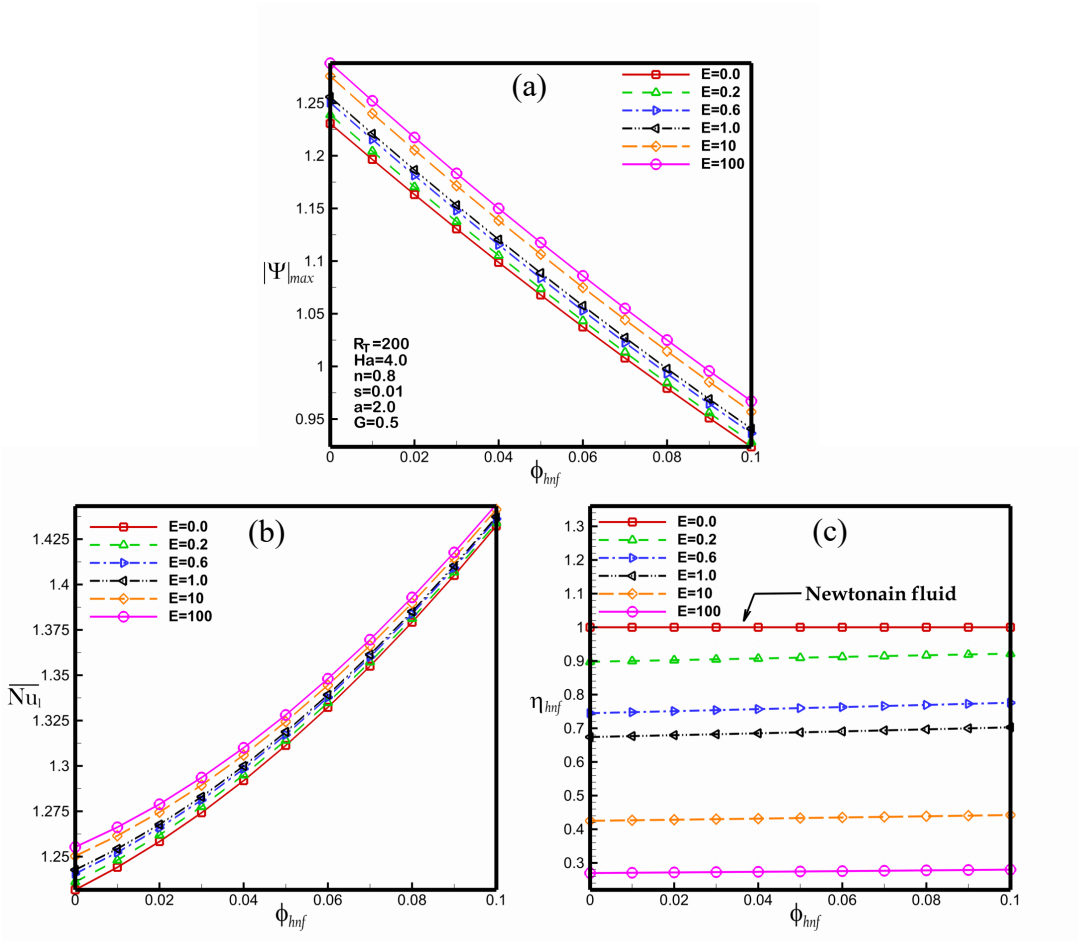



*Figure 4.23:The dependency of: (a) the maximum absolute stream function; (b) the average Nusselt number on the left wall; and (c) the apparent viscosity of the hybrid nanofluid on the function of the concentration percentage ($\phi$) and various dimensionless time constant values (E)*

The findings presented in Figure 4.24 and Figure 4.25, which investigate the effects of the viscosity ratio parameter ($s$) and the Carreau–Yasuda dimensionless parameter ($a$) , are aligned with the trends previously observed for the power-law index (n) and the time constant ($E$). It is noted that a decrease in either ($s$) or ($a$) amplifies the shear-thinning behavior of the fluid. This effect is evidenced by a decline in the apparent viscosity. This effect is illustrated in Figures 3(c) and 4(c), where lower values of (s) or (a) correspond to significantly reduced viscosity levels. For instance, at $\phi = 0.1\eta_{hnf}$ decreases from 1.0 (for $s = 1$) – Newtonian case- to below 0.7 (for $s = 0.0$).

This viscosity reduction promotes stronger natural convection, as evidenced by the rise in the maximum absolute stream function ($|\Psi|_{max}$) shown in (fig 4.24-a) and (fig 4.25-a). In turn, the

enhancement in flow circulation consequently improves heat transfer efficiency. This enhancement is substantiated by the increased values of the Nusselt number ($\overline{(Nu)}_l$) observed with the decrease in both ($s$) and ($a$) values.

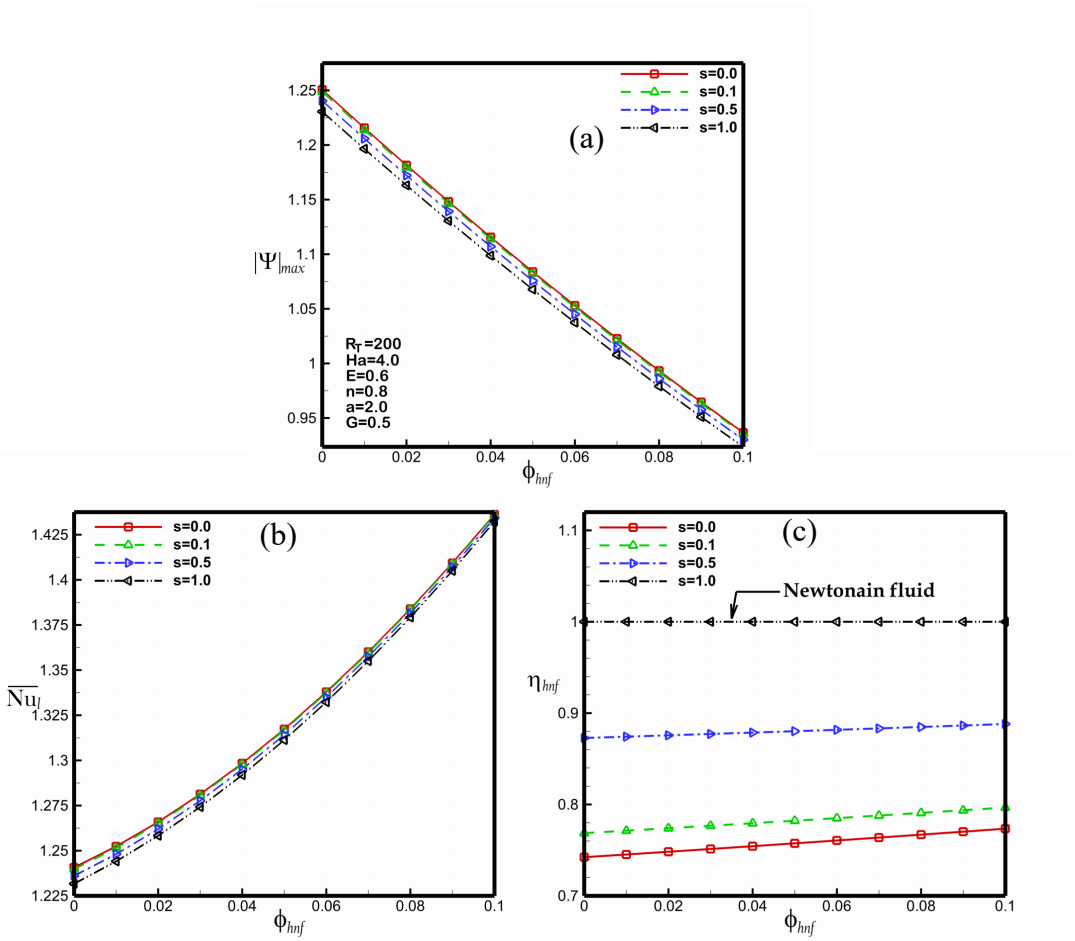



*Figure 4.24:The dependency of: (a) the maximum absolute stream function; (b) the average Nusselt number on the left wall; and (c) the apparent viscosity of the hybrid nanofluid on the function of the concentration percentage ($\phi$) and various viscosities ratio values (s)*

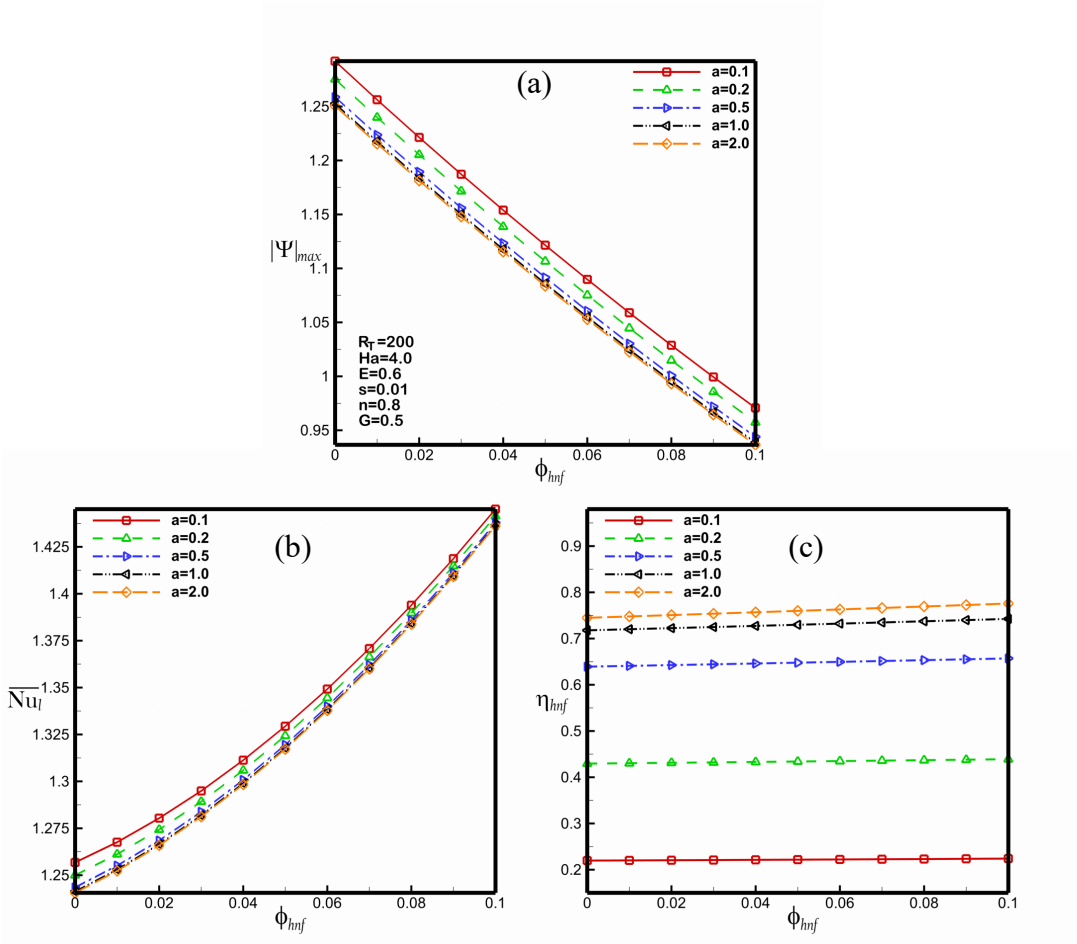



*Figure 4.25:The dependency of: (a) the maximum absolute stream function; (b) the average Nusselt number on the left wall; and (c) the apparent viscosity of the hybrid nanofluid on the function of the concentration percentage ($\phi$) and various dimensionless parameter values (a)*

The results demonstrate that the effect of Carreau–Yasuda parameters $(n, E, s, a)$ on flow strength and apparent viscosity is more pronounced than their effect on improving heat transfer. This effect becomes more evident with increasing nanoparticle concentration. However, even with improved effective thermal conductivity of the hybrid nanofluid, excessive loading leads to higher effective viscosity, thereby suppressing circulation intensity and limiting the net thermal gain.

Figure 4.26 illustrates the influence of the inertial coefficient $(G)$ on the flow dynamics and heat transfer. At $R_T$=200,G=0.5,Ha=4,a=2,n=0.8 ,and s=0.01. It is evident that with a rise in the inertial coefficient $(G)$,from the Darcy flow $(G = 0)$ to stronger inertial resistance$(G = 10)$, the flow rate diminishes significantly (fig 4.26-a). This weakening of circulation lowers the shear rate. Given the shear-thinning behavior of the nanofluid, a lower shear rate prompts an increase in the apparent viscosity $\eta_{hnf}$ (fig 4.26-c). Consequently, these changes in rheological properties detrimentally affect convective heat transfer efficiency, as reflected by the marked reduction in the Nusselt number $(\overline{(Nu)}_l)$ values. (fig 4.26-b).

The influence of $(G)$ is further amplified by nanoparticle loading $\phi_{hnf}$. Higher concentrations elevate the apparent viscosity $\eta_{hnf}$, thereby making the medium more sensitive to the inertial effects. Consequently, the suppression of circulation becomes stronger at larger concentrations. However, despite this combined inhibitory effect (inertial and viscosity) on fluid mobility, the net impact of a higher nanoparticle concentration $\phi_{hnf}$ on the overall thermal performance of the hybrid nanofluid remains superior to that of the base fluid. This is attributed to the enhancement in thermal conductivity, achieved via nanoparticle inclusion, which offsets the negative effects arising from increased viscosity and reduced flow velocity.

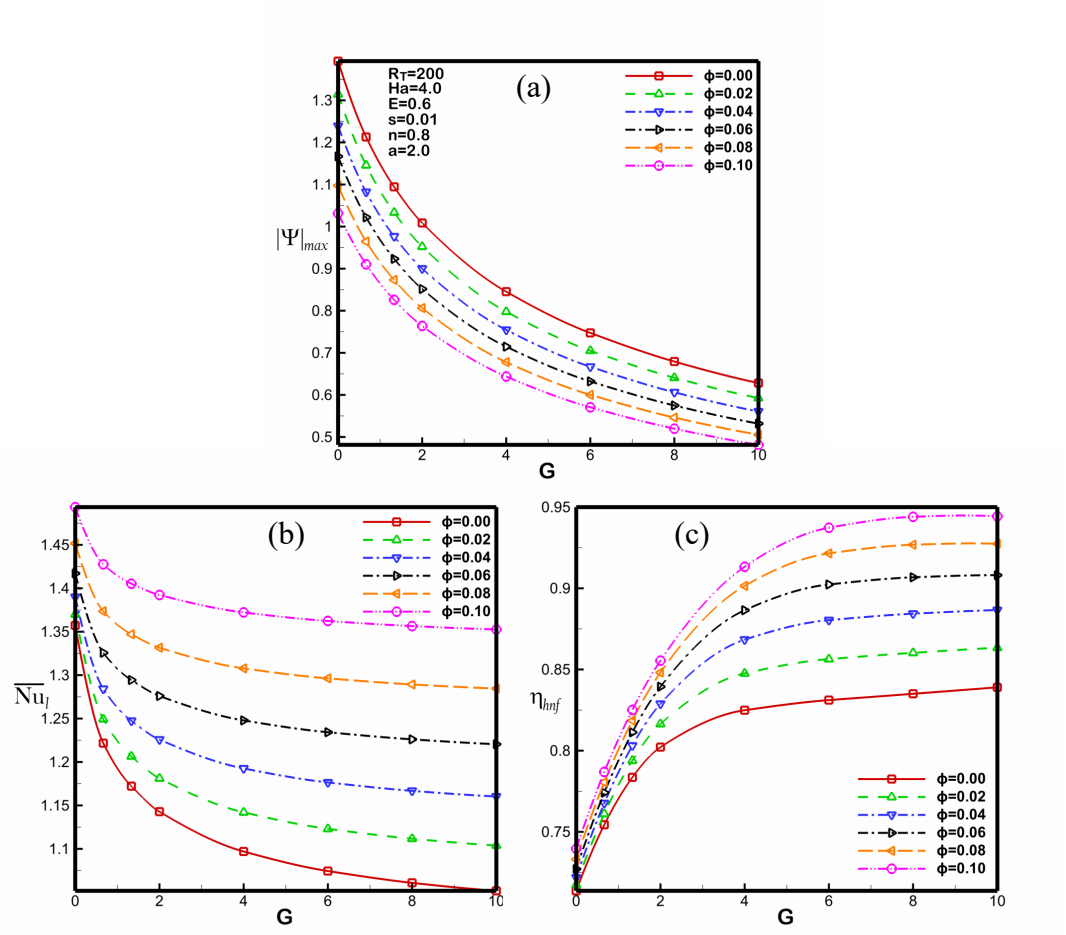



*Figure 4.26: The dependency of: (a) the maximum absolute stream function; (b) the average Nusselt number on the left wall; and (c) the apparent viscosity of the hybrid nanofluid on the function of the inertial parameter and various volumetric fraction values ($\phi$)*

Figure 4.27 presents the influence of the Hartmann number $(Ha)$ on the flow and heat transfer characteristics in terms of (fig 4.27-a) the maximum absolute stream function $|\Psi|_{max}$ ,(fig 4.27-b) the average Nusselt number on the left wall $\overline{(Nu)}_l$, and (fig 4.27-c) the apparent viscosity $\eta_{hnf}$.At $R_T$=200,G=0.5,Ha=4,a=2,E=0.6 ,and s=0.01. As evident in (fig 4.27-a), flow circulation exhibits a significant decline with increasing Hartmann number $(Ha)$ values. This attenuation in flow strength is attributed to the damping effect of the Lorentz force, whereby magnetic forces suppress buoyancy-driven

motion and inhibit circulation development. This flow suppression led to a reduction in the shear rate. and given the shear-thinning nature of the nanofluid, this diminished shear rate results in a noticeable increase in the effective viscosity (fig 4.27-c). As a result, the heat transfer performance deteriorates, demonstrated by a decrease in the Nusselt number $\overline{(Nu)}_l$ of approximately 40% between $Ha = 0$ and $Ha = 10$ (fig 4.27-b).

The magnitude of the Lorentz force's damping effect is intensified with increasing nanoparticle concentration, as the enhanced viscosity amplifies the susceptibility of the flow to magnetic damping. However, despite this double inhibitory effect on flow dynamics, the increase in nanoparticle concentration still yields a net positive contribution to heat transfer. This result is explained by the dominance of the significant enhancement in thermal conductivity – achieved through nanoparticle inclusion – over the adverse effects of magnetic damping and increased viscosity

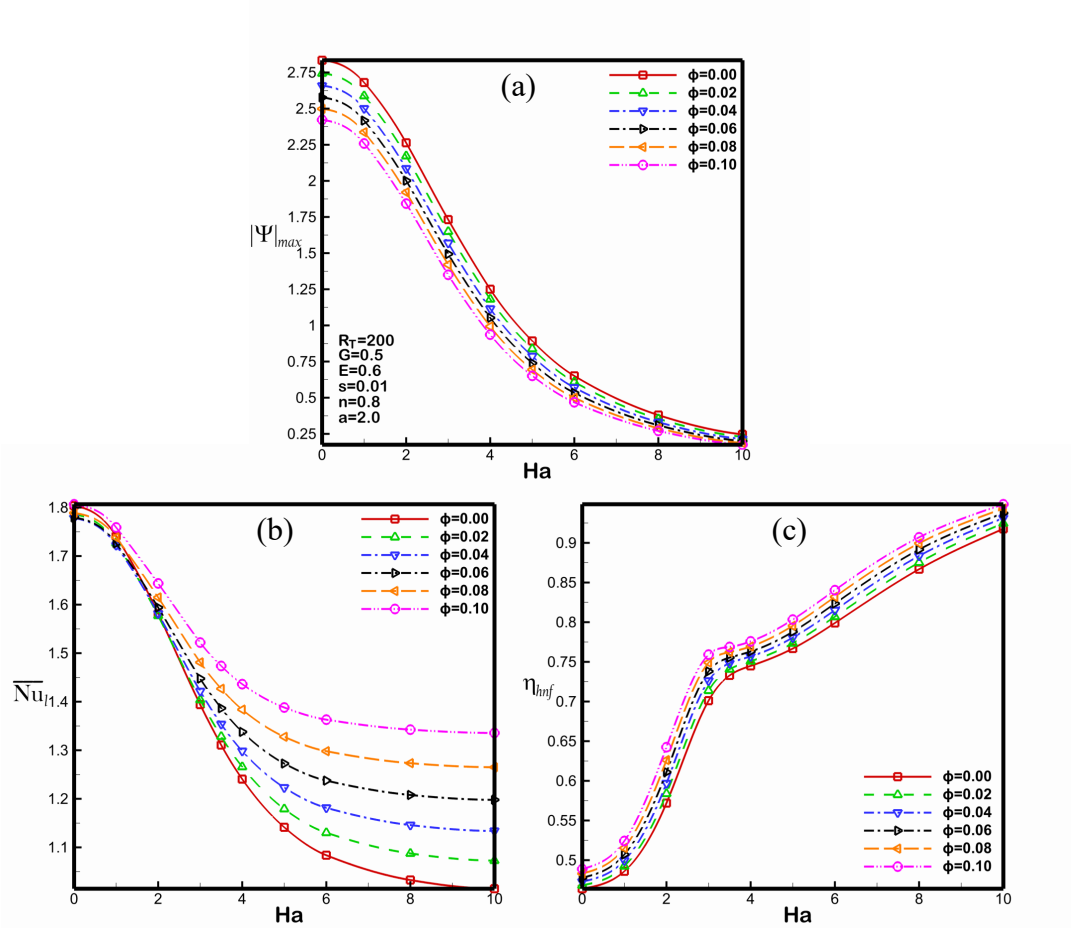



*Figure 4.27: The dependency of: (a) the maximum absolute stream function; (b) the average Nusselt number on the left wall; and (c) the apparent viscosity of the hybrid nanofluid on the function of Hartmann number(Ha) and various volumetric fraction values ($\phi$)*

Figure 4.28 depicts the influence of the Rayleigh-Darcy number ($R_T$) on natural convection performance. At the zero value of the Rayleigh-Darcy number ($R_T = 0$), buoyancy forces vanish. Consequently, the dominant heat transfer mechanism becomes pure thermal conduction. This is confirmed by the average Nusselt number $\overline{(Nu)}_l$,which drops to the unity value ($\overline{(Nu)}_l = 1$) at ($\phi = 0$)

. The absence of buoyancy results in a complete stagnation of fluid motion, as reflected by a zero-stream function value ($|\Psi|_{max} = 0$).The absence of flow also eliminates the shear rate within the fluid. causing the shear-thinning hybrid nanofluid to lose its non-Newtonian characteristics and exhibit Newtonian behavior, displaying its highest apparent viscosity ($\eta_{hnf} = 1$), as depicted in fig 4.28-c.

With increasing Rayleigh number ($R_T$), buoyancy forces begin to overcome the effects of viscous and inertial effects. Both the stream function $|\Psi|_{max}$ (fig.4.28-a) and Nusselt number $\overline{(Nu)}_l$ (fig.4.28-b) rise steadily with $R_T$. A distinct transition is noted around $R_T \approx 100$, where the slope of the Nusselt curve increases sharply, indicating enhanced convection intensity. This acceleration in thermal performance enhancement is attributed to the shear-thinning nature of the hybrid nanofluid. Higher buoyancy strengthens circulation, elevating the shear rate. Consciously leads to a sharp decrease in the apparent viscosity $\eta_{hnf}$ (fig.4.28-c). The lowered viscosity facilitates fluid flow, which further enhances convective heat transfer. Eventually, at $R_T = 200$, the system achieves its peak performance, with the Nusselt number reaching its maximum.

Moreover, nanoparticle loading enhances the thermal performance across all $R_T$ values. At higher concentrations, the improvement in effective thermal conductivity counterbalances the viscosity drawback, particularly evident at lower Rayleigh numbers. This results in consistently higher Nusselt numbers compared to the base fluid. Ultimately, at $R_T = 200$, the highest level of convective efficiency is achieved, demonstrating the combined effect of buoyancy and the conductivity augmentation induced by nanoparticles.

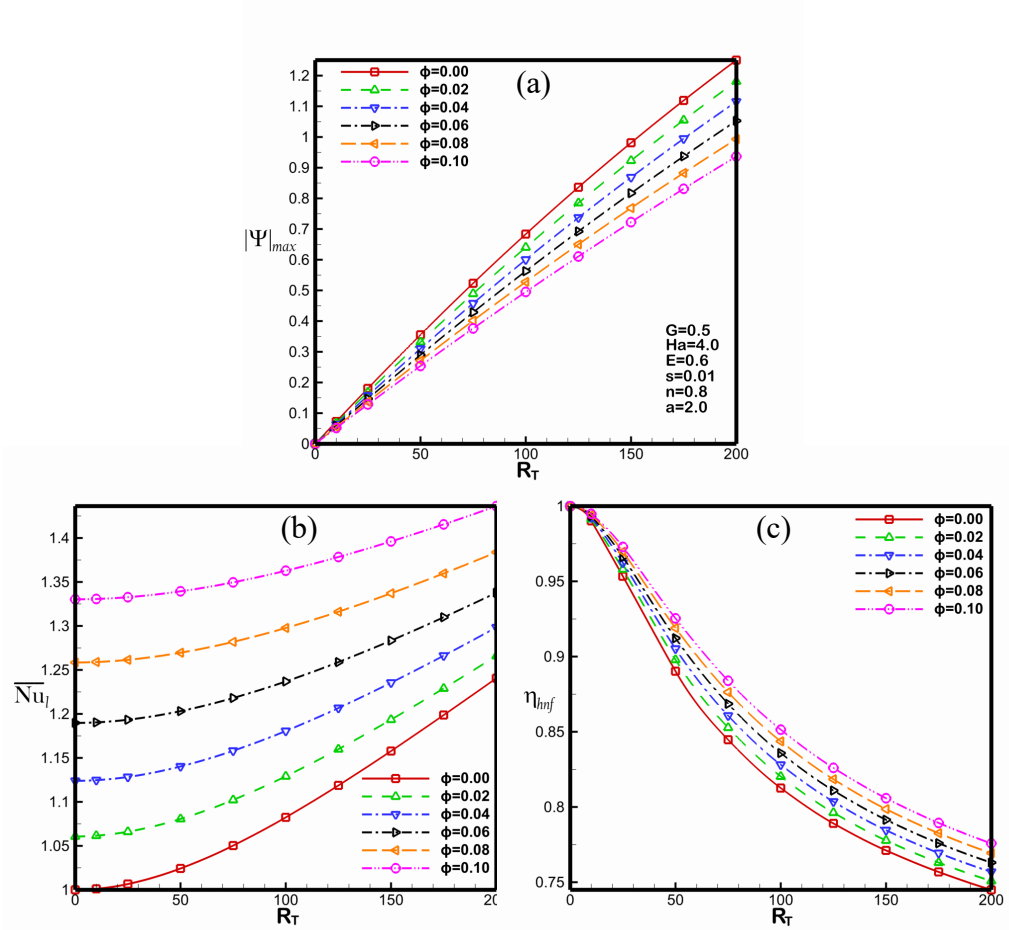



*Figure 4.28:The dependency of: (a) the maximum absolute stream function; (b) the average Nusselt number on the left wall; and (c) the apparent viscosity of the hybrid nanofluid on the function of Rayleigh number($R_T$) and various volumetric fraction values ($\phi$)*

Figure 4.29 presents the impact of the cavity inclination angle (γ) on flow intensity and the convection heat transfer characteristics. At $R_T$=200,G=0.5,Ha=4,a=2,E=0.6 ,n=0.8 and s=0.01 As depicted in Fig. 4.29-a, the maximum absolute stream function $|\Psi|_{max}$) diminishes with increasing inclination angle until it completely vanishes ($|\Psi|_{max}$= 0) at the extreme angles (γ = ±90°). At these angles, the gravitational force nullifies the buoyancy-driven flow, resulting in a complete cessation of fluid motion.

This stagnation reduces the shear rate to zero. For the case of shear-thinning non-Newtonian nanofluid, the absence of shear leads it to reach its maximum apparent viscosity ($\eta_{hnf}$ = 1), as shown in Fig. 4.29-c. Consequently, heat transfer becomes purely conductive, as evidenced by the average Nusselt number (fig 4.29-b) on the wall dropping to unity ($\overline{(Nu)}_l$ = 1) at (γ = ±90°) for the pure fluid.

When the cavity is inclined away from these extreme orientations, the thermal convection reemerges. Leading to an enhancement of both the Nusselt number ($\overline{(Nu)}_l$) and stream function ($|\Psi|_{max}$). The

findings indicate that the optimal thermal performance is achieved at an inclination angle of $\gamma = 30°$, where the Nusselt number exhibits an improvement of 20% compared to its value at ($\gamma = \pm 90°$).

Furthermore, despite the significant flow suppression at ($\gamma = \pm 90°$), the inclusion of nanoparticles significantly improves the heat transfer even under a conduction-dominated regime. For instance, increasing $\phi_{hnf}$ from 0 to 0.1 enhances $\overline{(Nu)}_l$ from 1.0 to 1.33. This enhancement is attributed to the improvement of the effective thermal conductivity due to the presence of nanoparticles, which compensate for the adverse impact of suppressed convection.

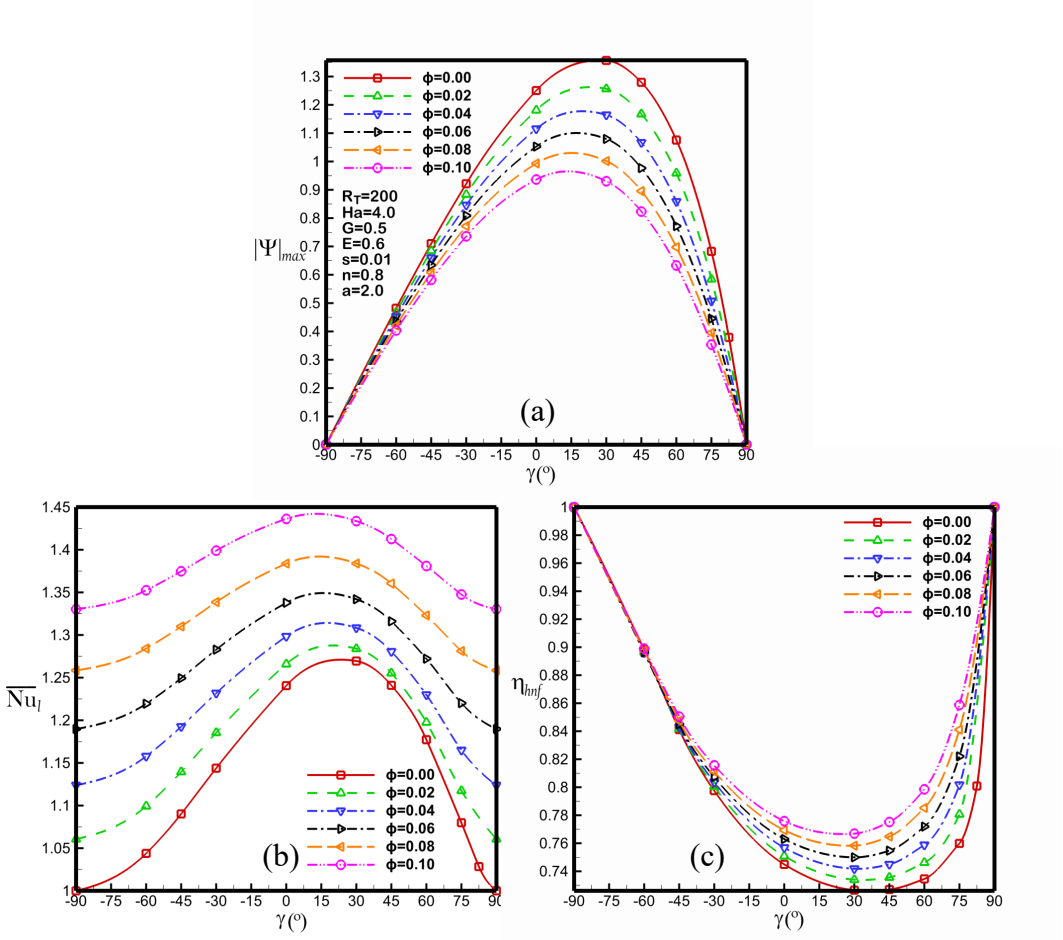



*Figure 4.29:The dependency of: (a) the maximum absolute stream function; (b) the average Nusselt number on the left wall; and (c) the apparent viscosity of the hybrid nanofluid on the function of the Inclination angle ($\gamma$) and various volumetric fraction values ($\phi$)*

Figure 4.30 presents a comparative analysis of the three investigated fluids (SWCNT-water,$Al_2O_3$-water and Cu-$Al_2O_3$ water). Fig. 4.30-a illustrates distinct flow behaviors in terms of stream function. While the SWCNT/water nanofluid enhances circulation strength with increasing nanoparticle concentration. The $Al_2O_3$/water shows an almost unchanged trend. In contrast, the hybrid ($Al_2O_3$+Cu/water) nanofluid exhibits a progressive decline in $|\Psi|_{max}$. These observations indicate that

the inclusion of SWCNTs promotes buoyancy-driven circulation owing to their minimal viscosity effect, whereas the hybrid suspension is subject to viscous damping, which suppresses the effects of buoyancy.

Fig. 4.30-b confirms these rheological differences directly impact heat transfer performance. The SWCNT/water nanofluid provides the highest thermal enhancement, with the Nusselt number nearly doubling as $\phi_{hnf}$ increases from 0 to 0.1, driven by its superior effective thermal conductivity combined with minimal viscosity growth. By comparison, $Al_2O_3$-water presents only a moderate improvement, attributable to enhanced conduction rather than stronger convective motion. The hybrid nanofluid registers the weakest performance, as the conductivity gain from copper particles is offset by the notable rise in effective viscosity, which suppresses buoyancy-driven circulation.

Fig. 4.30-c further validates this observation. The hybrid nanofluid exhibits the steepest increase in apparent viscosity, $Al_2O_3$/water presents moderate growth, while SWCNT/water shows only a slight rise. This trend underlines the pivotal role of rheology in shear-thinning fluids; increased viscosity directly hampers convective motion, consequently diminishing the efficiency of thermal transport. Overall, SWCNT/water is the most effective thermal fluid, achieving a favorable equilibrium between high thermal conductivity and minimal viscous resistance. $Al_2O_3$/water. In contrast, it has shown restricted gains, chiefly driven by conduction with minor enhancements in convection, while the hybrid $Al_2O_3$+Cu/water fails to achieve the expected synergistic benefit due to the high viscosity, which weakens the conductivity benefit

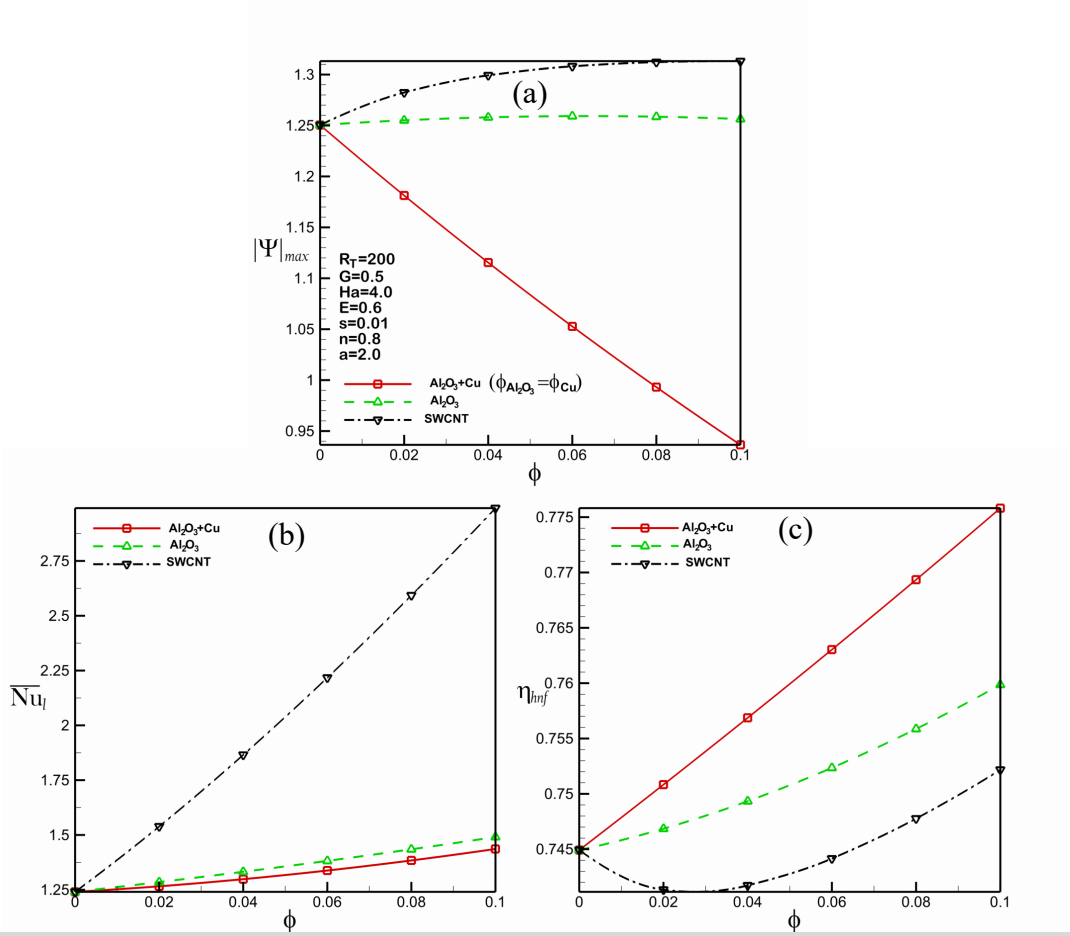



*Figure 4.30 comparison between the hybrid nanofluid ($Al_2O_3$+Cu/water),the nanofluids ($Al_2O_3$/water)and (SWCNT/water) in term of (a) the maximum absolute stream function; (b) the average Nusselt number on the left wall; and (c) the apparent viscosity*

# CHAPTER 5

# Conclusion and recommendation

# 5. CHAPTER V: CONCLUSION AND PERSPECTIVES

## 5.1. **Conclusion**

The present doctoral thesis aimed to conduct a comprehensive numerical analysis of natural convection heat transfer generated a gradient of temperature in a porous medium saturated with non-Newtonian nanofluids. The examined field consisted of an inclined two-dimensional square cavity, characterized by vertical walls maintained at different constant temperatures ($T_h$ and $T_c$), while the horizontal walls were thermally insulated.

the Dupuit–Darcy model was employed to model the flow behavior in the porous medium, . The Boussinesq approximation was applied to consider buoyancy-driven convention. The Carreau–Yasuda model was used to represent the rheological behavior of the non-Newtonian nature of the studied fluids, namely: the single-walled carbon nanotube (SWCNT)–water nanofluid, the alumina–water ($Al_2O_3$–water) nanofluid, and the hybrid $Al_2O_3$–Cu/water nanofluid.

The study was organized into two primary parts. The initial segment analyzed the characteristics of the non-Newtonian SWCNT–water nanofluid and compared it with that of $Al_2O_3$–water, while the second segment focused on the hybrid $Al_2O_3$–Cu/water nanofluid, drawing comparisons with the previous cases(SWCNT-Water and $Al_2O_3$-Water). Using a numerical algorithm created in FORTRAN, the governing equations and related boundary conditions were solved using the finite difference method (FDM) on a uniform grid.

A complete parametric analysis was conducted to explore the effects of the Carreau–Yasuda model parameters (n, E, a, s), the Hartmann number (Ha), the inertial parameter (G), the Darcy-Rayleigh number (Ra), and the inclination angles of both the cavity ($\gamma$) The established numerical code's validity and correctness were confirmed through comparisons with previously published results, demonstrating excellent agreement and confirming the resilience of the proposed numerical methodology

The main findings and interpretations of this study are summarized as follows:

- Increasing the Rayleigh number leads to improvements in both flow and heat transfer.
- Increasing the magnetic field intensity leads to a considerable decrease in both fluid circulation and heat transfer, resulting from the Lorentz force. While magnetic fields can regulate convection, excessive intensity affects thermal efficiency.
- The improvements in shear-thinning properties (reduced effective viscosity) led to a significant increase in fluid motion and consequently an improvement in convective heat transfer. However, these positive rheological benefits gradually diminish with an increase in either the magnetic field strength (high Ha) or higher nanoparticle volume fractions ($\phi$),

especially in the $Al_2O_3$+Cu hybrid nanofluid case. Moreover, the maximum convective heat transfer rate was achieved at a power-law index (n) of 0.2, representing an improvement of 4% compared to the Newtonian case (n=1)

- The reduction in inertial resistance (i.e., G →0 Darcy flow) significantly enhances convective flow and heat transfer performance. , This effect results in an increase in the heat transfer rate reaching up to 85% for( SWCNT-water) case and up to 95 % in the hybrid nanofluid(Al2O3+Cu water) case
- The combined synergistic effect of intensified Lorentz force (Ha) and elevated inertial damping (high G), leads to a significant reduction of convective currents. This joint suppression results in a shift in the heat transfer regime state dominated from a convection to a thermal conduction
- The incorporation of SWCNTs significantly augments the effective thermal conductivity of the fluid. While increased nanoparticle concentration correlates with elevated viscosity, the aggregate effect is a substantial improvement in convective heat transfer. A concentration increase from $\varphi = 0.0$ to 0.1 leads to a 76% rise in heat transfer performance, demonstrating the potential of SWCNT-based nano fluid in energy systems
- The best cavity inclination angle for obtaining maximum thermal performance is $\gamma \approx 30\circ$, since this angle promotes the maximization of heat flow and the overall heat transfer rate. However, selecting the maximal angle ($\gamma = 90\circ$) renders the convection ineffective since it strongly suppresses fluid flow. This ultimately causes inefficient heat transfer that is largely controlled by the thermal conduction mode
- The SWCNT water nanofluid shows a marked superiority over the other fluids under investigation—$Al_2O_3$–Water and ($Al_2O_3$ + Cu)–Water—owing to its reduced effective viscosity and enhanced thermal conductivity, which collectively improve natural convective heat transfer in the medium. In contrast, the hybrid nanofluid ($Al_2O_3$ + Cu)–water demonstrates the least efficient performance of the three fluids, principally due to its elevated viscosity and increased sensitivity to inertial effects within the cavity.

## 5.2. **PERSPECTIVES:**

- Investigations of further non-Newtonian fluid types are recommended. Therefore, broadening the study to include different rheological models will reveal how the same governing equations within the cavity affect their behavior.

- It is recommended to vary the form of the cavity (e.g., triangular, hexagonal, or circular cavities) to examine the influence of non-square geometry on the flow and heat transfer efficiency of non-Newtonian fluids

# REFERENCES

Abbas, Z., Arslan, M. S., & Rafiq, M. Y. (2024). Numerical modeling of Carreau–Yasuda fluid with induced magnetic field in a heated curved channel having ciliary walls. *Numerical Heat Transfer, Part B: Fundamentals*, 1-21. https://doi.org/10.1080/10407790.2024.2310714

Abderrahmane, A., Hatami, M., Medebber, M., Haroun, S., Ahmed, S. E., & Mohammed, S. (2022). Non-Newtonian nanofluid natural convective heat transfer in an inclined Half-annulus porous enclosure using FEM. *Alexandria Engineering Journal*, *61*(7), 5441-5453. https://doi.org/10.1016/j.aej.2021.11.004

Adnan, Nadeem, A., Khan, S. U., Khan, Y., Akermi, M., & Hassani, R. (2024). Features of hydrocarbon liquid-based nanofluid under augmentation of parametric ranges in non-Darcy media. *Modern Physics Letters B*, 2550041.

Afsana, S., Molla, M. M., Nag, P., Saha, L. K., & Siddiqa, S. (2021). MHD natural convection and entropy generation of non-Newtonian ferrofluid in a wavy enclosure. *International Journal of Mechanical Sciences*, *198*, 106350. https://doi.org/10.1016/j.ijmecsci.2021.106350

Ahmed, S., & Mahdy, A. (2016). Laminar MHD natural convection of nanofluid containing gyrotactic microorganisms over vertical wavy surface saturated non-Darcian porous media. *Applied Mathematics and Mechanics*, *37*, 471-484.

Akram, U., Akbar, Y., & Ahmad, W. (2023). Thermodynamic analysis for peristaltic flow of Carreau-Yasuda magneto nanofluid through a porous medium. *Waves in Random and Complex Media*, 1-17. https://doi.org/10.1080/17455030.2023.2173496

Alfvén, H. (1942). Existence of electromagnetic-hydrodynamic waves. *Nature*, *150*(3805), 405-406. https://doi.org/10.1038/150405d0

Alilat, D., Alliche, M., Rebhi, R., & Borjini, M. (2020). Inertial and Porosity Effects on Dupuit-Darcy Natural Convection of Cu-Water Nanofluid Saturated High Thermal Conductive Porous Medium. *Special Topics & Reviews in Porous Media: An International Journal*, *11*(5). https://doi.org/10.1615/SpecialTopicsRevPorousMedia.2020033717

Alilat, D., Alliche, M., Rebhi, R., & Chamkha, A. J. (2020). Inertial effects on the hydromagnetic natural convection of SWCNT-water nanofluid-saturated inclined rectangular porous medium. *International Journal of Fluid Mechanics Research*, *47*(5). https://doi.org/10.1615/InterJFluidMechRes.2020035103

Alloui, Z., & Vasseur, P. (2015). Natural convection of Carreau–Yasuda non-Newtonian fluids in a vertical cavity heated from the sides. *International Journal of Heat and Mass Transfer*, *84*, 912-924.

Alqahtani, A. M., Bilal, M., Elsebaee, F. A. A., Eldin, S. M., Alsenani, T. R., & Ali, A. (2023). Energy transmission through carreau yasuda fluid influenced by ethylene glycol with activation energy and ternary hybrid nanocomposites by using a mathematical model. *Heliyon*, *9*(4). https://doi.org/10.1016/j.heliyon.2023.e14740

Balandin, A. A. (2011). Thermal properties of graphene and nanostructured carbon materials. *Nature materials*, *10*(8), 569-581.

Balmforth, N. J., Frigaard, I. A., & Ovarlez, G. (2014). Yielding to stress: recent developments in viscoplastic fluid mechanics. *Annual review of fluid mechanics*, *46*(1), 121-146.

Bani-Fwaz, M. Z., Adnan, Karim, S., Ullah Khan, S., Bilal, M., Khan, Y., & Tlili, I. (2025). Significance of Fe3O 4/MnZnFe2O4 nanoparticles for thermal efficiency of ethylene glycol: Analysis for single-phase nanofluid flow using Cattaneo Christov theory. *Modern Physics Letters B*, 2550105.

Barnes, H. A. (2000). *A handbook of elementary rheology* (Vol. 1). University of Wales, Institute of Non-Newtonian Fluid Mechanics Aberystwyth.

Barnes, H. A., Hutton, J. F., & Walters, K. (1989). *An introduction to rheology* (Vol. 3). Elsevier.

Barnoon, P., & Toghraie, D. (2018). Numerical investigation of laminar flow and heat transfer of non-Newtonian nanofluid within a porous medium. *Powder Technology*, *325*, 78-91.

Batchelor, G. K. (1977). The effect of Brownian motion on the bulk stress in a suspension of spherical particles. *Journal of Fluid Mechanics*, *83*(1), 97-117.

Baytaş, A. (2000). Entropy generation for natural convection in an inclined porous cavity. *International Journal of Heat and Mass Transfer*, *43*(12), 2089-2099. https://doi.org/10.1016/S0017-9310(99)00291-4

Bear, J. (1972). *Dynamics of fluids in porous media*. Courier Corporation.

Benygzer, C., Bouzit, M., & Mokhefi, A. (2023). Natural convection a square cavity partially filled with porous medium and nanofluid using Buongiorno's model. *The Romanian Journal of Technical Sciences. Applied Mechanics.*, *68*(1), 91-107.

Bhanvase, B., & Barai, D. (2021). *Nanofluids for heat and mass transfer: Fundamentals, sustainable manufacturing and applications*. Academic Press.

Bianco, V., Manca, O., Nardini, S., & Vafai, K. (2015). Heat transfer enhancement with nanofluids.

Bilal, M., Ullah, I., Alam, M. M., Shah, S. I., & Eldin, S. M. (2023). Energy transfer in Carreau Yasuda liquid influenced by engine oil with Magnetic dipole using tri-hybrid nanoparticles. *Scientific Reports*, *13*(1), 5432. https://doi.org/10.1038/s41598-023-32052-2

Bird, R. B., Armstrong, R. C., & Hassager, O. (1987). Dynamics of polymeric liquids. Vol. 1: Fluid mechanics.

Bird, R. B., Stewart, W. E., & Lightfoot, E. N. (2002). Transport Phenomena 2nd edition,(2002). In: John Wiley & Sons.

Bobkov, V., Fokin, L., Petrov, E., Popov, V., Rumiantsev, V., & Savvatimsky, A. (2008). Thermophysical properties of materials for nuclear engineering: a tutorial and collection of data. *IAEA, Vienna*, 18-21.

Boualit, A., Zeraibi, N., Chergui, T., Lebbi, M., Boutina, L., & Laouar, S. (2017). Natural convection investigation in square cavity filled with nanofluid using dispersion model. *International Journal of Hydrogen Energy*, *42*(13), 8611-8623.

Brinkman, H. C. (1949). A calculation of the viscous force exerted by a flowing fluid on a dense swarm of particles. *Flow, Turbulence and Combustion*, *1*(1), 27-34.

Brinkman, H. C. (1952). The viscosity of concentrated suspensions and solutions. *Journal of Chemical Physics*, *20*(4), 571-571. https://doi.org/10.1063/1.1700493

Carreau, P. (1968). *Rheological equations of state from molecular network theories* PhD thesis, University of Wisconsin, Madison].

Cheng, C.-Y. (2006). Non-Darcy natural convection heat and mass transfer from a vertical wavy surface in saturated porous media. *Applied Mathematics and Computation*, *182*(2), 1488-1500.

Chhabra, R. P., & Richardson, J. F. (2011). *Non-Newtonian flow and applied rheology: engineering applications*. Butterworth-Heinemann.

Choi, S. U., & Eastman, J. A. (1995). *Enhancing thermal conductivity of fluids with nanoparticles*.

Chung, D. (2001). Materials for thermal conduction. *Applied Thermal Engineering*, *21*(16), 1593-1605.

Cross, M. M. (1965). Rheology of non-Newtonian fluids: a new flow equation for pseudoplastic systems. *Journal of colloid science*, *20*(5), 417-437.

Darcy, H. (1856). *Les fontaines publiques de la ville de Dijon: exposition et application des principes à suivre et des formules à employer dans les questions de distribution d'eau* (Vol. 1). Victor dalmont.

Das, S. K., Choi, S. U., & Patel, H. E. (2006). Heat transfer in nanofluids—a review. *Heat transfer engineering*, *27*(10), 3-19.

Davidson, P. A. (2017). *Introduction to magnetohydrodynamics* (Vol. 55). Cambridge university press.

Djamel, A., Rebhi, R., Mounir, A., & Chamkha, A. J. (2023). ENHANCEMENT OF DUPUIT-DARCY THERMAL CONVECTION OF SWCNT-WATER NON-NEWTONIAN NANOFLUID SATURATED POROUS MEDIUM. *Heat Transfer Research*, *54*(8). https://doi.org/10.1615/HeatTransRes.2022045431

Dullien, F. A. (1992). *Porous media: fluid transport and pore structure*. Academic press.

Einstein, A. (1905). *Eine neue bestimmung der moleküldimensionen* ETH Zurich].

Einstein, A. (1906). Zur theorie der brownschen bewegung. *Annalen der physik*, *324*(2), 371-381.

Ergun, S. (1952). Fluid flow through packed columns. *Chemical Engineering Progress*, *48*(2), 89.

Faisal, M., Anwar, T., & Javed, F. (2025). Buoyancy-induced nanofluid circulation in a novel configuration of a porous square cavity. *Partial Differential Equations in Applied Mathematics*, 101315.

Faraz, N., Majeed, A. H., Mehmood, A., Sajad, H., & Khan, Y. (2023). Features of the power-law fluid over cylinders in a channel via gap aspects: Galerkin finite element method (GFEM)-based study. *Frontiers in Physics*, *10*, 1081130. https://doi.org/10.3389/fphy.2022.1081130

Faraz, N., Nisar, M. S., Khan, Y., Hussain, A., & Iqbal, K. (2023). Natural convection of Cu-H2O nanofluid inside hexagonal enclosure fitted with a square cavity with a non-uniformly heated wall (s). *Results in Physics*, *51*, 106648. https://doi.org/10.1016/j.rinp.2023.106648

Figura, L. O., & Teixeira, A. A. (2007). *Food Physics: Physical properties—measurement and applications*. Springer.

Forchheimer, P. (1901). Wasserbewegung durch Boden. *Zeitschrift des Vereins deutscher Ingenieure*, *45*(45th Edition), 1782–1788.

Frank, M. (2011). White," Fluid Mechanics", McGraw Hill.

Frankel, S. P. (1950). Convergence rates of iterative treatments of partial differential equations. *Mathematics of Computation*, *4*(30), 65-75.

Fu, J., Thomas, H. R., & Li, C. (2021). Tortuosity of porous media: Image analysis and physical simulation. *Earth-Science Reviews*, *212*, 103439.

Garandet, J., Alboussiere, T., & Moreau, R. (1992). Buoyancy driven convection in a rectangular enclosure with a transverse magnetic field. *International Journal of Heat and Mass Transfer*, *35*(4), 741-748.

Geridonmez, B. P., & Oztop, H. F. (2019). Natural convection in a cavity filled with porous medium under the effect of a partial magnetic field. *International Journal of Mechanical Sciences*, *161*, 105077.

Ghalambaz, M., Mehryan, S., Izadpanahi, E., Chamkha, A. J., & Wen, D. (2019). MHD natural convection of Cu–Al 2 O 3 water hybrid nanofluids in a cavity equally divided into two parts by a vertical flexible partition membrane. *Journal of Thermal Analysis and Calorimetry*, *138*, 1723-1743.

Giwa, S., Sharifpur, M., Ahmadi, M., & Meyer, J. (2021). A review of magnetic field influence on natural convection heat transfer performance of nanofluids in square cavities. *Journal of Thermal Analysis and Calorimetry*, *145*, 2581-2623.

Gross, R., Baer, M. R., & Hickox Jr, C. (1986). The application of flux-corrected transport (FCT) to high Rayleigh number natural convection in a porous medium. International Heat Transfer Conference Digital Library,

Hamilton, R. L., & Crosser, O. K. (1962). Thermal conductivity of heterogeneous two-component systems. *Industrial & Engineering chemistry fundamentals*, *1*(3), 187-191.

Handbook, A. (2005). American society of heating. *Refrigerating and Air Conditioning Engineers, Atlanta*.

Heinemann, Z., & Mittermeir, G. (2013). Fluid flow in porous media.

Herschel, W. H., & Bulkley, R. (1926). Konsistenzmessungen von Gummi-Benzollösungen. *Kolloid-Zeitschrift*, *39*(4), 291-300. https://doi.org/10.1007/BF01432034

Hossain, M., & Rees, D. A. S. (1997). Non-Darcy free convection along a horizontal heated surface. *Transport in porous media*, *29*, 309-321.

Incropera, F. P., DeWitt, D. P., Bergman, T. L., & Lavine, A. S. (1996). *Fundamentals of heat and mass transfer* (Vol. 6). Wiley New York.

Iqbal, J., Abbasi, F., & Alam, M. (2025). Thermal enhancement in solar aircraft by using MHD Carreau-Yasuda nanofluid with solar radiation. *Aerospace Science and Technology*, *158*, 109906. https://doi.org/10.1016/j.ast.2024.109906

Javaherdeh, K., Karimi, H., & Khojasteh, A. (2021). Numerical study of heat transfer enhancement of non-Newtonian nanofluid in porous blocks in a channel partially. *Powder Technology*, *383*, 270-279.

Jino, L., & Kumar, A. V. (2021). Cu-water nanofluid MHD quadratic natural convection on square porous cavity. *International Journal of Applied and Computational Mathematics*, *7*(4), 164.

Kareem, R. S., & Abdulhadi, A. M. (2019). Effect of MHD and porous media on nanofluid flow with heat transfer: Numerical treatment. *Journal of advanced research in fluid mechanics and thermal sciences*, *63*(2), 317-328.

Khan, Y., Mahmood, R., Majeed, A. H., Irshad, S., Alameer, A., & Faraz, N. (2022). Finite element simulations of inclined magnetic field and mixed convection in an enclosure with periodically heated walls in the presence of an obstacle. *Frontiers in Physics*, *10*, 1006023.

Khanafer, K., & Vafai, K. (2019). Applications of nanofluids in porous medium: a critical review. *Journal of Thermal Analysis and Calorimetry*, *135*, 1479-1492.

Khanafer, K., Vafai, K., & Lightstone, M. (2003). Buoyancy-driven heat transfer enhancement in a two-dimensional enclosure utilizing nanofluids. *International Journal of Heat and Mass Transfer*, *46*(19), 3639-3653. https://doi.org/10.1016/S0017-9310(03)00156-X

Khechiba, K., Mamou, M., Hachemi, M., Delenda, N., & Rebhi, R. (2017). Effect of Carreau-Yasuda rheological parameters on subcritical Lapwood convection in horizontal porous cavity saturated by shear-thinning fluid. *Physics of Fluids*, *29*(6). https://doi.org/10.1063/1.4986794

Kim, S. H., Choi, S. R., & Kim, D. (2007). Thermal conductivity of metal-oxide nanofluids: particle size dependence and effect of laser irradiation.

Kumar, R., Bhattacharyya, A., & Seth, G. (2021). Heat transfer analysis on unsteady natural convection flow of silver nanofluid in a porous square cavity using local thermal non-equilibrium model. *Indian Journal of Physics*, 1-14. https://doi.org/10.1007/s12648-021-02137-7

Kumari, P., Nigam, M., Kumar, S., Kumar, V., Raturi, S., Pargaei, M., Murthy, S. V. K., & Kumar, B. R. (2019). Magnetic field effect on non-darcy mixed convection from a horizontal plate in a nanofluid-saturated porous medium. *Journal of Porous Media*, *22*(5).

Kwon, Y.-K., & Kim, P. (2006). Unusually high thermal conductivity in carbon nanotubes. *High Thermal Conductivity Materials*, 227-265.

Lauriat, G., & Prasad, V. (1989). Non-Darcian effects on natural convection in a vertical porous enclosure. *International Journal of Heat and Mass Transfer*, *32*(11), 2135-2148. https://doi.org/10.1016/0017-9310(89)90120-8

Lofrano, F. C., Morita, D. M., Kurokawa, F. A., & de Souza, P. A. (2020). New General Maximum Entropy Model for Flow Through Porous Media. *Transport in Porous Media*, *131*(2), 681-703. https://doi.org/10.1007/s11242-019-01362-3

Mahdy, A. (2009). MHD non-Darcian free convection from a vertical wavy surface embedded in porous media in the presence of Soret and Dufour effect. *International Communications in Heat and Mass Transfer*, *36*(10), 1067-1074.

Mahmood, R., Khan, Y., Rahman, N., Majeed, A. H., Alameer, A., & Faraz, N. (2022). Numerical computations of entropy generation and MHD ferrofluid filled in a closed wavy configuration: finite element based study. *Frontiers in Physics*, *10*, 916394.

Mahmoudi, Y., Hooman, K., & Vafai, K. (2019). *Convective Heat Transfer in Porous Media*. CRC Press.

Mahmud, S., & Fraser, R. A. (2004). Magnetohydrodynamic free convection and entropy generation in a square porous cavity. *International Journal of Heat and Mass Transfer*, *47*(14-16), 3245-3256.

Manaa, N., Abidi, A., Hussein, A. K., Alliche, M., Borjini, M. N., & Kolsi, L. (2024). Numerical study of thermo-solutal convection of a Cu/water micropolar nanofluid in a cubic cavity saturated with

porous media. *The European Physical Journal Special Topics*, 1-19. https://doi.org/10.1140/epjs/s11734-024-01111-8

Manole, D. M. (1992). Numerical benchmark results for natural convection in a porous medium cavity. Heat and Mass Transfer in Porous Media, ASME Conference 1992,

Maxwell, J. C. (1873). *A treatise on electricity and magnetism* (Vol. 1). Clarendon press.

Maxwell, J. C. (1904). *A treatise on electricity and magnetism* (Vol. 1). Clarendon press.

Mehryan, S., Izadpanahi, E., Ghalambaz, M., & Chamkha, A. (2019). Mixed convection flow caused by an oscillating cylinder in a square cavity filled with Cu–Al2O3/water hybrid nanofluid. *Journal of Thermal Analysis and Calorimetry*, *137*(3), 965-982.

Mirza, C. R., Abbas, M., Idris, S. A., Khan, Y., Alameer, A., Rajab, A. B., Ismailov, S., Faqihi, A. A., Abbas, A., & Khedher, N. B. (2025). Intelligent computing technique to analyze the two-phase flow of dusty trihybrid nanofluid with cattaneo-christov heat flux model using levenberg-marquardt neural-networks. *Case Studies in Thermal Engineering*, *68*, 105891.

Mirzaei, A., Jalili, B., Jalili, P., & Ganji, D. D. (2024). Free convection in a square wavy porous cavity with partly magnetic field: a numerical investigation. *Scientific Reports*, *14*(1), 14152. https://doi.org/10.1038/s41598-024-64850-7

Mishra, N. K., Adnan, Rahman, K. u., Bani-Fwaz, M. Z., & Khan, Y. (2025). Investigation of micropolar nanofluid using AA7072 alloys under intrinsic polarities: model-based computational analysis. *Journal of Thermal Analysis and Calorimetry*, 1-17.

Morrison, F. (2001). Understanding Rheology Oxford University Press. *New York*.

Muthtamilselvan, M., & Sureshkumar, S. (2017). Impact of aspect ratio on a nanofluid-saturated porous enclosure. *Mechanics & Industry*, *18*(5), 501.

Nabwey, H. A., Jakeer, S., Mansour, M., Salah, T., & Rashad, A. (2025). Entropy generation on MHD hybrid nanofluid flow over a porous square cavity with a cross-shaped obstacle and heater corners. *Journal of Thermal Analysis and Calorimetry*, 1-24. https://doi.org/10.1007/s10973-025-14782-9

Nield, D. A., & Bejan, A. (2006). *Convection in porous media* (Vol. 3). Springer.

Pak, B. C., & Cho, Y. I. (1998). Hydrodynamic and heat transfer study of dispersed fluids with submicron metallic oxide particles. *Experimental Heat Transfer an International Journal*, *11*(2), 151-170.

Peaceman, D. W., & Rachford, J., Henry H. (1955). The numerical solution of parabolic and elliptic differential equations. *Journal of the Society for industrial and Applied Mathematics*, *3*(1), 28-41.

Perry, J. H. (1950). Chemical engineers' handbook. In: ACS Publications.

Poulikakos, D., & Bejan, A. (1985). The departure from Darcy flow in natural convection in a vertical porous layer. *The Physics of fluids*, *28*(12), 3477-3484.

Qayyum, M., Riaz, M. B., & Afzal, S. (2023). Analysis of blood flow of unsteady Carreau-Yasuda nanofluid with viscous dissipation and chemical reaction under variable magnetic field. *Heliyon*, *9*(6). https://doi.org/10.1016/j.heliyon.2023.e16522

Rajenderan, E., & Prasad, V. R. (2024). Numerical study of magneto convective ag (silver) graphene oxide (GO) hybrid nanofluid in a square enclosure with hot and cold slits and internal heat

generation/absorption. *Scientific Reports*, *14*(1), 24868. https://doi.org/10.1038/s41598-024-76233-z

Rashad, A., Rashidi, M., Lorenzini, G., Ahmed, S. E., & Aly, A. M. (2017). Magnetic field and internal heat generation effects on the free convection in a rectangular cavity filled with a porous medium saturated with Cu–water nanofluid. *International Journal of Heat and Mass Transfer*, *104*, 878-889.

Rasool, G., Khan, W. A., Bilal, S. M., & Khan, I. (2020). MHD squeezed Darcy–Forchheimer nanofluid flow between two h–distance apart horizontal plates. *Open Physics*, *18*(1), 1100-1107.

Rebhi, R., Hadidi, N., & Bennacer, R. (2021). Non-Darcian effect on double-diffusive natural convection inside aninclined square Dupuit-Darcy porous cavity under a magnetic field. *Thermal Science*, *25*(1 Part A), 121-132. https://doi.org/10.2298/TSCI190117271R

Rebhi, R., Hadidi, N., Mamou, M., Khechiba, K., & Bennacer, R. (2020). The onset of unsteady double-diffusive convection in a vertical porous cavity under a magnetic field and submitted to uniform fluxes of heat and mass. *Special Topics & Reviews in Porous Media: An International Journal*, *11*(3).

Rebhi, R., Mamou, M., & Alliche, M. (2014). Form drag effect and Hopf bifurcation in Dupuit-Darcy thermal convection in a shallow well-packed porous enclosure. *Physics of Fluids*, *26*(7).

Rebhi, R., Mamou, M., Vasseur, P., & Alliche, M. (2016). Form drag effect on the onset of non-linear convection and Hopf bifurcation in binary fluid saturating a tall porous cavity. *International Journal of Heat and Mass Transfer*, *100*, 178-190.

Reddy, N. K., Swamy, H. K., Sankar, M., & Jang, B. (2023). MHD convective flow of Ag–TiO2 hybrid nanofluid in an inclined porous annulus with internal heat generation. *Case Studies in Thermal Engineering*, *42*, 102719. https://doi.org/10.1016/j.csite.2023.102719

Rees, D. A. S. (1996). The effect of inertia on free convection from a horizontal surface embedded in a porous medium. *International Journal of Heat and Mass Transfer*, *39*(16), 3425-3430.

Rees, D. A. S., & Pop, I. (1995). Non-Darcy natural convection from a vertical wavy surface in a porous medium. *Transport in Porous Media*, *20*, 223-234.

Revnic, C., Groșan, T., Khanafer, K. M., & Pop, I. (2024). Natural convection in a porous square cavity filled with a ternary hybrid nanofluid: A numerical study. *Thermal Science*(00), 272-272. https://doi.org/10.2298/TSCI240927272R

Ribeiro, J.-P., & Gruss, J.-A. (2009). *Nanofluides pour les applications thermiques*. Ed. Techniques Ingénieur.

Riley, D., & Rees, D. A. S. (1985). Non-Darcy natural convection from arbitrarily inclined heated surfaces in saturated porous media. *The Quarterly Journal of Mechanics and Applied Mathematics*, *38*(2), 277-295.

Rosca, A., Rosca, N., Grosan, T., & Pop, I. (2012). Non-Darcy mixed convection from a horizontal plate embedded in a nanofluid saturated porous media. *International Communications in Heat and Mass Transfer*, *39*(8), 1080-1085.

Saeid, N. H., & Pop, I. (2005). Non-Darcy natural convection in a square cavity filled with a porous medium. *Fluid Dynamics Research*, *36*(1), 35.

Salahuddin, T., Tariq, S., Khan, M., & Altanji, M. (2024). The impact of Carreau-Yasuda nanofluid flow on ciliated walls of the channel. *Tribology International*, *191*, 109152. https://doi.org/10.1016/j.triboint.2023.109152

Sarkar, J. (2011). A critical review on convective heat transfer correlations of nanofluids. *Renewable and sustainable energy reviews*, *15*(6), 3271-3277.

Shackelford, J. F., & Alexander, W. (2000). *CRC materials science and engineering handbook*. CRC press.

Sheikholeslami, M., & Ganji, D. D. (2016). *External magnetic field effects on hydrothermal treatment of nanofluid: numerical and analytical studies*. William Andrew.

Sheremet, M. A., Revnic, C., & Pop, I. (2017). Free convection in a porous wavy cavity filled with a nanofluid using Buongiorno's mathematical model with thermal dispersion effect. *Applied Mathematics and Computation*, *299*, 1-15. https://doi.org/10.1016/j.amc.2016.11.032

Sisko, A. (1958). The flow of lubricating greases. *Industrial & Engineering Chemistry*, *50*(12), 1789-1792.

Sundar, L. S., Ramana, E. V., Singh, M. K., & Sousa, A. C. (2014). Thermal conductivity and viscosity of stabilized ethylene glycol and water mixture Al2O3 nanofluids for heat transfer applications: An experimental study. *International Communications in Heat and Mass Transfer*, *56*, 86-95.

Suresh, S., Venkitaraj, K., Selvakumar, P., & Chandrasekar, M. (2011). Synthesis of Al2O3–Cu/water hybrid nanofluids using two step method and its thermo physical properties. *Colloids and Surfaces A: Physicochemical and Engineering Aspects*, *388*(1-3), 41-48.

Teng, T.-P., & Hung, Y.-H. (2014). Estimation and experimental study of the density and specific heat for alumina nanofluid. *Journal of Experimental Nanoscience*, *9*(7), 707-718.

Vafai, K. (2015). *Handbook of porous media*. Crc Press.

Vahedi, S. M., Pordanjani, A. H., Wongwises, S., & Afrand, M. (2019). On the role of enclosure side walls thickness and heater geometry in heat transfer enhancement of water–Al 2 O 3 nanofluid in presence of a magnetic field: sensitivity analysis and optimization. *Journal of Thermal Analysis and Calorimetry*, *138*, 679-696.

Vajjha, R. S., Das, D. K., & Kulkarni, D. P. (2010). Development of new correlations for convective heat transfer and friction factor in turbulent regime for nanofluids. *International Journal of Heat and Mass Transfer*, *53*(21-22), 4607-4618.

Venkatadri, K., Fazuruddin, S., Anwar Bég, O., & Ramesh, O. (2023). Natural convection of nanofluid flow in a porous medium in a right-angle trapezoidal enclosure: a Tiwari and Das' nanofluid model. *Journal of Taibah University for Science*, *17*(1), 2263224. https://doi.org/10.1080/16583655.2023.2263224

Vigneshwari, S., Reddappa, B., & Kumar, B. R. (2025). Magnetohydrodynamic natural convection of complex fluids in a square porous cavity: A numerical simulation. *Journal of Thermal Engineering*, *11*(3), 780-799.

Walker, K. L., & Homsy, G. M. (1978). Convection in a porous cavity. *Journal of Fluid Mechanics*, *87*(3), 449-474. https://doi.org/10.1017/S0022112078001718

White, F. M., & Majdalani, J. (2006). *Viscous fluid flow* (Vol. 3). McGraw-Hill New York.

Xuan, Y., & Roetzel, W. (2000). Conceptions for heat transfer correlation of nanofluids. *International Journal of Heat and Mass Transfer*, *43*(19), 3701-3707. https://doi.org/10.1016/S0017-9310(99)00369-5

Xue, Q. (2005). Model for thermal conductivity of carbon nanotube-based composites. *Physica B: Condensed Matter*, *368*(1-4), 302-307. https://doi.org/10.1016/j.physb.2005.07.024

Yasuda, K. (1979). *Investigation of the analogies between viscometric and linear viscoelastic properties of polystyrene fluids* Massachusetts Institute of Technology].

Yılmaz Aydın, D., & Gürü, M. (2021). Nanofluids: preparation, stability, properties, and thermal performance in terms of thermo-hydraulic, thermodynamics and thermo-economic analysis. *Journal of Thermal Analysis and Calorimetry*, 1-34.

Young, D. M. (1950). *Iterative methods for solving partial differential equations of elliptic type* [Doctoral Thesis, Harvard University]. Cambridge, MA.

Yu, W., Choi, & SUS. (2003). The role of interfacial layers in the enhanced thermal conductivity of nanofluids: a renovated Maxwell model. *Journal of Nanoparticle Research*, *5*, 167-171.

Zafar, M., Sakidin, H., Sheremet, M., Dzulkarnain, I., Nazar, R., Al-Yaari, A., & Salleh, M. Z. (2023). MHD Free Convection Heat Transfer in Nano-Fluid Flow in Square Porous Cavity of TiO2 Nanoparticles with Base Fluid Engine Oil. *Journal of advanced research in fluid mechanics and thermal sciences*, *110*(1), 145-156.

Zhang, L., Hu, Y., & Li, M. (2021). Numerical study of natural convection heat transfer in a porous annulus filled with a Cu-nanofluid. *Nanomaterials*, *11*(04), 990.

Zhou, L.-P., Wang, B.-X., Peng, X.-F., Du, X.-Z., & Yang, Y.-P. (2010). On the specific heat capacity of CuO nanofluid. *Advances in mechanical engineering*, *2*, 172085.